DEMOCRATIC AND POPULAR REPUBLIC OF ALGERIA
MINISTRY OF HIGHER EDUCATION AND SCIENTIFIC RESEARCH

Mohamed Boudiaf University of - M'sila
Faculty of Sciences
DEPARTEMENT OF PHYSICS

Serial number: …….
Registration number: DPH/01/16

THESIS

Presented to obtain the degree of

Doctor of Science

Specialty: Materials physics
Option: Material sciences

THEME:

Elaboration, characterization and modeling of oxide-based nanostructured thin films.

Presented by:
Mr. Ammar BOUKHARI

Discussed publicly on: 19/12/2021
with the board of examiners:

Mss. AZZEDDINE Hiba	Professor	Univ. of M'sila	Chairman
Mr. DEGHFEL Bahri	Professor	Univ. of M'sila	Supervisor
Mr. AHMAD AZMIN	Professor	Univ. Sains Malaysia	Co- Supervisor
Mr. IBRIR Miloud	Professor	Univ. of M'sila	Examiner
Mr. GUEDDIM Ahmed	Professor	Univ. of Djelfa	Examiner
Mr. BOUKAOUD Abdelali	MCA	Univ. of Medea	Examiner
Mr. BAAZIZ Hakim	Professor	Univ. of M'sila	Invited

Academic year : 2020/2021

بِسْمِ اللَّهِ الرَّحْمَنِ الرَّحِيمِ

ABSTRACT

The structural, morphological, electronic, and optical properties of pure, 4 %, and 7 % Mn-doped ZnO thin films deposited on glass substrate by the sol–gel spin coating process are investigated in this study. All films exhibited a hexagonal wurtzite structure with a strong c-axis preference. The surface morphology was uniform, with a cracks and wrinkles. With increasing thickness, the transmittance decreased. The bandgap energy varied inversely with the coatings number. photoluminescence spectra revealed ultraviolet with strong and weak blue emission peaks, as well as weak green emission peaks. The structural, electronic, and optical properties of pure and 6.25 % Mn-doped ZnO materials were then investigated using density functional theory and the Hubbard (DFT+U) approach. The DFT+U approach demonstrated a decrease in bandgap energy from pure to 6.25 % Mn-doped ZnO material. It was also discovered that the Mn3d states were distributed far from the Fermi level, with both ionic and covalent nature bonds coexisting. Mn doping caused a small shift in optical properties toward the lower energy. The theoretical findings were consistent with those obtained through experiment.

Keyword: Film thickness; Sol-gel spin coating method; Mn-doped ZnO; Structural properties; Optical properties; DFT+U

This thesis is dedicated

To

Ahmed Yasin's Soul

ACKNOWLEDGEMENTS

First of all, all thanks and praises for Allah who guided me and helped me to complete this thesis. I would like to warmly thank my thesis supervisor Prof. Bahri DEGHFEL, for his help, his confidence, his wise advice, and his support during all these last five years. I would particularly like to express my sincere gratitude and my deepest gratitude to him.

I would like to express my deepest sense of gratitude to my co- supervisors Prof. Ahmad Azmin Mohamad, professor of the School of Materials and Mineral Resources at Sains Malaysia University (USM), and member of the Ionic Materials and Devices Research Laboratory (IMADE), Institute of Science, Universiti Teknologi, Malaysia, for his patient, guidance, encouragement, excellent advices, and the experience I got because of him and his hospitality throughout my internship in USM.

I owe sincere thanks to the Algerian Ministry of higher Education and scientific research for giving me the opportunity to study outside the country, in the frame of national exceptional program (PNE). Many thanks also go to University Sains Malaysia for giving me the chance to study continue my thesis research in it under the supervision of Professor Ahmad Azmin Mohamad.

My sincere thanks also go to Professor AZZEDINE Hiba from the University of M'sila who does me the honor of chairing this jury. I would then like to thank all the members of the jury for having accepted to evaluate this work, Professors BAAZIZ Hakim and IBRIR Miloud from the University of M`sila, Doctor BOUKAOUD Abdelali, Lecturer at the University of Medea, and Professor GEDDIM Ahmed from the University of Djelfa.

A deep hearted gratitude goes to my loving mother, my father, my brothers, and my wife for their full support, love, care and inspiration. I would like to express my gratitude to all those who made it possible for me to complete this study.

TABLE OF CONTENTS

LIST OF FIGURES

LIST OF TABLES

I.General Introduction

I.1 Introduction

Recently, much attention has been paid to the semiconducting metal oxides materials such as TiO_2, SnO_2, CuO and ZnO, which have been researched extensively and have raised tremendous interest in the academic and industry fields. At the nanoscale, these materials change their characteristics considerably compared to the equivalent micro and macro size, and they exhibit attractive physical characteristics and advantages, that are: stability, non-toxic, low cost, etc. Metal oxides are attractive candidates, notably in photovoltaics, optoelectronics and for application in numerous fields of technology [1-3].

Transparent Conductive Oxides (TCOs) are interesting materials in several technological sectors. Their electric conductivity and transparency in the visible range, make them ideal candidates for various applications [4].

Zinc oxide (ZnO), a II–VI semiconductor material, belonging to the family of transparent conductive oxides, has received a lot of attention and research due to its wide bandgap (3.37 eV) and high exciton binding energy (60 meV) [5]. Thus, its physical and chemical properties are enticing many researchers to use it in various applications [6, 7].

The variation of material composition, concentration, thickness, annealing temperature, and other parameters can modify the structural, electronic, and optical properties of ZnO thin films, due to the changes in surface morphology, particle size, crystalline structure orientation, and defect concentration [8]. Furthermore, to improve its properties, ZnO is doped with transition metal elements such as Fe, Al, Co, and Mn [9].

Doping ZnO with Mn^{+2} exhibits promising optical and luminescence properties, such as a high optical gain (300 cm^{-1}) and a very short luminescence lifetime, which are required for a variety of optoelectronic and magneto-optical devices [10, 11]. Generally, due to the similarity in the ionic radius of Mn^{2+} (0.80Å) and Zn^{2+} (0.74Å) ions, which facilitating the incorporation of the dopant in the host lattice, the wurtzite structure stay kept [12]; however, it may cause changes in the luminescence, electronic, and optical properties of ZnO. Unlike strain and roughness, numerous studies found that the grain size, average transmittance, and bandgap values of Mn-doped ZnO thin films are less than the pure ZnO values [11, 13].

The thickness effect of pure ZnO thin films have been widely investigated using different physical and chemical synthesis methods such as atomic layer deposition [6], pulsed laser deposition [14], filtered cathodic vacuum arc [15], spray pyrolysis [16, 17], magnetron sputtering [7, 18], Thermal evaporation [19] and sol–gel [20-24].

To the best of our knowledge, investigations on the thickness effect of Mn-doped ZnO thin films, which mostly used RF magnetron sputtering method for preparation, are limited [25-27]. It is worth noting that thickness parameter has a significant influence on the properties of pure and Mn-doped ZnO thin films. According to the literature, pure ZnO films studied using the sol–gel method, generally prefer the (002) c-axis orientation and crystallize in wurtzite structure. By increasing the thickness (number of coats), the crystallinity improves with the increase of grain size and roughness, while the strain, average transmittance, and bandgap decrease [20, 23, 28-34]. This behavior is similar to that of Mn-doped ZnO prepared by RF magnetron sputtering method [25-27].

Theoretically, the first-principles method based on density functional theory (DFT) in the local density approximation (LDA) has been successfully applied to study molecules, surfaces, interfaces, and solid states. The ground state properties of materials can be accurately predicted using this approach [35, 36].

The standard DFT method failed to describe the ground-state properties of materials containing strong localized d- and f-electron metals and underestimated their fundamental bandgap and corresponding optical properties [37]. The DFT+U approach was then successfully applied to address this problem [38].

To predict the physical properties of pure and Mn-doped ZnO materials, few researches were performed using the first-principle pseudopotential method based on density functional theory (DFT) and different forms of exchange-correlation function [39-41].

I.2 Objectives of the thesis

In this thesis, there are three main targets;(i) investigating experimentally the influence of thickness on the structural, morphological, and optical properties of pure, 4% and 7% Mn-doped ZnO thin films, (ii) studying theoretically, by DFT +U approach, the properties of pure and Mn-doped ZnO structure ($Zn_{1-x}Mn_xO$, x = 6.25%), and (iii) comparing the experimental findings with the theoretical results of pure and doped ZnO materials.

I.3 Organization of the thesis

Following this introductory chapter, a background of ZnO nanostructures will be reviewed in chapter II, along with ZnO properties, discussions on previous studies on the thickness effects on the physical properties of pure and Mn-doped ZnO thin films, semiconductors and thin films will be also discussed in general with their types and growth modes. Chapter III

describes the experimental steps and the calculation details including; samples preparation, growth process and the different measurements that had been used for characterizations. In addition, chapter IV presents the experimental and DFT results with discussions of the thickness effects on the structural, morphological, and optical properties of pure, 4% and 7% Mn doped-ZnO thin films followed by comparison between different results. Finally, a general conclusion summarizes the main results of this work.

II.Literature review of ZnO thin films

II.1 Introduction

Oxide-based thin films, particularly ZnO, which has remarkable properties, have received a lot of attention in recent years due to their potential applications in optoelectronics, piezoelectric, photovoltaic cells, and spintronics. In this chapter, we will present a brief overview of the structural, optical and morphological properties of ZnO thin films and their most important applications in various technological fields. Also, an overview on the thickness effect on these properties of pure and Mn- doped ZnO thin films. Thin films and semiconductors will also be discussed in general, including definitions, thin film growth modes, and semiconductor types.

II.2 Thin films

II.2.1 Definition

In general, a thin film of a given material is the material deposited on a support known as a substrate. One of its dimensions (thickness) could strongly reduce to the scale of nanometers. This quasi-two-dimensionality gives the first characteristic of the thin film. This characteristic results in a disturbance of the majority of the physical properties **(Figure II.1)**. The fundamental difference between the bulk and thin films forms is that the role of the boundaries in the properties is usually overlooked in the bulk form of materials, whereas in the thin film form, the effects related to the boundaries are preponderant and very important. It is obvious that the thinner the thickness, the greater the two-dimensional effect. Conversely, when the thickness of a thin layer exceeds a certain threshold, the thickness effect diminishes and the material regains its properties [42].

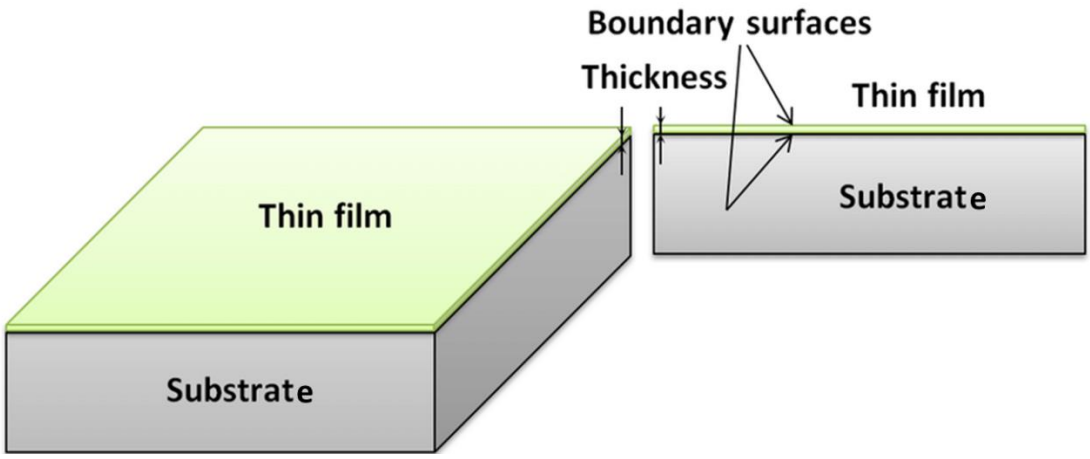

Figure II. 1. Schematic of deposited thin film on a substrate [43].

II.2.2 Thin film growth mechanisms

All thin film manufacturing processes are divided into three stages:

a) The **production** of the appropriate ionic, molecular, atomic species

b) **Transport** of these species to the substrate

c) **Condensation** on the same substrate is done either directly or by means of a chemical or electrochemical reaction in order to form the solid deposit. This stage often goes through three phases **(Figure II.2)** [44]:

(i) **Nucleation**, is the formation of small nuclei that are statistically distributed over the surface of the substrate.

(ii) **Growth** of the nuclei and formation of larger islands, which often have the shape of small crystals (crystallites).

(iii) **Coalescence** of the islands (crystallites) and formation of a more or less connected network containing empty channels.

Figure II. 2. Thin film formation Mechanisms: Coalescence and growth [45].

II.2.3 Thin film growth modes

Thin film growth on a substrate is classified into three modes **(Figure II.3)**.

II.2.3.1 Volmer-Weber mode

The Volmer-Weber growth mode (VW) occurs when atoms or molecules arrive on the surface of the substrate and have a greater tendency to bond with each other than with the substrate. A typical case of this growth is that of metallic films on insulating substrates.

II.2.3.2 Frank-Van der Merve mode

When the atoms-substrate interaction is very strong, Frank–Van der Merwe growth (FM), also known as 'layer-by-layer' growth mode, occurs. The first atoms that arrive into the substrate surface condense and form a monolayer that covers the entire surface, a two-dimensional growth of nuclei to form a layer, then grow layer by layer.

II.2.3.3 Stransky-Krastanov mode

Stranski-Krastanov growth mode (SK) is an intermediate case between FM and VW. The growth is initially 2D to form the first layers; however, as the atoms-substrate interaction energy gradually decreases, the growth tends to become three-dimensional with forming 3D islands.

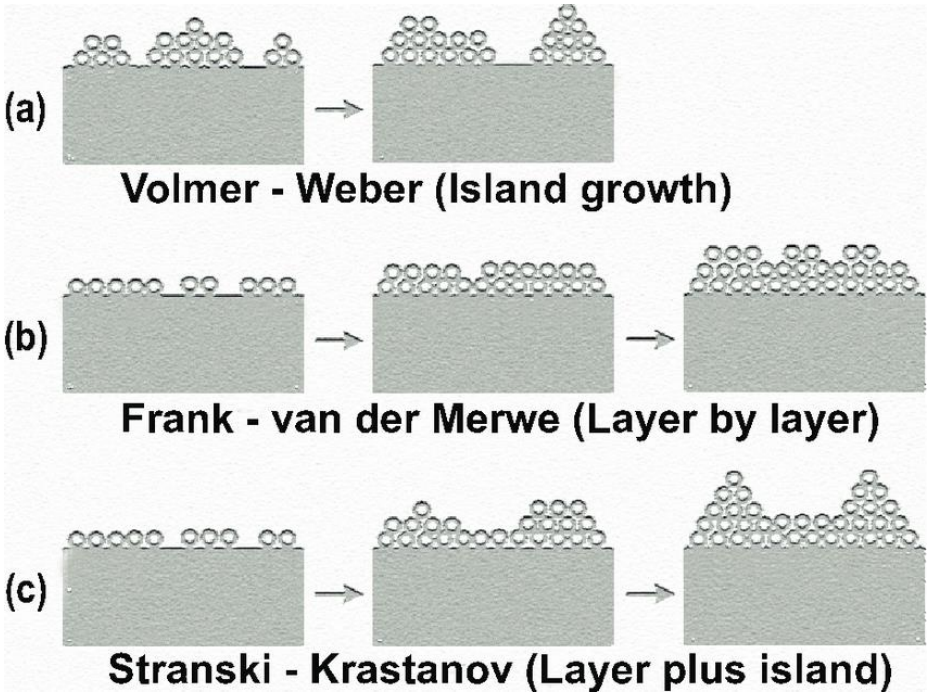

Figure II. 3. Cross-section views of the three primary modes of thin-film growth. (a) Volmer-Weber (island growth), (b) Frank-Van der Merwe (layer by layer), and (c) Stranski-Krastanov (layer plus island) [46].

II.3 Semiconductors

II.3.1 Definition

A semiconductor is a crystalline solid whose electrical conduction property is determined by two particular energy bands: on the one hand, the valence band, which corresponds to the electrons involved in covalent bonds; on the other hand, the conduction band, comprising electrons in an excited state, which can travel within the crystal. These two bands are separated by a gap or a forbidden band that the electrons can only cross thanks to an external excitation such as the absorption of a photon [47].

II.3.2 Types of semiconductors

Semiconductors are of two types, intrinsic and extrinsic.

II.3.2.1 Intrinsic semiconductors

An intrinsic semiconductor material is chemically very pure and does not contain any impurity. It possesses poor conductivity and carries same number of negative and positive charge carriers. The number of electrons in the conduction band is equal to the number of holes in the valence band. Under the influence of thermal agitation or by photo excitation, electrons can transit from the valence band to the conduction band. In this case there will be creation of free electrons in the conduction band and holes in the valence band which make it possible to increase the electrical conduction of the material. In this type of (intrinsic) semiconductor, the concentrations of electrons (n) and holes (p) are equal and the Fermi level is in the middle of the forbidden band.

II.3.2.2 Extrinsic semiconductors

Extrinsic semiconductors are improved intrinsic semiconductors. Small number of impurities are added by doping process. Doping is another way to increase the electrical conductivity of the semiconductor. There are two types of extrinsic semiconductors: the first (type n) is formed by the introduction of pentavalent impurities where the doping atoms (called donor atoms) provide an electron to the conduction band. The second (type p) formed by the introduction of trivalent impurities where the doping atoms (called acceptor atoms) have a lack of electrons compared to the matrix and capture an electron from the valence band, which allows them to " increase the number of holes in the valence band. Doping causes new acceptor and electron donor levels to appear in the band structure of the doped material. These levels appear in the gap, between the conduction band and the valence band **(Figure II.2).**

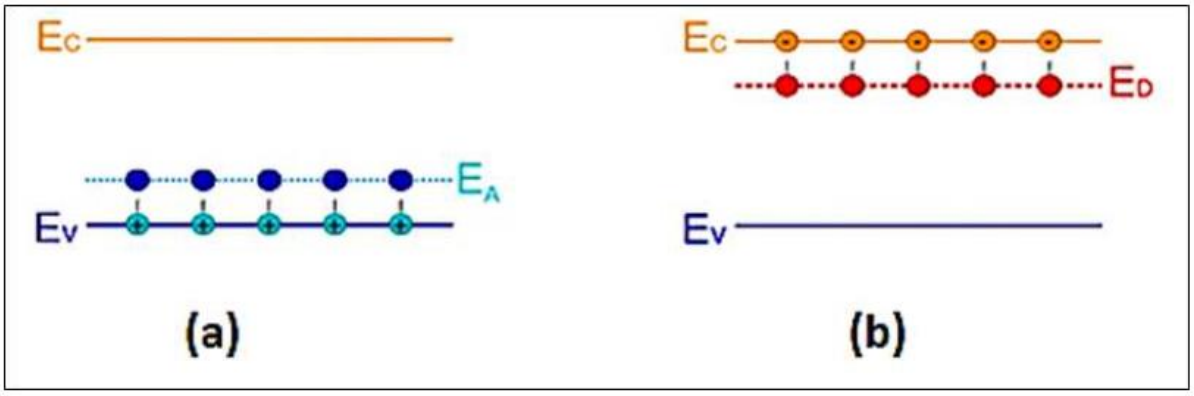

Figure II. 4. The energy level of the doping element: (a) p-type doping, (b) n-type doping.

II.3.3 Semiconductors based on metal oxides

In general, a metal oxide is composed of metal atoms and oxygen. Metal oxides can be classified either according to the nature of the conduction by electrons or holes, or according to whether simple or complex metal oxides. Metal oxides play a very important role in many fields of chemistry, physics and materials science. Metal oxides have a metallic, semiconductor or insulating character due to the difference in electronic structure. Normally, the oxides formed by metals residing on the left or right of the periodic table are generally insulating in nature (eg, MgO, CaO, Al_2O_3, SiO_2), while those formed by metals residing in the middle of the periodic table are semiconductors or metallic in nature (e.g, ZnO, NiO, TiO_2, CuO, Fe_2O_3). Semiconductors based on metal oxides have received considerable attention in recent years due to their optical, electrical and their various applications. Some of them are good candidates for films conductive transparencies. Oxide-based semiconductors are preferred in photo-electrochemistry because of their exceptional stability against photo-corrosion during optical excitation in the forbidden band, moreover, because of the wide band gap (> 3 eV) of this type of materials. Undoped and doped oxide thin films have a wide range of applications as important semiconductor materials, such as solar cells and electrical, piezoelectric or luminescent devices, as well as gas and chemical sensors.

It is well known that chemical doping greatly influences the electronic and optical properties of oxide thin films.

II.3.4 Transparent conductive oxides (TCO)

Transparent conductive oxides are optically transparent (band gaps > 3.1 eV) and electrically conductive (carrier concentration of at least 10^{19} cm^{-3}). These two special properties lead this kind of materials to be useful in many of electronic devices including touchscreens, liquid-crystal displays and photovoltaics [48].

TCOs can become conductive (n-type) if their lattice contains too many electrons. This excess of electrons can be caused by structural defects that cause an imbalance in the stoichiometry of the oxide, or by doping with a metal [49]. N-type TCOs (SnO_2, ZnO, In_2O_3 …. etc) are already utilized in a range of technological applications. However, p-type TCOs (NiO, $CuAlO_2$, $CuInO_2$, $CuGaO_2$ $CuInO_2$, $SrCu_2O_2$, and LaCuOCh) have proved to be harder to manufacture [50-52].

These TCOs with a large gap are degenerated semiconductors, which means that their Fermi level is very close to, or even within, the conduction band (CB) for heavily doped TCOs. This means that the CB is already well filled with electrons at room temperature, thus making the TCOs conductive. Furthermore, the large gap of TCOs (~3 - 4 eV) prevents them from absorbing photons with energies lower than the gap, and making them transparent to visible light.

II.4 Zinc oxide (ZnO) thin films

Recently, ZnO and its derivative has attracted intensive research effort for its versatile applications and it exhibits many unique interesting properties [11, 36, 53]. Thanks to its semiconducting, optical, piezoelectric and catalytic properties, zinc oxide has become an interesting material in research field, due to its characteristics such as a wide direct band gap of 3.37 eV which allows it to be transparent to visible light, a high free energy of exciton binding (60

meV), a high cohesion energy of 1.89 eV, a high optical gain (300 cm^{-1}) and high mechanical and thermal stability [54]. In addition, ZnO is non-toxic, cheaper and abundant on the earth's crust. In this section, a discussion of the most important zinc oxide properties will be presented in details.

II.4.1 General properties of ZnO

II.4.1.1 Structural properties

ZnO is one of II-VI compound semiconductors. It has crystal structure of hexagonal wurtzite (B4) **(Figure II.4a)**, zinc blend (B3) **(Figure II.4b)** or rock salt (B1) **(Figure II.4c)** (cubic symmetry) [55].

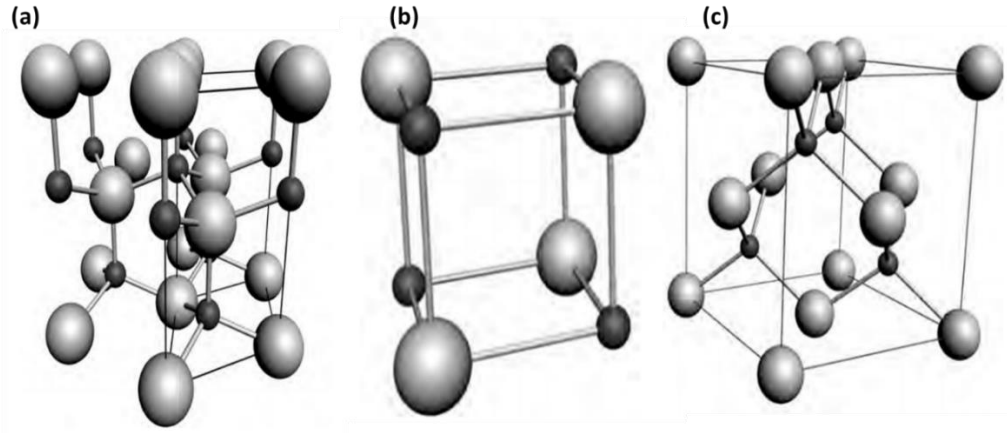

Figure II. 5. The phases of ZnO structure; (a) hexagonal wurtzite, (b) rock salt and (c) zinc blende. O atoms are shown as white spheres, Zn atoms as black spheres. Only one unit cell is illustrated for clarity [56].

Under the ambient conditions, ZnO crystals most commonly stabilize in the wurtzite structure with a hexagonal unit cell (space group *P63mc*), while the zinc blende structure can only be stable on substrates with a cubic structure. In these two structures, the unit cell forms a tetrahedron structure which consists of 5 atoms; one atom belongs to zinc (cation) and is surrounded by 4 oxygen atoms (anions) and vice versa. These Zn-O bonds are both ionic and covalent. However, the crystals exhibit the rock salt phase only at high pressures (10-15 GPa).

The ZnO wurtzite phase has a polar hexagonal axis known as the c-axis (0002) that is parallel to the z-axis and the other is the nonpolar plane and includes $(11\bar{2}0)$ and the $(10\bar{1}0)$. The lattice parameters of ZnO wurtzite structure are found to be around of $a = b = 3.2496$ Å, $c = 5.2042$ Å and $\beta = 120°$, with a ratio of $c/a = 1.601$ which is close to that of an ideal compact hexagonal structure (c/a =1.633) **(Figure II.5)**.

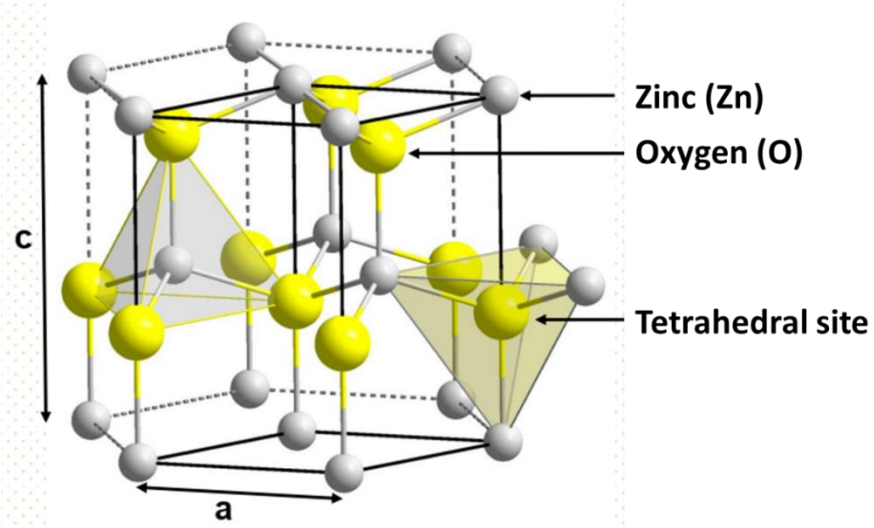

Figure II. 6. Elementary crystal lattice of the wurtzite structure of ZnO [57].

II.4.1.2 Electronic and optical properties

Zinc oxide is a direct wide bandgap type II-VI semiconductor of 3.37 eV at room temperature. This energy is what causes an electron to move from the valence band (VB) to the conduction band (CB). In general, the band structure can provide the band gap value of each material. The band structure of ZnO is related to its crystallographic structure, and to the electronic configurations of oxygen ($1s^2 2s^2 2p^4$) and zinc ($1s^2 2s^2 2p^6 3s^2 3p^6 3d^{10} 4s^2$), where the 2p states of oxygen form the valence band and the 4s states of zinc constitute the conduction band. **Figure II.7** represents the shape of the ZnO band structure which is shown in the reciprocal space of the Brillouin zone [58].

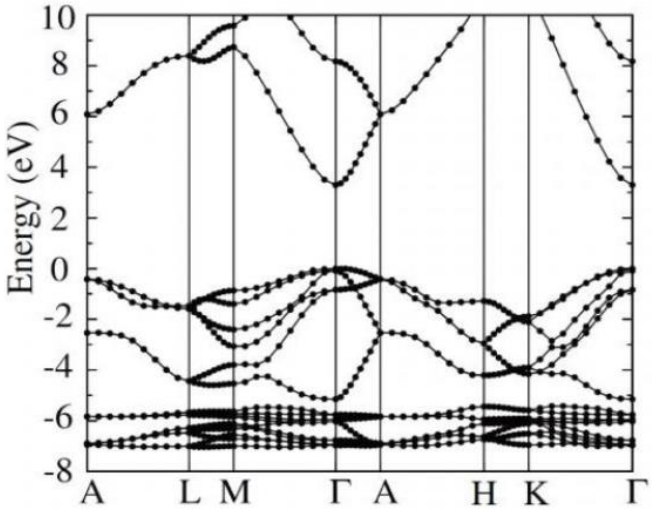

Figure II. 7. Theoretical band diagram of ZnO in wurtzite structure [58]

The Brillouin zone associated with the wurtzite structure of ZnO with several points of high symmetry is illustrated in **Figure II.8** [58]. The direction Γ -A coincides with the z axis in the real space.

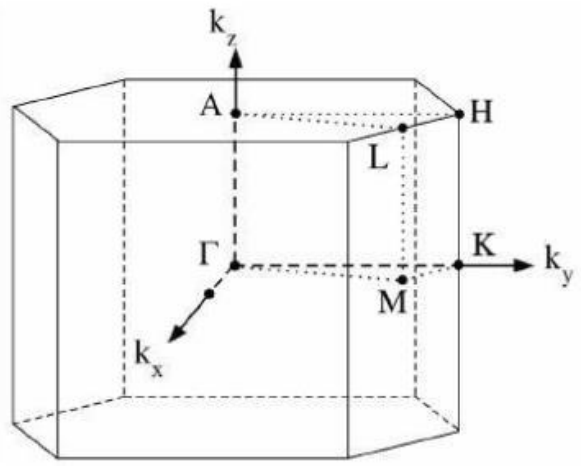

Figure II. 8. First Brillouin zone of the wurtzite structure [58].

At the point Γ (k = 0), the ZnO material is a direct gap semiconductor (characteristic of the existence of a minimum energy in the BC and a maximum energy in the BV). The value of this band gap is approximately 3.37 eV, corresponding to an absorption threshold in the near ultraviolet

of approximately 380 nm [59]. This value of band gap is extremely important for optics particularly interesting for opto-electronic applications in the near ultraviolet UV of around 380 nm. Because of its large gap, this material is capable of allowing more than 90% of visible light to pass through under conditions of sufficient crystalline quality.

Zinc oxide is a transparent material whose refractive index in its massive form is equal to 2, and in the form of a thin film, its refractive index and its absorption coefficient, vary according to the elaboration conditions. The refractive index varies between 1.90 and 2.20 [60].

II.4.1.3 Luminescence of zinc oxide

Luminescence is the process of returning a material to its energy equilibrium after it has been excited by a light wave (photoluminescence) or electron bombardment (cathodoluminescence) of energy greater than or equal to the material gap, where the absorption of this energy creates an "electron - hole" pair called an exciton. The exciton can be free, associated with an ionized or neutral impurity, donor or acceptor [61].

Zinc oxide emits two types of luminescence: the first is excitonic, due to the recombination of an electron-hole pair created after the absorption of energy greater than the gap. The energy released in the form of UV photon corresponds to the energy of the gap minus the binding energy of the exciton estimated at 60 meV in ZnO. The measured wavelength is therefore approximately 380 nm at room temperature. The binding energy of the exciton is much greater than kT at room temperature, thus promising strong UV luminescence.

The second luminescence is for its part correlated with the presence of structural defects, impurities, dopants, which will create energy levels in the gap more or less close to the valence and conduction bands.

In ZnO, there are two types of defects (**Figure II.7)**. The first called "deep" defects, whose energy levels are located a few hundred meV or a few eV from the valence band (VB) and conduction bands (CB), these defects are intrinsic in the ZnO film, such as oxygen vacancies or Zn interstitial, and give luminescence in the visible [62]. The second-called "shallow" defects located a few tens of meV from VB and CB. These last defects are "doping" defects, will create the bound excitons [63]. They will eventually induce discrete energy levels in the ZnO wurtzite gap, influencing significantly the optoelectronic properties of the material. Because the excitons trapping energy is very low at shallow defects, the characteristic emission of these defects is energetically very close to that of free excitons and is only visible at low temperatures.

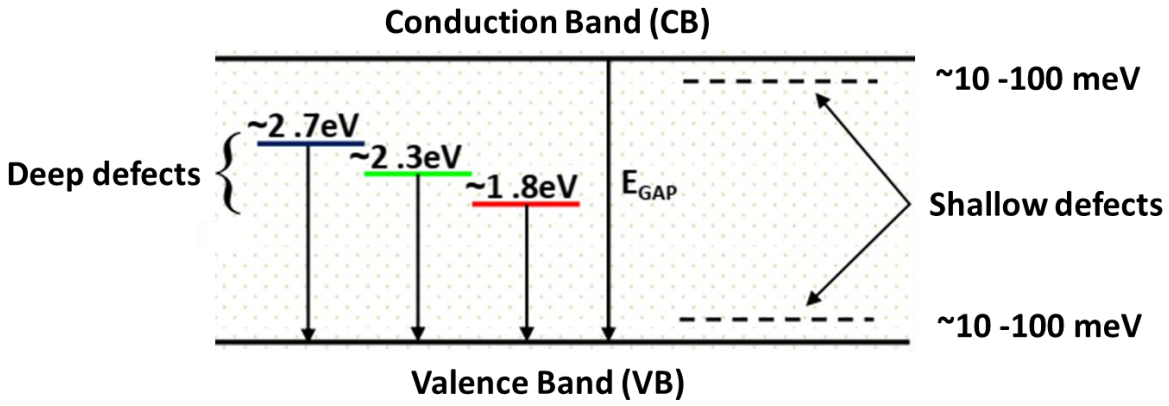

Figure II. 9. Implantation in the forbidden band of deep and shallow defects [58].

II.4.2 Doping of ZnO

Doping is the introducing of impurities into an extremely pure semiconductor. For several applications in the optoelectronic and magnetic fields, improvement in the properties of ZnO thin films, commonly occurs through doping. These properties could be affected by the type of dopant, its valence state and its emplacement in the lattice structure (substitution or interstitial) [64]. The

best doping candidate should have high solubility, be relatively stable within the crystal lattice, and have sufficiently low ionization energy.

There are several studies and results in the literature showing that it is possible to dope the ZnO matrix with generally metallic elements according to the desired physical properties; for example for optoelectronic properties, we can cite Aluminum (Al), magnesium (Mg) and indium (In) [65-67], and for magnetic properties Cobalt (Co), Copper (Cu) and manganese (Mn) [11, 36, 68].

Doping in ZnO can be classified into two types, cationic and anionic doping. The cationic doping is the process of doping a cation such as, Al, Sn, Ga, In, Cd, Cu, Fe, Co, Mn, and Ni. However, anionic doping is the doping of anions; e.g. As, N, and S.

For example, incorporation of Mn resulted in a decreased crystallite size, bandgap and transparency. Red-shift of absorption edge is observed clearly with Manganese doping [8].

II.4.3 Applications of ZnO

Due to the properties of ZnO nanostructure, mentioned previously, zinc oxide (ZnO) is widely used in our society, and it is an important component in many industrial manufacturing processes such as paints, cosmetics, pharmaceuticals, plastics, batteries, electrical equipment, rubber, textiles, and floor coverings. Also, ZnO has been used for acoustic wave devices, gas sensors, solar cells, piezoelectric transducers, light emitting diodes (LEDs), laser diodes (LDs) and transparent electrodes [3, 69-72].

In addition, zinc oxide has been used in a variety of technical applications, including porcelain enamels, heat resisting glass, an activator in vulcanization, an additive for rubber and plastics, pigment in paints with UV-protective and fungi static properties, spacecraft protective coatings, a constituent of cigarette filters, healing ointments and in optical waveguide. Recently,

based on piezoelectricity effect of ZnO nanowires, nanogenerator driven by an ultrasonic wave was achieved. Finally, it is worthy to note that ZnO has been also used in medical applications such as sunburn prevention, nappy rash, skin irritations, cold sores, cuts and burns treatments [56, 73-76].

II.5 Review on the thickness effect of pure and Mn- doped ZnO

The thickness is an important parameter in the elaboration of thin films. Its effect on the physical properties of pure ZnO thin films were investigated by various authors using different elaboration method such as: elaboration atomic layer deposition [6], pulsed laser deposition [14], filtered cathodic vacuum arc method [15], spray pyrolysis [16, 17], magnetron sputtering [7, 18], and sol–gel [20-24]. However, limited investigations were performed on the properties of Mn-doped ZnO thin films [25-27].

The thicknesses of films, elaborated by different methods at various experimental conditions, were measured by different techniques such as cross-sectional SEM 2D-image, Profilometer, envelope method based on transmittance measurement.

II.5.1 Thickness effect of pure ZnO

II.5.1.1 Structural properties

X-ray diffraction (XRD) is a powerful and non-destructive technique for structural characterization of materials. It provides information on the structure and phase of crystals and can also confirm the incorporation of defects in each host lattice. Different parameters, such as the lattice parameters, crystallite size and number of phases, stress and strain, could be deduced from the diffraction peaks of XRD analysis [77].

Whatever the elaboration method, ZnO thin films are generally polycrystalline (P63mc space group; JCPDS card 36-1451), with XRD peaks corresponding to the (100), (002), (101), (102), (110), (103), and (112) planes [28, 74, 78]. The XRD spectra commonly show three main peaks at the angles of ~31.9°, ~34.5°, and ~36.4° which are assigned to (100), (002) and (101) planes respectively [79]. Moreover, in some cases, only (002) peak can be observed [78, 80]. Among the planes from XRD spectra, pure ZnO prefers (002) plane as a dominant orientation [81]. However, in some other conditions of sol-gel elaboration method, ZnO prefers (100) or (101) planes as a preferential orientation [82, 83]. Some researchers confirmed the preferential orientation by calculating the texture coefficient **(Table II.1)** [84, 85].

From the literatures, the variation of film thicknesses can influence the different XRD parameters, whatever the deposition method [17, 23, 78, 86]. In general, it is observed that the lattice constants a = b and c, which are usually calculated from XRD patterns, decrease with increasing of the thickness [16, 74, 81]. Some exceptions were noted where the lattice parameter increased **(Table II.1)** [29, 32].

It is also found that the increasing of thickness influences the crystallite size (D). The crystallite size presents an increase with increasing the thickness, [80, 87, 88] while an increase followed by a decrease is marked at higher thickness **(Table II.1)** [89] .

II.5.1.2 Morphological properties

Many researchers were used Atomic Force Microscopy (AFM) and/or Scanning Electron Microscopy (SEM), to investigate the smallest of internal ZnO thin films. That because of their ability to reveal the grain size and surface roughness. These micrographs provide additional confirmation to XRD pattern results.

AFM analysis of ZnO thin films of various thicknesses has been reported in the literature [17, 20, 30, 86]. Two and three-dimensional AFM images, as well as morphological parameters such as roughness and grain size, are then typically extracted **(Table II.1)**.

All works noticed an increase in the grain size and surface roughness with increasing the thickness **(Table II.1)**, while other work marked a decrease of roughness despite the increase of grain size at lower thin film thickness (15 nm - 200 nm) deposited by sol- gel [90]. In the same work, hillocks with island-like growth were also observed. However, in other works, islands type growth of the films [14], a regular surface morphology with evidence of granular structures characterized by columnar growth perpendicular to the substrate were clearly observed [86].

Many reports showed SEM or FE-SEM images for ZnO films elaborated by different process at various experimental conditions for thickness effect investigation [17, 20, 74, 86, 91]. As the film thickness increases, it was observed that the grains become larger, and also observed that the surface become more porous for thin films prepared by sol- gel and deposited on alumina substrate [20]. For ZnO samples deposited on SiO2/Si substrates by RF magnetron sputtering, the SEM micrographs with high-magnification exhibits a smooth surface consisting of very small spherical-like grain size particles. As the thickness increased, denser surface is observed [86].In another work, SEM images of the films with higher thicknesses (280 and 366 nm) indicate that a dense packing of grains without any cracks are observed for samples prepared by sol- gel method on glass substrate [91]. Zhong et al. have reported that with the increase in film thickness, the grain size increases and the grain shape changed from regular hexagonal sheet-like to wedge-shaped, even pyramidal [92].

II.5.1.3 Electronic and optical properties

Ultraviolet-Visible (UV-Vis) spectroscopy is widely used for investigating the electronic and optical properties of thin films. To study the thickness effect on these properties of ZnO thin films, several studies were done using UV-Vis spectroscopy [24, 32, 86, 93]. The UV-Vis spectra of ZnO thin films could be measured as transmittance, absorbance or reflectance. The energy band gap E_g can be usually extracted from these spectra using the Tauc relation.

From the literatures, ZnO thin films generally exhibited high optical transmittance in the visible region [24, 86, 93, 94]. Under the thickness effect, the average transmittance generally found to be decrease with increasing the thickness [17, 95]. The absorption edge in the transmittance spectra of ZnO thin films shifts towards higher wavelength region by the increasing of thickness [6, 96].

The optical band gap (Eg) values of the ZnO thin films found to be increase with increasing the film thickness [16, 74, 78, 81, 96, 97]. However, a decrease is also noticed in the literature [24, 31, 32, 93]. In one case, band gap was not influenced by the thickness variation **(Table II.1)** [82] .

Photoluminescence (PL) spectra are required to investigate the levels and amounts of defects in ZnO thin films. A few works investigating the thickness effect on the properties of ZnO thin films used PL spectroscopy [74, 80-82, 97-100]. The emission peaks occurred in the PL spectra are a result of the transitions between; VB, CB, and various created levels of defects.

The near-band-edge (NBE) emission, which normally ranges between 375 and 387 nm wavelength, and it appear due to recombination of free excitons between conduction band (CB) and valence band (VB), was observed in all of these works. Also, it is observed that the increasing of thickness increases the intensity of NBE peaks, which indicate the good crystallinity of films

while the thickness increase. The better crystalline quality of the films leads to better optical properties [80].

Another emission peaks can be seen with the NBE emission peak in the PL spectra, which recorded in these studies. However, in one case, the NBE peak appeared alone for samples prepared by RF sputtering [74]. Broad green emission peak at 518 nm [81], weak and broad peak in the blue range at 468 nm [98] and green-yellow band [99] were observed. The origin of these emissions is not clearly understood yet. However, many researchers were suggested their origin [53]. As the film thickness increase, the intensity of the above-mentioned peaks increases, which indicates the presence of more defects in the ZnO films.

Table II. 1. Film thickness effects on the different physical properties of pure ZnO prepared via different techniques

Deposition method	Thickness range (nm)	Substrate	Changes in the film properties when increasing the thickness						ref
			PO	Lattice constants	CS	BG	GS	RMS	
sol–gel spin coating	65 - 600	glass	(002)	NP	increase	NP	increase	NP	[101]
sol–gel spin coating	120 - 320	glass	(101)	NP	increase	constant	increase	NP	[82]
sol–gel spin coating	14.2 - 62.7	glass	(101)	NP	NP	increase	increase	NP	[97]
sol–gel dip coating	50 - 350	sapphire (0001)	(002)	NP	increase	NP	increase	NP	[23]
sol–gel spin coating	80 - 620	alumina	(002)	NP	increase	NP	increase	increase	[20]
sol–gel dip coating	98 - 366	glass	(002)	NP	increase	decrease	increase	increase	[28]
sol–gel dip coating	NP 1-7 coats	glass	(101)	NP	NP	NP	NP	NP	[102]
sol–gel spin coating	15 - 208	Corning glass (7059)	(002)	NP	increase	increase	increase	decrease	[103]
sol–gel spin coating	58 - 77	glass	(002)	NP	decrease	decrease	NP	NP	[104]
sol–gel spin coating	60 - 180	silicon	(002)	decrease	increase	increase	NP	decrease	[105]
spray pyrolysis	600 - 2350	glass	(101)	decrease	increase	increase	NP	increase	[16]
spray pyrolysis	355 - 445	glass	(002)	increase	increase	increase	increases	NP	[106]
spray pyrolysis	200 - 500	quartz	(002)	NP	NP	decrease	NP	NP	[107]
nebulizer spray pyrolysis	225 - 1138	glass	(002) (101)	slightly increased	increase	decrease	NP	increase	[29]

Spray-ILGAR	100 - 720	glass	(002)	decrease	increase	increase	NP	increase	[81]
spray pyrolysis	46 - 317	glass	(101)	NP	NP	decrease	NP	increase	[17]
RF Sputtering	31 - 280	glass	(002) (103)	decrease	increase	increase	increase	increase	[78]
RF Sputtering	190-342	p-Si/glass	(002)	decrease	increase	increase	increase	increase	[74]
RF Sputtering	160-398	p-type silicon and glass	(100)	NP	increase	decrease	increase	increase	[30]
RF Sputtering	70 - 1800	glass	(002)	NP	increase	decrease	increase	NP	[24]
RF magnetron Sputtering	NP	glass	(002)	NP	increase	increase	NP	increase	[84]
RF magnetron Sputtering	75.5 - 130.5	corning (7059) glass	(002)	NP	increase	NP	NP	NP	[108]
D.C magnetron sputtering	75 - 250	glass	(002)	NP	increase	decrease	NP	NP	[31]
DC magnetron sputtering	12 - 50	fused silica	(002)	NP	increase then decrease	decrease	NP	NP	[93]
DC magnetron sputtering	50 - 600	Polyethylene terephthalate	(002)	NP	increase	NP	NP	NP	[109]
PLD	50 - 3200	sapphire (0001)	(002)	NP	increase	NP	NP	NP	[99]
PLD	40 - 2400	sapphire (0001)	(002)	NP	increase	NP	NP	increase	[80]
PLD	150 - 240	Corning glass	NP	NP	NP	increase	NP	NP	[110]
PLD	20 - 216	glass	(002)	NP	increase	increase	increase	increase	[96]
PLD	10 - 200	Corning glass	NP	NP	NP	increase	NP	NP	[95]
ALD	5 - 70	silicon and fused quartz	(002)	NP	NP	increase	NP	NP	[6]

ALD	43 - 225	silicon (100)	(002)	NP	increase	decrease	NP	NP	[88]
ALD	70 - 220	Si (100)	(002)	NP	increase	NP	increase	NP	[111]
PFCVAD	139 - 427	glass	(002)	increase	increase	decrease	NP	NP	[32]
PFCVAD	100 - 400	Si and SiO2/Si	NP	NP	NP	increase	NP	NP	[112]
MOCVD	5 - 55	sapphire	(002)	NP	NP	NP	NP	NP	[113]
SILAR	50 - 350	glass	(002)	NP	increase	decrease	NP	increase	[33]
Thermal evaporation	50 - 250	glass	NP	NP	NP	decrease	NP	NP	[19]
PA-MBE	50 - 300	Si and porous silicon (PS)	(002)	NP	increase	NP	increase	increase	[87]
ultrasonic spray	NP (growth time)	glass	(002)	decrease	Increase then decrease	increase	NP	NP	[89]

PA-MBE: Plasma-assisted Molecular Beam Epitaxy
ALD: Atomic Layer Deposition
PLD: Pulsed Layer Deposition
SILAR: Successive Ion Layer Adsorption and Reaction
MOCVD: metal organic chemical vapor deposition
PFCVAD: pulsed filtered cathodic vacuum arc deposition
PO: Preferential Orientation
CS: Crystallite Size
BG: Band Gap
GS: Grain size
RMS: Root Mean Square
NP: Not provided

II.5.2 Thickness effect of Mn-doped ZnO

II.5.2.1 Structural properties

The X-ray diffraction (XRD) data of all works investigating the thickness effect of Mn-doped ZnO thin films, exhibited totally (002) preferred orientation which means that c-axis is perpendicular to the substrate surface. It is observed that the Mn- doped ZnO thin films prepared by RF magnetron sputtering are free from any other secondary phases [26, 27, 114]. However, a formation of $ZnMnO_3$ phase was observed for Mn-doped ZnO thin films prepared by sol–gel dip coating method [25]. It should be noted that the intensity of (002) peak increases as the film thickness increases.

In few studies investigating the thickness effect of Mn- doped ZnO thin films, the variation of film thickness, generally, influenced the different XRD parameters. It is observed that the lattice constants a = b and c, which are usually calculated from XRD patterns, increase with increasing of the thickness [26]. An exception was noted where the lattice parameter almost constant **(Table II.2)** [25]. It is also found that the increasing of thickness influences the crystallite size (D). All studies present an increase of the crystallite size with increasing the thickness **(Table II.2)**.

II.5.2.2 Morphological properties

For surface morphology, in the studies investigating the thickness effect of Mn- doped ZnO thin films, only Scanning Electron Microscopy (SEM) or Field Emission Scanning Electron Microscopy (FESEM) were used [25-27].

For 3% Mn- doped ZnO thin films deposited on Si substrate by RF magnetron sputtering, their FESEM images showed granular surface with uniform distribution of tightly packed hexagonal structured grains for smaller thickness. As the film thickness increases, the growth of grains with 4-sided pyramid structures of varying sizes are randomly observed [26].

Also, for 5% Mn- doped ZnO thin films deposited on fused quartz substrate by the RF magnetron sputtering, the FESEM images of the films showed clusters of small grains with porous nature. With increase the thickness of film the cluster with high packing density appear distinctly. The grain size within the cluster decreases with increase in thickness **(Table II.2)** [27].

In the SEM images, an island surface morphology of thin films deposited by sol- gel dip coating method on soda lime glass was observed. Crystallites of small size are gathered on the surface of the thin films. Crystallites are uniformly and mono-dispersedly distributed on the films. With the increase of films thickness, agglomeration of particles increases.

II.5.2.3 Electronic and optical properties

The thickness effect on the electronic and optical properties of Mn-doped ZnO thin films were studied [25-27, 114]. The transmission (T) in the visible region of 5% Mn- doped ZnO thin films deposited on fused quartz substrate range is 90% and it is not affected significantly with increase in film thickness [27]. However, the optical transmission of Mn- doped ZnO films deposited by sol- gel dip coating method on soda lime glass, shows a decreases with increasing the withdrawal speed of substrate [25]. Also, for 3% Mn- doped ZnO thin films deposited on Si substrate by RF magnetron sputtering, the optical transmittance of different thickness deposited on quartz glass shows a large transmittance for smaller thickness and decreases at larger thickness [26].

The optical band gap (Eg) values of the Mn- doped ZnO thin films is found to be decreased with increasing the film thickness **(Table II.1)** [25-27].

The PL analysis of Mn-doped ZnO thin films with thickness were also studied [26, 114]. Both studies show near-band-edge (NBE) emission due to the recombination of free excitons.

Another set of emission peaks can be seen in the PL spectra. for 5% Mn- doped ZnO films grown on Si (100) and Si (111) substrates by RF magnetron sputtering, blue band (BB) emission at around 2.8 eV, green band (GB) emission at around 2.5 eV and yellow band (YB) emission at around 2.4 eV have been observed in both cases of substrates. Also, NBE showed red and blue shift with the increase of thickness [114]. For 3% Mn- doped ZnO films grown on quartz substrates by RF magnetron sputtering, the PL spectra shows a broad visible emission in violet-blue region, sharp near band emission at 378 nm. For larger thickness, the intense broad visible emission is observed.

Table II. 2. Film thickness effects on the different physical properties of Mn- doped ZnO thin films prepared via different techniques

Deposition method	Thickness range (nm)	Mn content mol%	Substrate	Changes in the film properties when increasing the thickness						ref
				PO	LC	CS	BG	GS	RMS	
sol–gel dip coating	150 – 350 withdrawal speed mm/s	NP	soda lime glass	(002)	Almost constant	increase	decrease	NP	NP	[25]
RF magnetron sputtering	50 - 190	3	quartz glass	(002)	increase	increase	decrease	NP	NP	[26]
RF- sputtering in nitrogen gas	398- 1650	5	Fused quartz	(002)	NP	increase	decrease	increase	NP	[27]
RF magnetron sputtering	15 - 105	5	Si (100) Si (111)	(002)	NP	increase	NP	NP	NP	[114]

PO: Preferential Orientation
CS: Crystallite Size
BG: Band Gap
GS: Grain size
RMS: Root Mean Square
NP: Not provided

III. Experiments and DFT details

III.1 Experimental details

In the first part of this chapter, we present the synthesis techniques of ZnO thin films. Our attention is paid to the sol-gel technique used in this study to prepare the films of pure ZnO and Mn-doped ZnO. Then, we describe the experimental protocols and the characterization techniques which used in this work.

III.1.1 ZnO thin films deposition techniques

Generally, there are a wide variety of physical and chemical thin films deposition methods. The chemical methods split into solution deposits and vapor phase deposits, which include together, spray pyrolysis, electrochemical deposition, and sol-gel processes. For the physical methods, we find deposition techniques such as, evaporation, laser ablation, molecular beam epitaxy, pulsed-laser deposition, and atomic layer deposition (**Figure III.1)**.

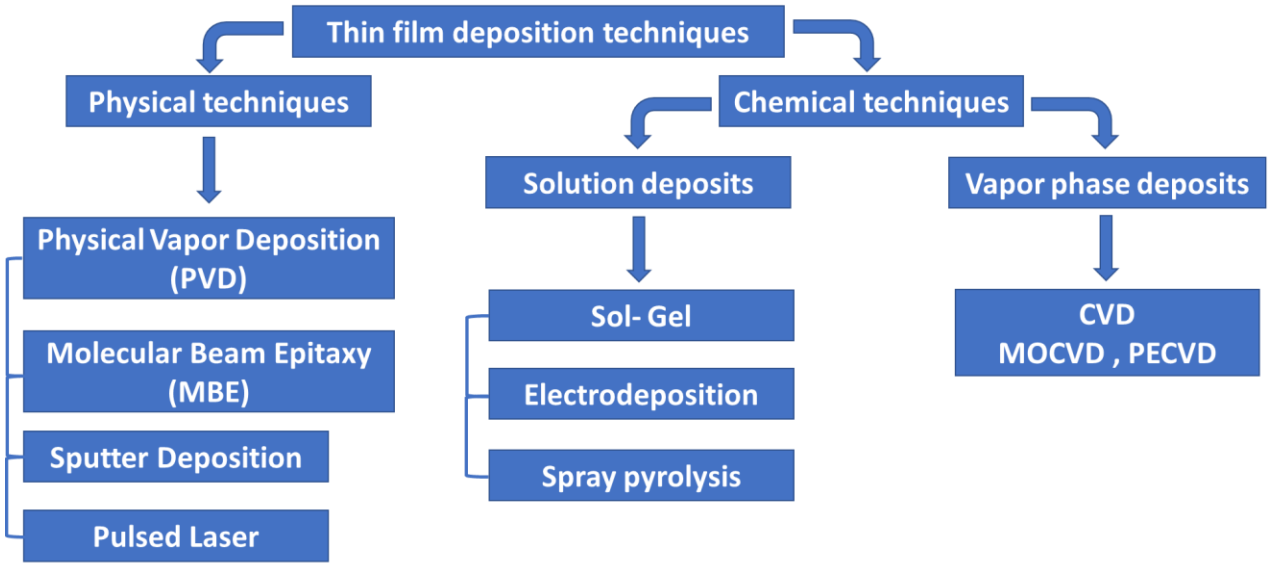

Figure III. 1. Different thin films deposition techniques

Every technique has its own advantage and can produce various ZnO nanostructures. Because of its good homogeneity, ease of controlling composition, low processing temperature, large-area coating, low equipment cost, and good optical properties, the sol–gel process is one of the most widely used methods in the synthesis of ZnO nanoparticles [75].

III.1.2 The sol-gel technique

The sol-gel (solution- gelation) technique is widely used to prepare oxides. It occurs at low temperatures through a hydrolysis and condensation reaction. Since the second half of the twentieth century, this gentle chemistry method has been in use.

The basic principle of the sol-gel process is as follows: a liquid-phase solution based on precursors is transformed into a solid by a series of chemical reactions such as polymerization at low temperature. The cycle, which consists of the following stages: pulling, centrifugation, drying, and annealing, can be repeated several times to obtain a multi- layered final film.

III.1.2.1 The precursor

The precursor is the main material that allows the chemical reaction to occur in the sol–gel process. The two main groups of precursors are: metal salts of which its general formula M_nX_n, (chlorides, nitrates, oxychlorides) and the metal alkoxide compounds of formula $M(OR)_n$ where M denotes a metal atom of valence n and R is an alkyl chain of formula ($C_nH_{2n\pm1}$).

Sol-gel synthesis routes: There are two routes of sol-gel synthesis which are [115]:

- Inorganic or colloidal route: obtained from metal salts (chlorides, nitrates, oxychlorides) in aqueous solution. This route is inexpensive but difficult to control, which is why it is still very little used. However, this is the preferred route for obtaining ceramic materials.
- Metal-organic or polymeric route: obtained from metal alkoxides in organic solutions. This route is relatively expensive but allows fairly easy control of the particle size.

III.1.2.2 Sol-Gel reaction steps:

The Sol-Gel reaction is carried out in two steps: the synthesis of the “sol” then the formation of the “gel” (**Figure III.2**) [116-118].

a)- The synthesis of "sol"

A sol is defined as a stable dispersion in a liquid of colloidal particles. The synthesis of a "sol" is by adding water to an acidic or basic organic solution containing precursors. This is the hydrolysis reaction. Subsequently, this “sol” can be made to evolve by means of condensation reactions into a three-dimensional network with infinite viscosity, called “gel”.

Hydrolysis reaction:

$$\mathbf{M\text{-}(OR)_n + H_2O \rightarrow (OR)_{(n-1)}\text{-}M\text{-}OH + R\text{-}OH}$$

b)- Formation of "gel"

A gel is defined as a two-phase system in which the solvent molecules (water, alcohol) are trapped in a solid network. When the liquid is water, we speak of an aquagel or hydrogel, if it is alcohol, we speak of alcogel.

Condensation-polymerization reaction

$$\mathbf{(OR)_{(n-1)}\text{-}M\text{-}OH + (OR)_{(n-1)}\text{-}M\text{-}OH \rightarrow (OR)_{(n-1)}\text{-}M\text{-}O\text{-}M\text{-}(OR)_{(n-1)} + H_2O}$$

c)- Drying

Obtaining a material from the gel goes through a drying step which consists of removing the solvent outside the polymer network. This drying can cause shrinkage in volume. The drying process for obtaining the sol-gel material requires that the alcohol, or water, can escape as the gel solidifies. The evaporation process occurs through existing holes and channels in the porous solgel material. There are several types of drying that allow you to obtain different types of materials:

- The gel can be dried under mild conditions (normal evaporation). It hardens by compacting: it is a xerogel (subsequent application to form dense glasses and ceramics).
- The gel can be dried under supercritical conditions (high and constant evaporation rate) to form a very compact gel: it is an airgel (very open structure with high macroporosity).

d)- Annealing (heat treatment)

This phase is essential in the formation of the material. Annealing has two main functions:

- Elimination of organic species in the starting solution (organic groups of the Alkyl type (-OR-))
- Crystallization and densification of the material. It is only after this annealing that the desired material can be obtained.

Annealing is generally carried out at temperatures between 300 ° C and 700 ° C.

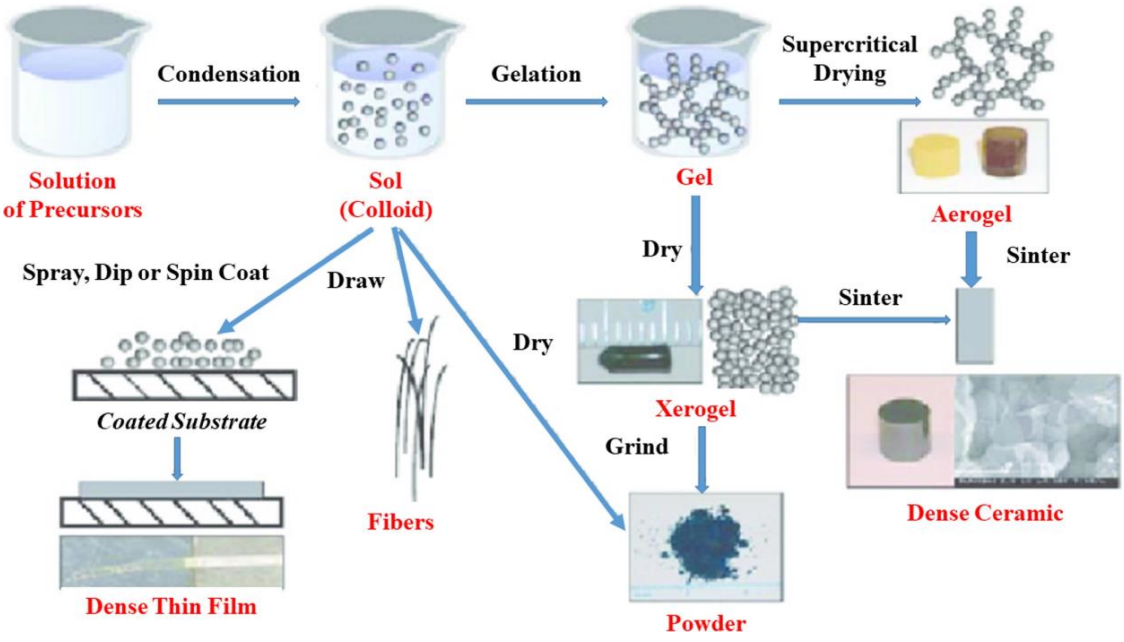

Figure III. 2. Main steps in the synthesis of a material by the sol-gel route [117]

III.1.2.3 Sol-gel thin film deposition techniques

The two best known processes for producing thin films with control of the deposited thickness are dip-coating and centrifugal coating (spin coating). Both are used at room temperature and pressure. The thicknesses of the films are controlled by varying the deposition rate.

a)- Dip-coating

This method simply involves immersing the substrate in the solution containing the "sol" followed by pulling at a predefined withdrawal rate under controlled temperature and pressure conditions (**Figure III.3**). During the ascent, the liquid will flow onto the substrate. At the end of the flow, the substrate is covered with a uniform and porous film.

This technique makes it possible to produce, in a single operation, deposits on both surfaces of the substrate. The thickness of the films can vary from 100 nm to a few micrometers.

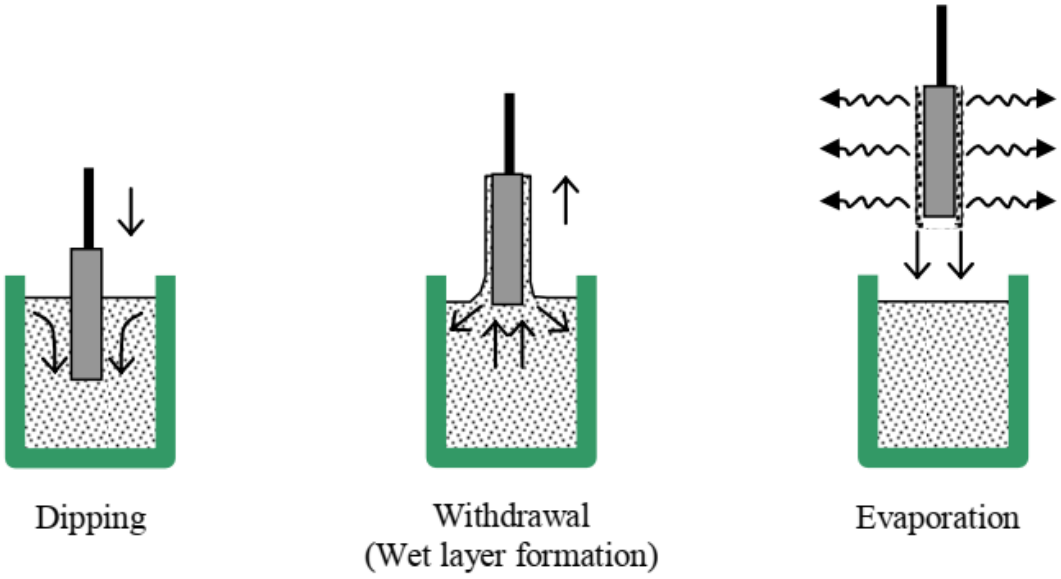

Figure III. 3. Scheme of the dip coating process [119].

b)- Spin-coating

In this method, a drop of solution is deposited in the center of a substrate fixed on a rotating horizontal support **(figure II.4)**. The spinning spreads the solution by centrifugation until a uniform film is obtained. This deposit method can be broken down into four steps:

a. The deposit of the solution.

b. The start of rotation: The acceleration phase causes the liquid to flow out of the substrate.

c. The constant speed rotation allows excess liquid to be ejected in the form of droplets and the film thickness to decrease evenly.

d. The evaporation of the most volatile solvents which accentuates the reduction in the thickness of the deposited film.

Figure III. 4. Scheme of the Spin-coating process [120].

III.1.3 Synthesis of ZnO and Mn-doped ZnO thin films

In this work, we deposit pure, 4% and 7% Mn-doped ZnO thin films on glass substrates with different thickness using the sol- gel spin coating technique. This technique consists of several steps which are summarized schematically in the flowchart (**Figure III.5)**.

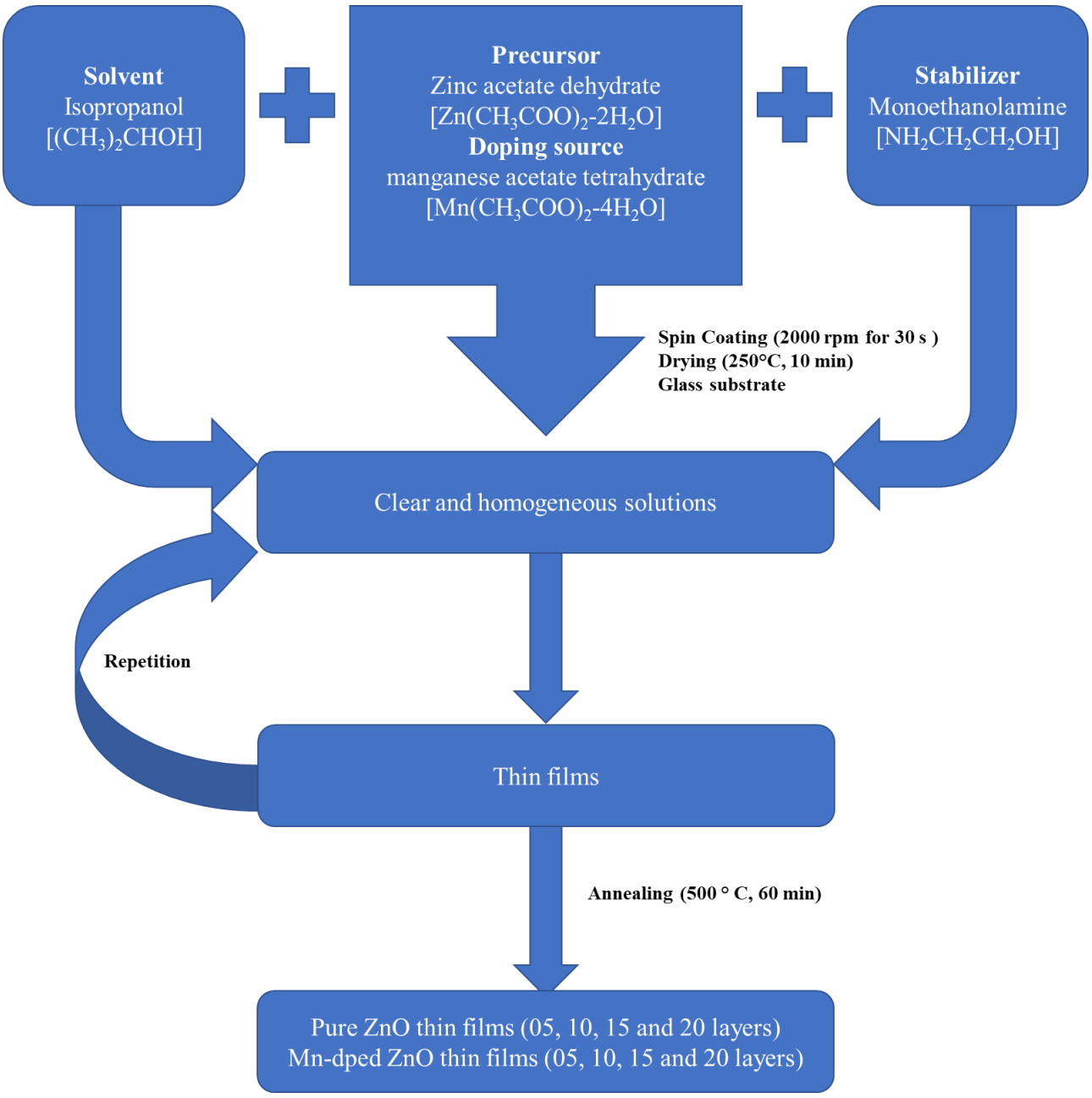

Figure III. 5. Chart of thin films preparation procedures of pure Zinc Oxide (ZnO) and doped with manganese with different thickness by sol gel spin coating.

III.1.3.1 Preparation of "sol" solutions

a) Preparation of pure solution

In this work, to synthesis pure ZnO thin films, a solution of 0.7 M was prepared by dissolving the precursor, zinc acetate dihydrate [$Zn(CH_3COO)_2$-$2H_2O$], in isopropanol (2-Propanol) [$(CH_3)_2CHOH$]. Then, after 15 minutes of magnetic stirring, monoethanolamine [$NH_2CH_2CH_2OH$] was added drop by drop to the solution as stabilizer (**Table III.1**). The molar ratio of the monoethanolamine to ion metal was fixed at 1. The clear, homogeneous and transparent solution was stirred at 65°C for 1 h and aged at room temperature for 24 h.

b) Preparation of the doped solution

To prepare the doped films, Manganese Acetate Tetrahydrate [Mn $(CH_3COO)_2$-$4H_2O$] and zinc acetate dihydrate [Zn $(CH_3COO)_2$-$2H_2O$] were mixed together at 4% and 7% mol concentration and were dissolved to form the solutions. Then, the same steps were followed as in pure ZnO solution (**Table III.1**).

III.1.3.2 Preparation of substrates

The used substrates in our work are glass slides **(Figure III.6)**. This choice was adopted for a variety of reasons, including: its thermal dilation coefficient which is very close to the thin layer of ZnO ($\alpha_{glass} = 8{,}5.10^{-6}\ K^{-1}$, $\alpha_{ZnO} = 7{,}2.10^{-6}\ K^{-1}$) so minimizing the constraints at the layer-substrate interface, its transparency allows us to perform a good optical and electrical characterization.

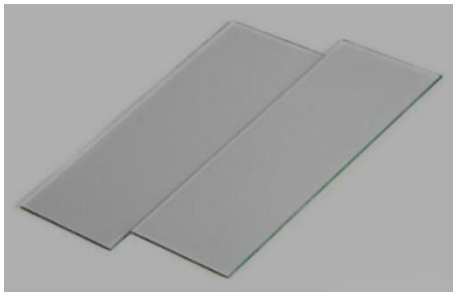

Figure III. 6. Glass slides for substrates

a) Cleaning of substrates

Before the deposition of pure and doped ZnO thin films, the glass substrates must be cleaned and free of grease, dust and scratches. Cleaning the substrates is an essential step because it determines the adhesion and homogeneity of the deposited layers, as well as the uniformity of their thicknesses.

Table III. 1. Different chemical elements used in the preparation of solutions

Zinc acetate dehydrate: The precursor (Figure III.6a)	**Manganese Acetate Tetrahydrate: Source of Mn (Figure III.6b)**
Formula: **[$Zn(CH_3COO)_2$-$2H_2O$]**. Form: **Solid**. Color: **White.** Melting point: **237 ° C.** Molar mass: **219.49 g / mol.** Density at 20 ° C: **1.74 g / cm^3.** Solubility in water at 20 ° C: **430 g / l** 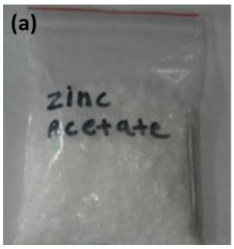	Formula: **[Mn(CH3COO)2-4H2O]** Form: **Solid.** Color: **Pink.** Melting point: **80 ° C.** Molar mass: **245.087 g / mol.** Density at 20 ° C: **1.59 g / cm^3.** Solubility in water at 20 ° C: **700 g / l** 
Isopropanol: Solvent	**Monoethanolamine: Stabilizer**
Formula: **[(CH3)2CHOH].** Form: **Liquid.** Color: **Colorless.** Molar mass: **60.1 g / mol.** Density: **0.786g / cm^3.** Boiling point: **82.2 ° C.** 	Formula: **[$NH_2CH_2CH_2OH$].** Form: **Liquid.** Color: **Colorless to yellow.** Molar mass: **61.08 g / mol.** Density: **1.01 g / cm^3.** Boiling point: **170 ° C.** 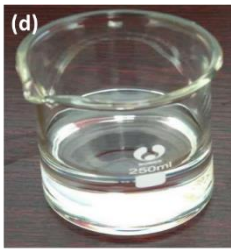

The cleaning of the substrates was carried out according to the following procedures: At first, ultrasonic cleaning bath with acetone for 10 minutes. Then, cleaning for 10 minutes in ethanol, and then rinsed in deionized water for 10 min. After that, dried and stored away from all kinds of impurities or dust.

III.1.3.3 Thin films deposition by Spin coating

After cleaning the substrates and preparing the pure and manganese doped ZnO solutions, the deposition process is carried out directly by the spin-coating technique (centrifugation) **(Figure III.4)**. This simple technique consists in the deposition of a few drops of the aged solution on the substrate surface which installed on a rotating support using a micropipette. the substrate rotates at a controlled speed (2000 rpm for 30s). This step allows the solution to be distributed (uniformly) over the entire surface of the substrate. To evaporate the solvent and remove organic residuals, the deposited films were preheated in a furnace at 250°C for 5 min. The process of coating and preheating was repeated (05, 10, 15 and 20 times) to increase the film thickness.

III.1.3.4 Annealing of thin films

After the deposition of the pure, 4% and 7% manganese doped ZnO thin films on the glass substrate with different thicknesses, to remove the organic species available in the starting solution, and to densify the final material, the samples were annealed in a furnace at 500 ° C for 1 hour. After all of these deposition procedures, the samples become ready for characterization.

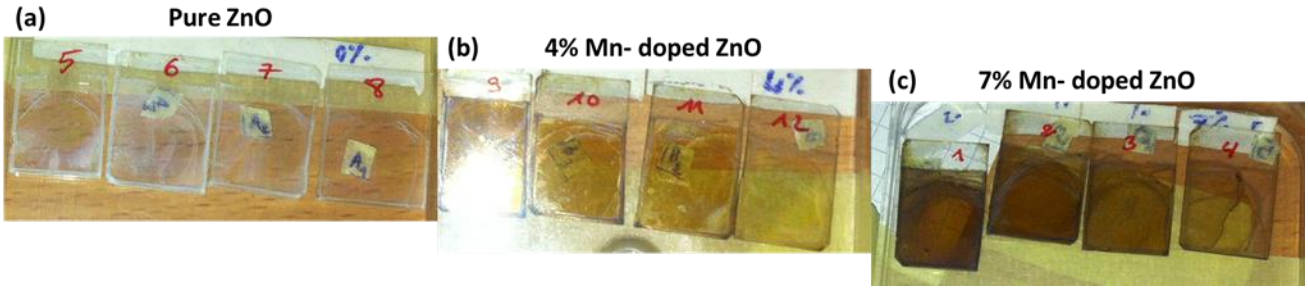

Figure III. 7. The prepared samples; (a) pure ZnO, (b) 4% Mn-doped ZnO and (b) 4% Mn-doped ZnO thin films deposited on glass substrate.

III.1.4 Characterization techniques

The pure, 4% and 7% Mn-doped ZnO thin films synthesized by the sol-gel technique were characterized by: X-ray diffraction for the structural properties, atomic force microscopy (AFM) and Field emission scanning electron microscopy (FESEM) for the morphological properties and UV-Visible and photoluminescence (PL) for the optical and electronic properties. The mechanical profilometer were used for thickness measurements.

III.1.4.1 Thickness measurement by Profilometer

The thickness measurements of our pure and Mn-doped ZnO thin films were carried out using Stylus Profilometer (model: D 500) **(Figure III.8a)**. To perform the measurements, the sample is placed on a specimen holder and a stylus (diamond tip) is brought into contact with the sample surface **(Figure III.8b)**. After having determine the step between the substrate surface (the area where there is no deposit) and the deposit surface, we set a distance to be traveled by the stylus between the two surfaces, the scanning time (speed) and the stylus pressing force, the vertical displacement of the stylus is recorded as a function of its position on the sample **(Figure III.8c)**. Generally, to make thickness measurements by profilometer, the creation of a physical

walk is mandatory. There are several methods to achieve this walk such as chemical attack. In our case, to create the step, we hid part of the substrate during the deposition of the thin layers.

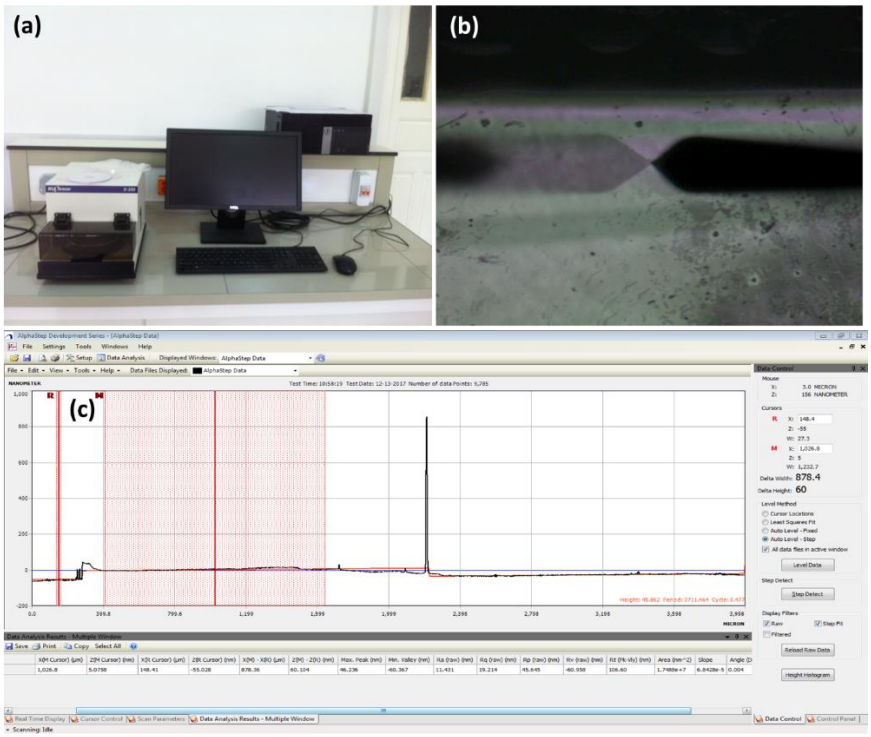

Figure III. 8. Thickness measurement; (a) Stylus Profilometer (model: D 500) (b) Contact of the stylus (diamond tip) on the sample surface and (c) Vertical displacement record of the stylus.

III.1.4.2 X-ray diffraction (XRD) analysis

The structural properties of samples (powders or thin films) could be obtained by X-ray diffraction (XRD). This technique allows to obtain a lot of information about the samples: crystallization, presence of parasitic phases, crystallographic parameters, orientation, grain size and the stresses.

The principle of this technique is based on Bragg's law, which is the law governing the diffraction of X-rays on a crystal. It was discovered by Sir William Henry Bragg and William Lawrence Bragg around 1915. This law establishes a link between the distance between the crystal

atoms $d_{(hkl)}$ and the angles at which are the scattered X-rays hitting the crystal θ **(Figure III.9a)** [121].

$$2d_{hkl} \sin \theta_{hkl} = n\lambda \quad \text{(III.1)}$$

Where:

d = Interreticular distance, ie distance between two crystallographic planes;

θ = X-rays angle incidence on the surface of the studied material;

n = order of reflection;

λ = X-rays wavelength.

Since Miller indices can be used to identify the crystallographic planes, we can index the diffraction peaks using these indices. For a given d_{hkl} value, and an incident X-ray with a fixed wavelength, the diffracted intensity can only be seen at 2 θ_{hkl} which represents a diffraction cone formed by the diffracted and incident rays. The phases present in a sample are identified by comparing its spectrum (positions and intensities of the diffracted lines) to known phase spectra[122].

In this study, The XRD analysis was carried out using the Philips "X'PERT PRO MPD" diffractometer in θ-θ mode (Bragg-Brentano configuration), equipped with a vertical goniometer with a 240 mm radius and fitted with a ray tube with copper anticathode. The interfaced detector is of the PIXcel-1D type.

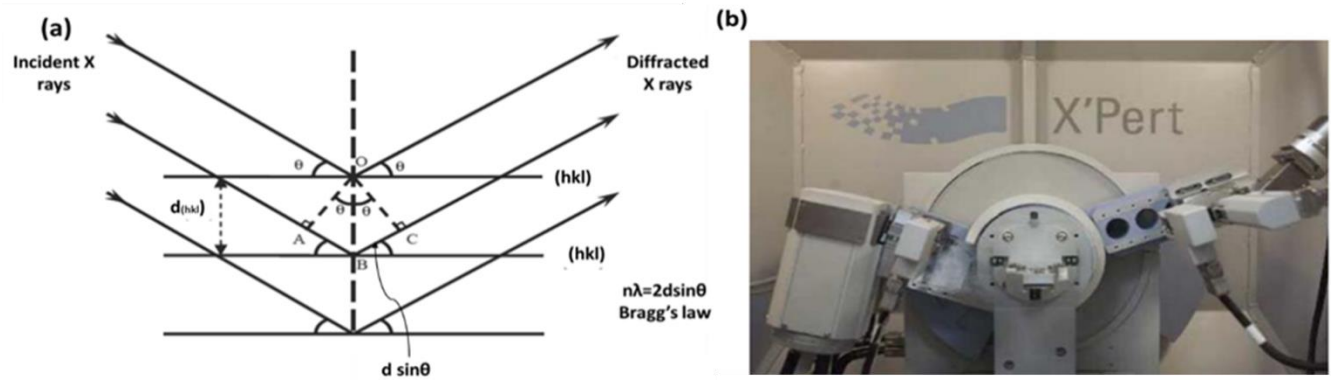

Figure III. 9. XRD analysis; (a) Principle of X-ray diffraction (b) X'Pert PRO MPD diffractometer.

III.1.4.3 Atomic force microscopy (AFM)

Atomic force microscopy (AFM) is one of the most common technique for surface analysis. This technique developed in 1986 by researchers Gerd Binning, Calvin Quate, and Cristoph Gerber in collaboration with IBM and Stanford University. The AFM allows extreme magnifications in the x-, y-, and z-directions, which facilitates atomic scale imaging with high resolution. So, this method led to see the shape of a surface in three-dimensional (3D) detail down to the nanometer scale. AFM can image all type of materials and do not require any special sample preparation [123].

This technique is essentially based on the scanning and measurement of interatomic forces between an ultra - sharp tip (radius less than 10 nm), which is attached to flexible cantilevers, and the sample surface at very short distance (0.2–10 nm tip-sample separation) **(Figure III.10)**. These interaction forces, which could be Van der Waals forces, electrostatic forces, magnetic forces or even ionic repulsion forces, can be described using Hooke's law: $F = - k x$. where F is the tip-sample force, k is the spring constant of the cantilever, and x is the extent of cantilever deflection [123]. This cantilever deflections resulting from variations in force between the tip and the sample during scanning are most often measured by optical detection. A laser beam is focused on the back

of the cantilever, which can move in all x, y, z directions, then reflected in a photodiode constituting the detector. The direction changes result a difference in light intensity and therefore a voltage difference. Thus, they are recorded and transmitted to the computer system to allow an analysis and a three-dimensional representation of the surface [124].

The flexible cantilever can move in all x, y, z directions using a piezoelectric scanner. The x, y scan can range from a few nanometers to a few hundred micrometers. The z-sensitivity is on the order of a fraction of nanometer, and the z-shift can be up to a few micrometers. The sample is fixed on a device composed of piezoelectric ceramics allowing movement in the three directions of XYZ space with an accuracy of the order of a tenth of an angstrom.

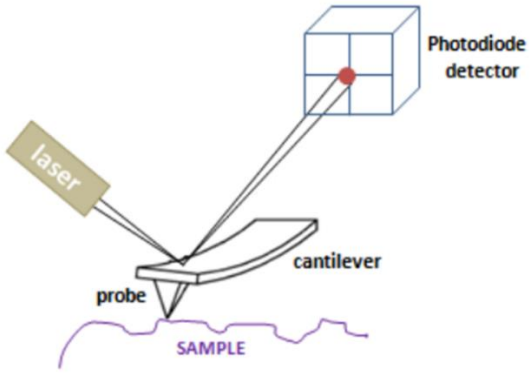

Figure III. 10. Concept of AFM and the optical lever

The AFM can operate in several modes which can be grouped in two categories: contact mode (static) and tapping mode (dynamic) **(Figure III.11)** [125].

Contact mode: in this mode, the cantilever with the tip presses on the sample. A repulsive force between the surface and the tip is created because of repulsion of electrons from the sample and the tip. In this case, the weak interaction between the sample and the tip is kept constant by

changing the height of the sample. The variation in height gives the height of the surface at the studied location **(Figure III.11a)**.

Tapping mode or intermittent contact: this is the most commonly used mode. In this mode, the cantilever oscillates at a given frequency of about 100 kHz and at a fixed amplitude. In this case, the sample exerts a short-range (van der Waals-type) attractive force on the cantilever and the tip. The amplitude of the oscillation changes. It is kept constant by moving the height z of the sample **(Figure III.11b)**.

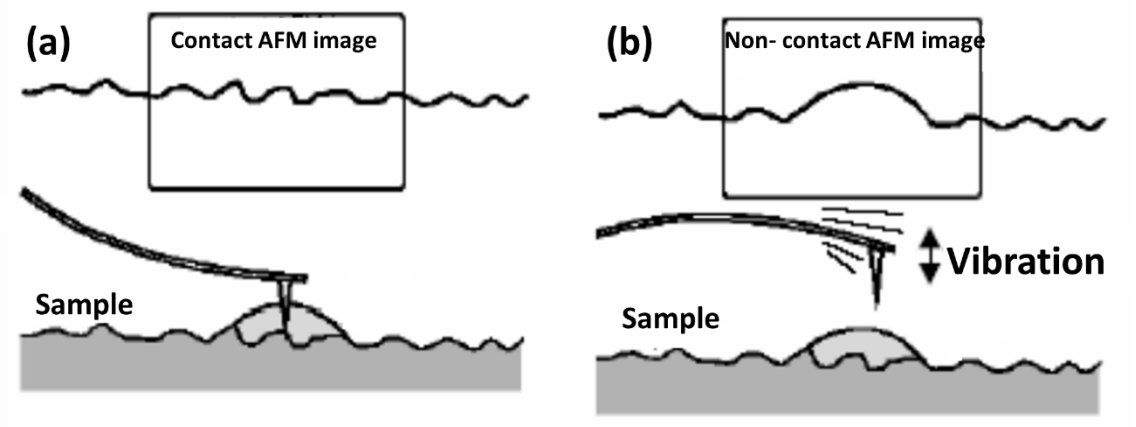

Figure III. 11. AFM modes; (a) contact mode and (b) tapping mode.

AFM measurements of our pure, 4% and 7% Mn doped ZnO thin films were recorded in non-contact mode using Asylum Research, MFP-3D Classic model **(Figure III.12)**. The images were analyzed by the WSxM 5.0 software program (Nanotec Electronica S.L.) [126].

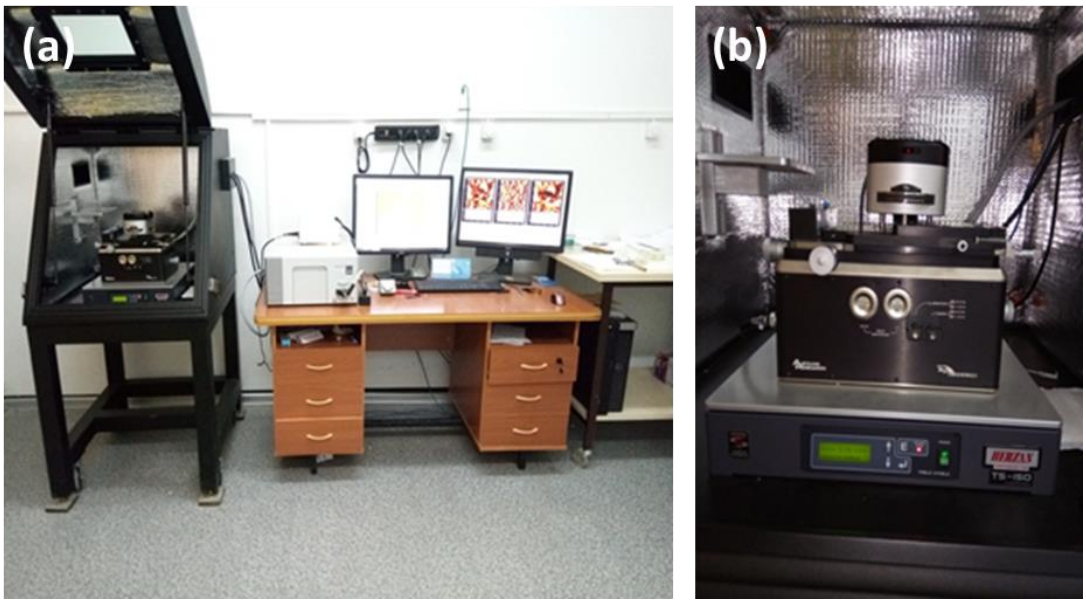

Figure III. 12. Atomic Force microscopy; (a) Image of the used microscope Asylum Research, MFP-3D Classic model and (b) Sample holder.

III.1.4.4 Scanning electron microscope

Scanning electron microscopy SEM is one of the most used instruments in research areas and semiconductor industries due to its large depth of field which allows a large amount of the sample to be in focus at one time and produces an image that is a good representation of the surface topography and due to its high resolution, which makes possible the examination of features at high magnification. It is also a non-destructive technique that provides information on the morphology of the sample, its mode of crystallization, sometimes to estimate the crystallites sizes and the thickness of the sample from cross sectional view [127].

SEM is based on the electron-matter interaction. Its principle consists of sweeping, point by point, the surface of the analyzed sample, which is placed in a maintained column under a secondary vacuum, by an energetic electron beam of some ten kilovolts. The electrons are generated by a thermionic emission or field emission gun. These so-called "primary" electrons are

focused on the surface of the sample by a system made up of a set of electromagnetic lenses. The interaction of the electron beam with the sample leads to the emission of different particles and radiations such as: secondary electrons, backscattered electrons, Auger electrons and X-rays. This emission occurs in a volume having the shape of a pear, of which the size is on the order of cubic micron (**Figure III.13a)**. A detector collects a mixture of the various types of radiation emerging from this volume and the resulting signal is amplified and displayed on a cathode ray tube (CRT) or television screen scanning synchronous with the scan on the specimen. The signals carry topological, compositional and crystallographic information about the sample and in particular secondary electrons give information about morphology and topography whereas backscattered ones provide compositional contrast (**Figure III.13b)** [127, 128].

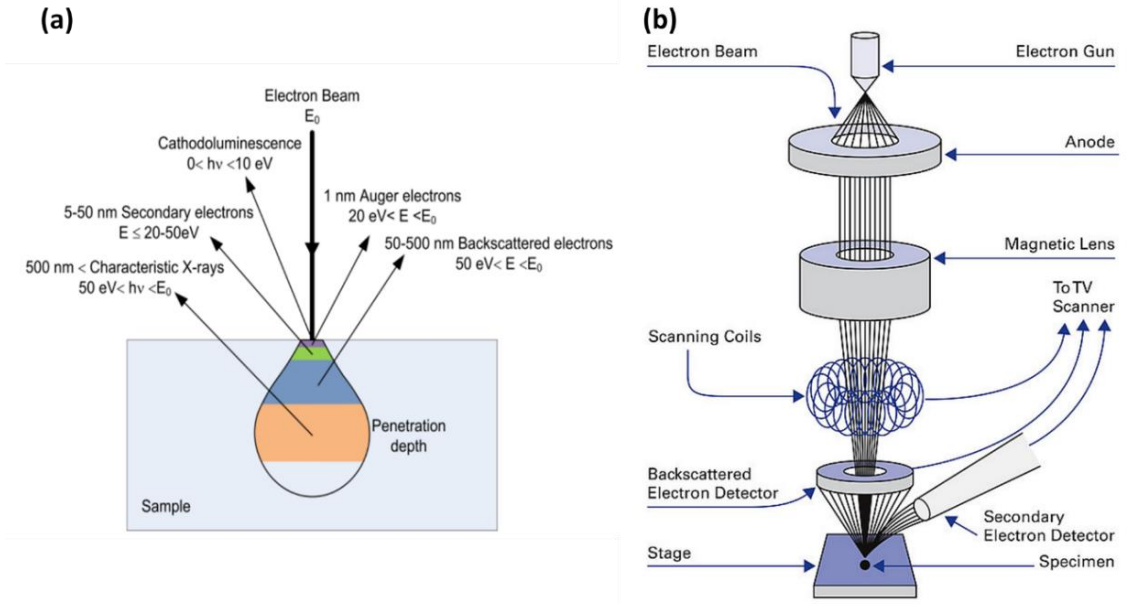

Figure III. 13. Scanning electron microscopy; (a) Effects produced by electron bombardment of a specimen [127] and (b) Principal design of a scanning electron microscope [129].

The used scanning electron microscope in this work, for observing the surface morphology, is of type (FESEM; Zeiss Supra 35 VP) Scanning microscope (**Figure III.14**).

Figure III. 14. Image of the used scanning electron microscopy Zeiss Supra 35 VP.

III.1.4.5 UV-visible spectroscopy

UV-Visible spectrophotometry is an optical characterization method used to study the optical properties of a material such as the transparency, the refractive index, extinction coefficient, energy gap, etc., from the detection of the transmitted (T), absorbed (A) or reflected (R) radiation. These are the three possible radiation when an incident beam of intensity strikes a sample. According to the frequency of the incident radiation, the radiation-matter interaction involves various types of energy levels of matter. The involved energies have the same magnitude order as molecule binding energies, and this radiation can also cause bond breaks. More generally, they cause electronic transitions between the different energy levels of molecules. The type of obtained information will depend on the sensitivity apparatus and the nature of the sample.

The UV-vis absorption spectroscopy provides information of absorption light as a function of wavelength, which describes the electronic transitions occurring in the measured samples. The

UV-vis spectrophotometer detects the light intensity passing through a sample and compares the detected intensity to incident light intensity (light before passes through the sample).

The light transmission in materials is an essential element in physics. The general transmission principle which is given by the Beer-Lambert law, expresses the light intensity variation as a function of the thickness d of the traversed object by the light and the absorption coefficient α of the used material [130].

$$I = I_0 \exp(-\alpha d) \quad \text{(III.2)}$$

I: the light beam intensity exiting the sample. I_0: the light beam intensity entering the sample.
The light intensity I decreases exponentially with the increases of the thickness d of the absorbent medium. The transmission measurement principle is to measure the transmitted light in two samples, one of them is the reference sample and the other is the sample to be analyzed. The following formula gives the relationship between transmission and intensities.

$$T\% = \frac{I}{I_0}\ 100 \quad \text{(III.3)}$$

The optical transmission measurements within the framework of this study were obtained by a UV-Visible UV 3101 PC spectrophotometer type Shimadzu **(Figure III.15a)**. The light source, the sample holder with the reference, and the measurement system are the three main components of this UV-visible spectrophotometer **(Figure III.15b)**.

The light source contains two lamps, one to cover the ultraviolet range (190- 400nm) and the other for the visible and near infrared range from 350 to 900nm wavelength range. The light sources are switched automatically in conjunction with wavelength scanning.

To record the spectra, the UV-Vis spectrophotometer is connected to a microcomputer, which allows the data to be processed by software. The principle of measurement consists of two main steps: putting a reference substrate on one of the device's slits and leaving the other slit empty

which is crossed by the light, resulting a spectrum of the substrate. The obtained spectrum is saved as a base spectrum. The purpose of this step is to remove the effects of the substrate. The sample is then placed on the second slit, while the reference substrate stays on the first slit. The recorded spectra only reflect the transmission or absorption of thin films.

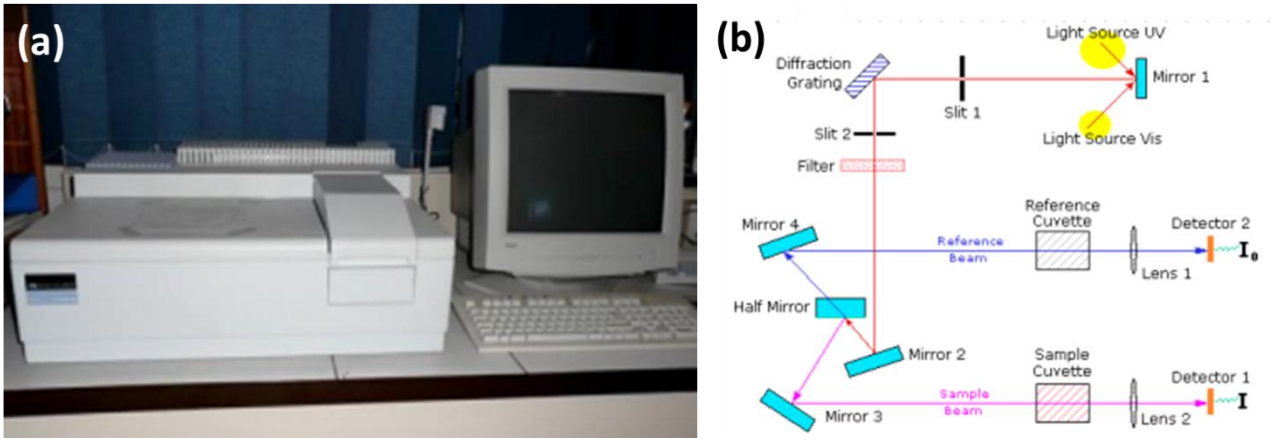

Figure III. 15. UV-Visible spectroscopy; (a) UV 3101 PC spectrophotometer type Shimadzu and (b) Schematic diagram of the UV spectrophotometer setup [131].

III.1.4.6 Photoluminescence spectroscopy PL

Luminescence is described as the emission of any visible, ultraviolet or infrared electromagnetic radiation, that is not strictly thermal in origin. It can be caused in a variety of ways, including by exposing the material to photons (photoluminescence), X-rays (X luminescence), accelerated electrons (cathodoluminescence), (α, β) particles (radioluminescence), or even an electric field (electroluminescence).

The phenomenon of luminescence is often divided into two phases: the excitation of the substance's electronic system, and its de-excitation during which light is emitted. Excitation and emission can be separated by intermediate phases, resulting in the distinction of two forms of light emission: fluorescence, which occurs almost immediately after excitation (t of the order of 10^{-8} s),

and phosphorescence, which occurs after a longer period of time (t can range from a fraction of a second to several days).

Photoluminescence (PL) is an optical technique for characterizing semiconductors and insulating materials. Its principle is based on the excitation of electrons in the sample to be studied by a monochromatic laser-type radiative source with a short wavelength. When the sample is exposed to radiation with a higher energy than the gap, the electrons in the valence band absorb it and cross the gap to the conduction band. Radiative or non-radiative transition mechanisms would then de-excite these electrons, allowing them to return to their original state. In the non-radiative transition mechanism, the electrons de-excite by giving up some of their energy to the crystal lattice in the form of acoustic vibrations called phonons. While in the radiative transition, electrons de-excite by emitting photons whose energy approaches that of the gap. The optical diagram of the device is shown in **(Figure III.16a)** [61].

The presence of impurities in the crystal lattice causes low energy electronic transitions to appear. The nature and proportion of these impurities can have a big impact on physical properties like electrical conductivity, which is why photoluminescence measurements are so significant.

A Perkin Elmer LS 50 luminescence spectrometer was used for photoluminescence measurements **(Figure III.16b)**. The light source is a 150 W xenon lamp. The lamp's light beam is focused on the entrance slit of an excitation monochromator, which determines the sample's excitation wavelength. The excitation wavelength used is 325 nm. A semi-transparent blade (Beam splitter) divides the outgoing beam, with a part reflecting to a control detector (reference photodiode) and the other part interacting with the sample. The luminescence radiation produced by the latter is directed towards the monochromator and the corresponding intensity value is measured by the photomultiplier. A computer system served for data collection and visualization.

Parameters such as the opening of the two monochromators' slits, the spectrum sweep speed, and the response time of the apparatus are all calibrated before the measurements are taken. The spectral resolution depends on the slit's width. It increases when the slit width decreases. However, for very narrow slits, a small amount of energy reaches the photomultiplier, and noise can affect spectral quality.

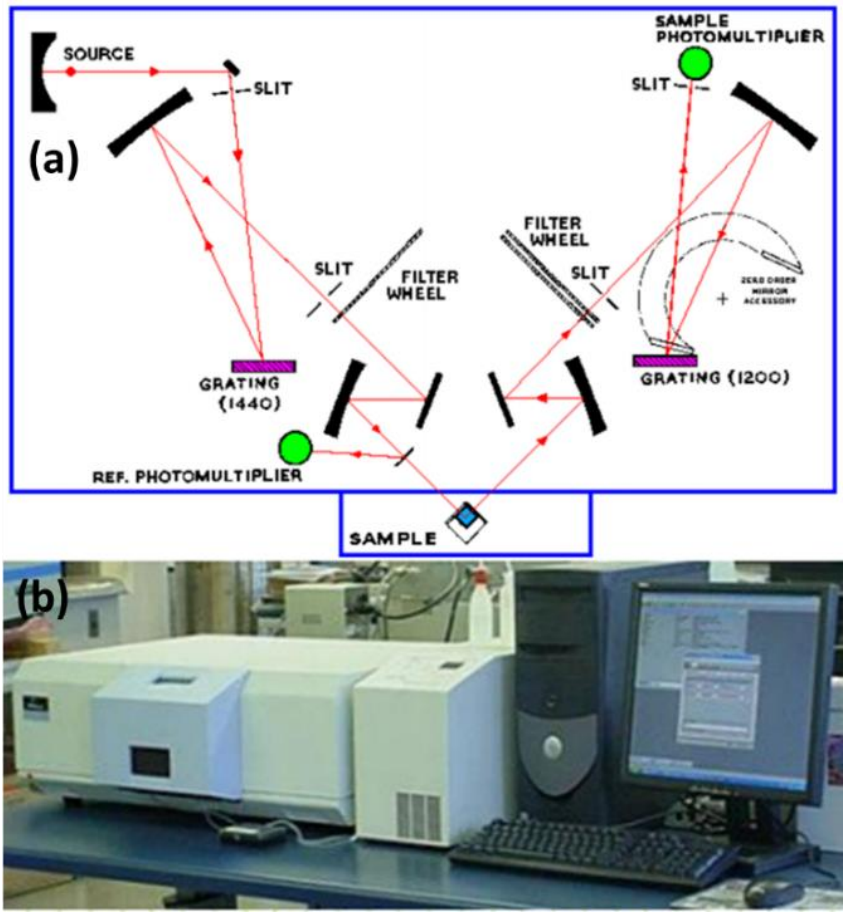

Figure III. 16. Photoluminescence spectroscopy PL; (a) Schematic diagram of the photoluminescence setup [58] (b) Perkin Elmer LS 50B luminescence spectrometer.

III.2 Calculation details

III.2.1 Introduction

Paul Dirac pointed out in 1929 that solving the Schrödinger equation for real systems needs to develop approximations that reduce the complexity of quantum calculations [1]. Hohenberg [2], Kohn [2], [3] and Sham [3] demonstrated, in the mid-sixties, that it was possible to write any Hamiltonian of a given system as a density functional. It took several years for such a method to be applicable because of the increase in digital capacities.

DFT is a highly successful method for describing the ground state properties of electronic systems such as metals, semiconductors, and insulators. It is widely used in the study of bulk materials, and it also effectively treats complex materials such as carbohydrates, proteins, and carbon nanotubes.

In the second part of this chapter, we will review the basis of DFT, as well as its implementation in the CASTEP code (Cambridge Sequential Total Energy Package) [132].

III.2.2 First-Principles Study

The foundation of first-principles method relied on quantum mechanics that describe the behavior of electrons and atomic nuclei in any situation [133]. The Schrodinger equation which was formulated by the Austrian physicist, Erwin Schrödinger, for non-relativistic quantum in a time-independent system, which explains all interactions between the nucleus and electrons inside a crystalline system. This time independent equation can be expressed as follows:

$$H\psi(\vec{r},\vec{R}) = E\psi(\vec{r},\vec{R}) \qquad \text{(III.4)}$$

Where: $\Psi(\vec{r},\overrightarrow{R})$ is the wavefunction, E is the total energy of the system and H is the Hamiltonian, which can be written for N nucleus and n electrons as:

$$H = \underbrace{\frac{-1}{2m}\sum_i^n \nabla_i^2}_{T_e} + \underbrace{\sum_i^n \sum_k^N \frac{Z_k e^2}{4\pi\varepsilon_0 r_{ik}}}_{V_{eN}} + \underbrace{\frac{1}{2}\sum_i^n \sum_{j\neq i}^n \frac{e^2}{4\pi\varepsilon_0 r_{ij}}}_{V_{ee}} - \underbrace{\frac{1}{2}\sum_k^N \frac{1}{M_k}\nabla_k^2}_{T_N} + \underbrace{\frac{1}{2}\sum_k^N \sum_l^N \frac{Z_k Z_l e^2}{4\pi\varepsilon_0 R_{kl}}}_{V_{NN}} \quad \text{(III.5)}$$

Where the nucleus (electron) has the position R_k (r_k), the mass M_k (m_k) and the charge $Z_k e$ (e) and R_{kl} (r_{ik}) is the distance between nuclei (electrons).

The Hamiltonian H can be written in another way as:

$$H = T_e + T_N + V_{ee} + V_{NN} + V_{eN} \quad \text{(III.6)}$$

Where:

T_e : is the electrons kinetic energy,

T_N : is the nucleus kinetic energy,

V_{ee} : is the potential energy of repulsion electron-electron,

V_{NN} : is the potential energy of repulsion nuclei-nucleus,

V_{eN} : is the potential energy of attraction electron-nucleus.

For systems containing more than one electron, the Schrodinger equation is too complex to be solved and would lead to uncontrollable computation. This is largely due to the nature of electrons that strongly interact each other, which leads to many-body problem [134-136]. Several approximations are then developed to solve the Schrodinger equation, of which the first useful one is the well-known Born–Oppenheimer approximation [137].

The idea in Born–Oppenheimer approximation is that atomic nuclei are more massive than electrons, and therefore their velocities are much lower. The nuclei can be considered as stationary, so we can eliminate the nucleus kinetic energy term T_N and considering the potential energy of

repulsion nuclei-nucleus term V_{NN} as constant. From this approximation, the resulting Hamiltonian is only constituted by contributions of electronic type:

$$H_e = T_e + V_{ee} + V_{eN} \quad \text{(III.7)}$$

Where: H_e is the electronic Hamiltonian.

Thanks to this approximation, the problem of interacting electrons, ions, and nuclei vanishes, allowing the Schrodinger equation to be applied in a complex system and became very simple compared to the original.

The wave function in Schrödinger equation becomes depending only on electrons. Thus, to solving the equation, the problem is reduced to determining the values and eigenfunctions of these electrons.

$$H_e.\psi = E_e.\psi \quad \text{(III.8)}$$

This obtained equation represents a problem with *n* bodies, where a large number of electrons interaction between themselves makes the resolution difficult. A rigorous resolution cannot be obtained analytically except in very simple cases such as that of the hydrogen atom. To do this in the most general case, it is necessary to introduce other approximations.

Hartree approach is one of these approximations. The problem of N interacting electrons was reduced to a single electron system. The interaction of each electron in the atom with all other electrons is replaced by the interaction with an average field created by the nuclei, and all other electrons and electron movements are assumed to be uncorrelated.

So, the Hamiltonian could be written as a sum of the Hamiltonians, each describing the behavior of a single electron:

$$H = \sum_i H_i \quad \text{(III.9)}$$

Where:

$$H_i = -\frac{h^2}{2m}\nabla_i^2 + U_i(r_i) + V_i(r_i) \quad \text{(III.10)}$$

Such as:

$U_i = -\sum_k \frac{Z_k e^2}{4\pi\varepsilon_0 |r_i - R_k^0|}$: is the potential energy of the electron (i) in the field of all nuclei ($V_N(r_i)$).

$V_i = \frac{1}{2}\sum_j \frac{e^2}{4\pi\varepsilon_0 |r_i - r_j|}$: is the Hartree effective field.

The wave function of the electronic system is a product of the wave functions of the electrons, and its energy is equal to the sum of all electron energies.

$$\psi_e(\vec{r}_1, \vec{r}_2, \vec{r}_3, \ldots, \vec{r}_n) = \psi_1(\vec{r}_1)\psi_2(\vec{r}_2)\psi_3(\vec{r}_3)\ldots\psi_n(\vec{r}_n) \quad \text{(III.11)}$$

And

$$E = E_1 + E_2 + E_3 + \ldots + E_n \quad \text{(III.12)}$$

With:

$$H_i\psi_i = E_i\psi_i \quad \text{(III.13)}$$

The Hartree field allows the multiple equation to be reduced to a single electron equation system.

$$\left[-\frac{1}{2m}\nabla_i^2 + U_i(r_i) + V_i(r_i)\right]\psi_i = E_i\psi_i \quad \text{(III.14)}$$

Fock demonstrated that the Hartree wave function violates the Pauli exclusion principle because it is not antisymmetric to any two-particle exchange. To correct this default, he proposed writing the wave function as a Slater determinant in order to satisfy the Pauli principle[138]:

$$\psi_e = \psi(\vec{r}_1, \vec{r}_2, \dots \vec{r}_n) = \frac{1}{\sqrt{N!}} \begin{vmatrix} \psi_1(\vec{r}_1)\psi_1(\vec{r}_2)\dots\psi_1(\vec{r}_n) \\ \psi_2(\vec{r}_1)\psi_2(\vec{r}_2)\dots\psi_2(\vec{r}_n) \\ . \\ \psi_n(\vec{r}_1)\psi_n(\vec{r}_2)\dots\psi_n(\vec{r}_2) \end{vmatrix} \quad \text{(III.15)}$$

With $\frac{1}{\sqrt{N!}}$ is the normalization constant.

The Hartree-Fock method works well for atoms and molecules, but it is less precise for solid.

III.2.3 Density Functional Theory

The basic idea behind the density functional is that the energy of a system can be expressed as a function of the electron density $\rho_0(\boldsymbol{r})$, which minimizes the system energy. Since the earliest contribution of Thomas and Fermi in 1920, where they demonstrated that the energy of an electron gas is a function of its electron density, the use of electronic density as a fundamental variable to describe the properties of the system has been developed [139].

In 1964, Hohenberg and Kohn have developed a theorem that defined the electron density as a unique function for ground state energy of a system with N-electron [140]. Later, a set of independent-particle equation has been established by Kohn and Sham [141]. They have introduced a Schrodinger-like equation with a modified effective potential that is much easier to calculate than the original Schrodinger equation [133].

The electron density in an electronic system is defined as the number of electrons per unit volume in a given state. It is expressed as a function of the square of the wave function $|\Psi|^2$

(probability of finding an electron in the element of volume $d\boldsymbol{r}_1$, whatever the position and the spin of the other *N*-1 electrons). It is given for an electron as:

$$\rho(r) = \rho(r_1) = N \int \ldots \int |\psi(x_1, x_2, \ldots, x_N)|^2 \, dx_1 dx_2 \ldots dx_N \quad \text{(III.16)}$$

The electron density *ρ(r)* is a positive function that depends only on the three spatial coordinates (x, y, z). The limit at infinity of the electron density *ρ(r)* function is zero ($\lim_{r\to\infty} \rho(r) = 0$), and is equal to *N*, the total number of electrons, when integrated over all space ($\int \rho(r)\, dr_1 = N$). Unlike the wave function, electron density is an observable that can be measured by X-ray neutron diffraction [142, 143].

III.2.3.1 Thomas –Fermi Model

The Thomas and Fermi model is based on describing the energy system as a simple function of density, which is the main origin of the DFT [139]. Using the kinetic energy expression and taking into account the electron-nuclei and electron-electron contributions, the Thomas-Fermi total energy is given by;

$$E = T_{TF} + \int V(r)\rho(r)dr + \frac{1}{2}\int \frac{\rho(r)\rho(r')}{|r-r'|} dr dr' \quad \text{(III.17)}$$

Thomas-Fermi total energy =Kinetic Energy + External Potential (due to nuclei) + Electron-Electron Interaction

Where T_{TF}**:** is the kinetic energy given as**:**

$$T_{TF} = C_F \int \rho(r)^{5/3} \, dr \quad \text{(III.18)}$$

With

$$C_F = {3(3\pi^2)^{2/3}}/{10} \quad \text{(III.19)}$$

This model fails to explain the exchange and correlation effects and does not give a binding energy for molecules.

III.2.3.2 Hohenberg–Kohn theorems

There are two theorems formulated by Hohenberg and Kohn which served as the basis for modern DFT [133]. The first theorem stated that in a system with *n* interacting electrons the total energy of an electron gas in the presence of an external potential is a single functional of the electron density *ρ(r)*. It could be expressed as follow [140]:

$$E = E[\rho(r)] \quad \text{(III.20)}$$

As a result, the total energy functional of the ground state, is given by:

$$E_0 = T[\rho_0] + E_{ne}[\rho_0] + E_{ee}[\rho_0] \quad \text{(III.21)}$$

The second Hohenberg–Kohn theorem allocates a minimum principle for the density. It stated that the exact energy of the ground state is the minimum value of this functional ${\delta E}/{\delta\rho}\Big|_{\rho_0} = 0$, and that the exact density of the ground state is the density which leads to this energy. The other properties of the ground state are also functional of this density.

$$E_0 = E(\rho_0) = min\, E\,(\rho) \quad \text{(III.22)}$$

ρ_0 : is the density of the ground state.

The theorems give no information about how to construct the functional. Kohn and Sham then proposed a simple method for solving the many-body problem by replacing it with an independent electron problem.

III.2.3.3 Kohn–Sham method

The Kohn–Sham method introduced a fictitious supporting system to resemble the real many-electron system. This approach gives a set of independent-particle equations that are numerically solvable [141]. The total energy is given by:

$$E_{Vext}[\rho] = T_0[\rho] + V_H[\rho] + V_{XC}[\rho] + V_{ext}[\rho] \quad \text{(III.23)}$$

Where: T_0 is the kinetic energy of the system without interaction. V_H stands for Hartree term or the Coulomb interaction between electrons. V_{ext} represents the Coulomb interaction of electrons with nuclei and that of nuclei with each other. V_{XC} is the term including the effects of exchange and correlation that can be given by the derived functional energy:

$$V_{XC} = \frac{\partial E_{XC}[\rho(r)]}{\partial \rho(r)} \quad \text{(III.24)}$$

Where E_{XC} is known as the exchange–correlation energy that contains the correlation energy, exchange energy, Coulombic correlation energy, and self-interaction correction. So far, no exact expression for this exchange and correlation (XC) potential is known. An approximation is thus embodied in the formalism to ensure the accuracy of DFT calculation [144-146].

III.2.4 Exchange–Correlation Functional

There are several approximations that have been developed, namely, the LDA, GGA, meta-GGA, and hybrid functional. Each of these approximations conveys different definitions and approaches and is thus suitable for specific materials. Among them, the LDA and GGA are the ones widely used in DFT calculation of ZnO system [133].

III.2.4.1 Local Density Approximation

The idea of the Local Density Approximation (LDA), which is the basis of all modern exchange-correlation functionals, is to consider V_{XC} as a local quantity defined at a point of the space r of material with a slow varying in charge density around this point [147]. The LDA formalism is presented as follows:

$$E_{XC}^{LDA} = \int \rho(r)\varepsilon_{XC}[\rho(r)]dr \quad \text{(III.25)}$$

$\varepsilon_{xc}[\rho(r)]$ can be considered as the sum of an exchange and correlation contribution:

$$\varepsilon_{xc}[\rho(r)] = \varepsilon_X[\rho(r)] + \varepsilon_C[\rho(r)] \quad \text{(III.26)}$$

Where ε_C represents the correlation energy and ε_X is the exchange energy.

Generally, the functional $\varepsilon_{xc}$is determined by different parameterization procedures such as those of Perdew and Wang, Kohn and Sham, Ceperly and Alder, Wigner, Perdew and Zunger and Hedin and Lundqvist [141, 148-152].

The LDA, is very successful approximations for many systems with quite uniform electron density, such as metals [153]. Also, LDA has been found to be very efficient in the extended system, such as calculation in solids and large molecules, and suitable for calculations of free atoms, molecules and systems with strong bonds [154]. However, the bandgaps calculations of semiconductors and insulators by the use of LDA revealed a strong underestimation, which is remedied with the use of Hedin's GW method [149], It also failed to reproduce the energy gap of systems exhibiting strong correlations between their *d* (or *f*) bands, which is overcome by the introduction of the Hubbard correction LDA + U [155, 156].

III.2.4.2 Generalized Gradient Approximation

The extension to improve the accuracy of (LDA) is provided by second approximation known as Generalized Gradient Approximation (GGA) [133]. This approximation is based on the suggestion that the exchange-correlation potential not depends only on the charge density, ρ as in LDA, at a given point ***r***, but also on its gradient, $\nabla\rho$, as given by the following equation:

$$E_{xc}^{GGA}[\rho, \nabla\rho] = \int f[\rho(r), \nabla\rho(r)]\, dr \qquad \text{(III.27)}$$

Where f [ρ (r), $\nabla\rho(r)$] is the exchange and correlation function dependent on the electron density and its gradient.

In addition, there are several corrected functionals are developed in GGA formalism to include the contribution of exchange and correlation part. These functionals are PBE, Perdew, Burke, and Ernzerhof for solid (PBESol) [157], and Perdew–Wang 1991 (PW91) [158].

III.2.5 Hubbard-U Scheme

To remedy the shortcoming calculation error of LDA and GGA in some systems such as ZnO system, many methods has been discussed and proposed. Among them, to increase the band gap, there is a method known as scissor operator incorporated in computer code [132], self-interaction correction (SIC) [153], and Hubbard-U correction [159].

Hubbard-U method is widely used as its calculation procedure is simple, the calculated results are reliable, and it is practically economical. The basis of this method introduced an orbital-dependent term known as on-site Coulomb repulsion energy, U into the XC term of LDA and GGA [155]. They are now referred to as LDA+U or GGA+U and expressed as follows:

$$E_{LDA+U}[\rho(r)] = E_{LDA}[\rho(r)] + E_U[\rho(r)] - E_{dc} \qquad \text{(III.28)}$$

Where, E_{LDA} is the energy from conventional LDA functional, E_U is the Hubbard type energy, and E_{dc} is the double-counting correction energy. Depending on the computer program, the Coulomb energy and the exchange energy are combined into a single parameter known as on-site Coulomb repulsion U as implemented in Cambridge Serial Total Energy Package (CASTEP) computer code [20, 40].

III.2.6 CASTEP code

CASTEP code (CAmbridge Serial Total Energy Package) which developed by Clark et al. [132], is a part of set of digital simulation software called Material Studio (MS) marketed by Accelrys©. This code aiming to perform electronic structure and any physical properties calculations of crystals and surfaces in materials, using density functional theory with plane waves basis set.

Two SCF (Self-consistent field) algorithms are implemented in the CASTEP code to determine the electronic ground state of the studied systems: Density Mixing (DM) and EDFT [160, 161]. The difficulty of convergence for a given system influences the choosing of one of these algorithms. In the DM algorithm, CASTEP supports four mixing methods: linear mixing, Kerker mixing, Broyden mixing and Pulay mixing [162-164]. The Pulay or Broyden method is recommended. The linear method is generally not suitable for large systems. The new electron density (after minimization) ρ_{out} is mixed with the initial density ρ_{in} and repeating the process until the convergence is reached.

In the CASTEP package, geometry optimization is performed using algorithms such as BFGS (Broyden, Fletcher, Goldfarb and Shannon) [161], Damped MD (Damped molecular dynamics) [165] and TPSD (Two-Point Steepest Descent) [166]. By using the BFGS algorithm, cells can be optimized in the presence of external stress.

The optimization of such a system is based on the minimization of forces, obtained by the Hellmann-Feynman theorem [167-169], which apply to each of the atoms constituting the structure.

III.2.7 Calculation setting

The 2 × 2 × 4 ZnO supercell containing 64 atoms is constructed from the optimized bulk wurtzite ZnO unit cell. Then, two Mn atoms substitutionally replaced two nearest Zn sites to achieve the concentration x = 6.25%, and antiferromagnetic phase was considered. For the practical, x = 6.25% of Mn concentration was used as it is the nearest value to 7% (concentration of Mn in the experimental part), which offers a less time-consuming DFT calculation. This was confirmed in the previous works for x = 12.5% [64, 170], where Mn atoms form cluster around the O atom. The obtained supercells of pure and Mn-doped ZnO materials ($Zn_{1-x}Mn_xO$; x = 6.25%) are optimized using DFT as implemented in CASTEP code [171]. The generalized gradient approximation (GGA) in the scheme of Perdew–Burke–Ernzerhof (PBE) was used to treat the exchange-correlation function [157].

Valence electron configurations for constructing pseudopotential were as follows: O: $2s^2\ 2p^4$, Zn: $3d^{10}\ 4s^2$, and Mn: $3d^5\ 4s^2$. The plane-wave ultrasoft pseudopotential method was used to reduce the cut-off kinetic energy [172], which was fixed at 400 eV. The 3 × 3 × 1 k-point grid was employed for the Brillouin-zone integration. Geometric optimization was performed using the convergence thresholds of 5×10^{-6} eV/atom for total energy, 0.05 eV/Å for maximum force, 0.05 GPa for pressure, and 1.0×10^{-3} Å for maximum displacement. The total tolerance of self-consistent calculations was 5×10^{-6} eV/atom. Based on the semi-empirical GGA+U approach to improve the bandgap energy [133], the following effective Hubbard U values were used: 5.5 eV for *Zn 3d* states, 10 eV for *Mn 3d* states, and 8 eV for *O 2p* states.

IV. Results and discussion

IV.1 Introduction

In this study, we have successfully synthesized pure ZnO, 4% and 7% Mn- doped ZnO thin films on glass substrates using the sol gel spin coating technique, in order to investigate the influence of thickness on the different structural, electronic and optical properties. Also, DFT+U calculation of pure and Mn- doped ZnO materials was done. The obtained thin films were characterized by different techniques: Diffraction X-rays (XRD), Atomic Force Microscopy (AFM) and Field Emission Scanning Electron Microscope (FESEM) for structural and morphological properties, UV-visible and photoluminescence for electronic and optical properties. In this chapter, we present the different experimental and DFT calculation results. All of these results are presented in figures or tables, discussed and compared.

IV.2 Experimental results

IV.2.1 Thickness measurement

The thicknesses of both pure ZnO and 7% Mn- doped ZnO thin films were measured using Stylus Profilometer (model: D 500). It is observed that the film thickness was increased with coating number, especially for Mn-doped thin films **(Figure IV.1)**.

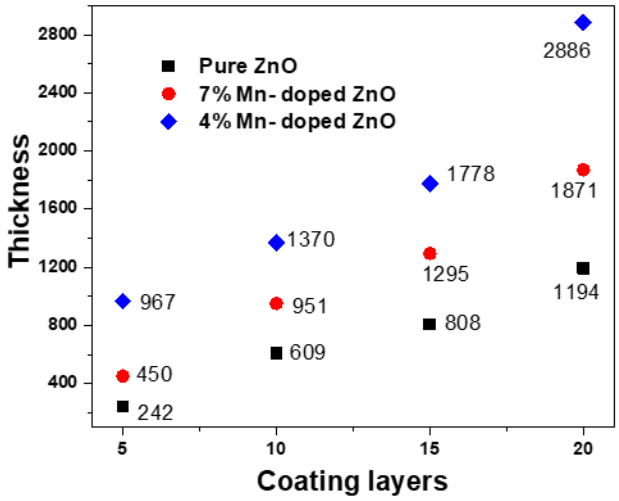

Figure IV. 1. Thickness variation in function of coating layers.

The average thickness of one deposited layer was found to be 50 nm for pure ZnO, 150 nm for 4% Mn- doped ZnO and 90 nm for 7% Mn-doped ZnO. These results were confirmed by FESEM cross sectional images **(Figure IV.2).**

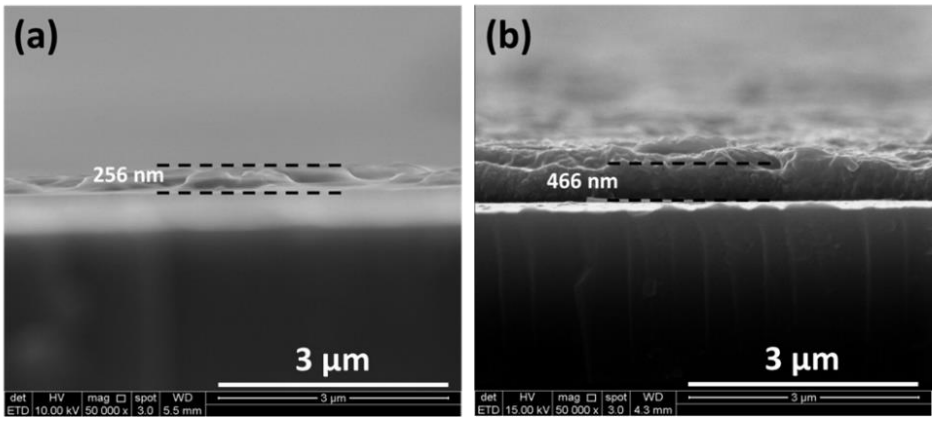

Figure IV. 2. FESEM cross sectional images of the samples of 5 layers; (a) pure ZnO thin films, (b) 7% Mn-doped ZnO thin films.

IV.2.2 Structural properties

IV.2.2.1 Pure ZnO

The structural properties of pure ZnO thin films for various thicknesses were studied by XRD **(Figure IV.3)**. Three main peaks were observed: (100), (002), and (101). These peaks indicate that the films are polycrystalline with a preferential orientation along the c-axis. It is observed that the (002) diffraction peak is stronger than the other peaks, indicating that the common direction along the c-axis is the preferential growth direction, and the surface free energy of (002) planes is the most stable compared to others [173].

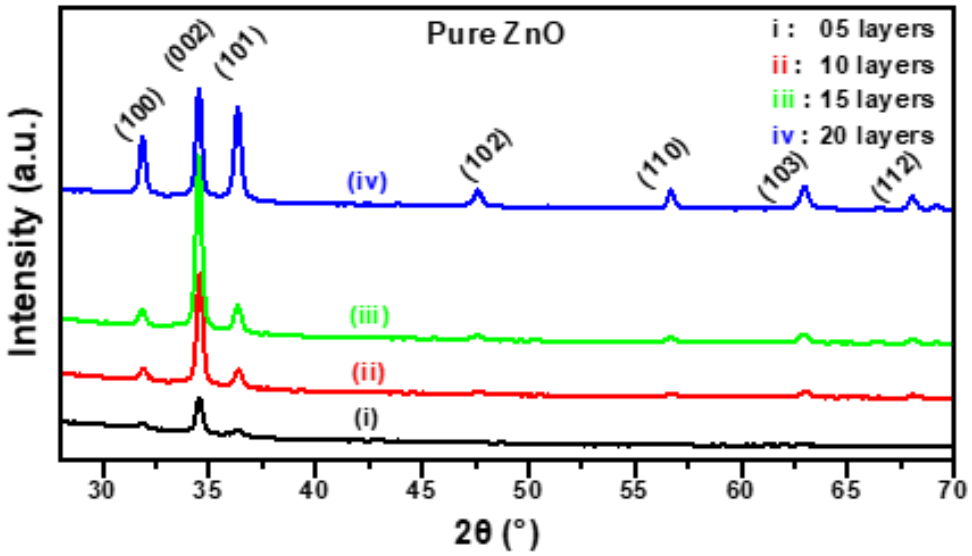

Figure IV. 3. XRD patterns of pure ZnO thin films for various deposited layers.

The lattice constants ($a = b$ and c) of the pure ZnO thin films with different deposited layers are calculated using the following formulas:

$$sin^2\theta = \frac{\lambda^2}{4\left[{}^4/_3{}^{(h^2+hk+k^2)}/_{a^2}+{}^{l^2}/_{c^2}\right]} \qquad \text{(IV.1)}$$

where θ is the diffraction angle, λ is the incident radiation wavelength Cu-Kα (λ = 1.5406 Å), and h, k, and l are the Miller indices.

From this formula, we can determine the two parameters a and c by taking the positions of (100) and (002) peaks, we find [174] :

$$a = {}^{\lambda}/_{\sqrt{3}\sin\theta_{100}} \qquad \text{(IV.2)}$$

$$c = {}^{\lambda}/_{\sin\theta_{002}} \qquad \text{(IV.3)}$$

The c-axis values insignificantly increase with thickness **(Table IV.1)**. This evolution is inversely proportional to the slight shift toward the lower angles of the (002) peak 2θ position with the increase of the coating number caused by relaxation of the residual strain [26]. The relative deviation with maximum up to 0.42% well agrees with those reported in the literature [16, 32, 53, 175, 176].

The average crystallite size of pure films with various thicknesses was calculated using the full-width-at-half-maximum (FWHM) of the most intense peak (002) by Scherrer's formula:

$$D = {K\lambda}/{\beta \cos \theta_{hkl}} \qquad \text{(IV.4)}$$

Where D is the crystallite size, λ is the x-ray wavelength (λ = 0.14506 nm), β is FWHM (full width at half maximum intensity), θ is the Bragg angle and the coefficient K =0.9 is the shape factor.

It is found that the crystallite sizes strongly depend on the number of the deposited layers and increase when the number of the deposited layers increases **(Table IV.1)**. Similar behavior of the crystallite sizes was observed by others for pure ZnO thin films synthesized by sol–gel [21, 91].

The strain (ε_{zz}) values are calculated using the following equation [176]:

$$\varepsilon_{zz} = [(c - c_0)/c_0].100\% \qquad \text{(IV.5)}$$

where c is the lattice parameter of the strained films estimated from the X-ray diffraction data and c_0 = 5.207 Å is the unstrained lattice parameter of bulk ZnO (JCPDS 36-1451: bulk value). The

compressive strain decreases with the increase of the film thickness for pure thin films, where the film is relaxed and becomes thicker **(Table IV.1)**.

Table IV. 1. Structural parameters of pure ZnO thin films for various deposited layers extracted from the (002) main peak.

Samples	Coating number	Thickness (nm)	2θ (°)	a (Å)	c (Å)	FWHM (°)	Peak intensity	Crystallite size (nm)	Strain, ε_z (%)
Pure ZnO	05	242	34.52	3.245	5.194	0.224	1073	37.15	-0.233
	10	609	34.54	3.241	5.192	0.218	2598	38.00	-0.284
	15	808	34.50	3.244	5.198	0.209	3870	39.63	-0.169
	20	1194	34.49	3.242	5.198	0.199	2622	41.74	-0.166

The texture coefficient $TC_{(hkl)}$ for all peaks observed in XRD patterns of pure ZnO thin films **(Figure IV.4)** was calculated for various thicknesses using the following relation [175]:

$$TC_{(hkl)} = \frac{I_{(hkl)}}{I_{0_{(hkl)}}} \Big/ \frac{1}{N} \sum_1^N \left(\frac{I_{(hkl)}}{I_{0_{(hkl)}}} \right) \quad \text{(IV.6)}$$

Where $I_0(hkl)$ is the intensity of the standard powder diffraction peak, N is the number of diffraction peaks and $I(hkl)$ is the measured relative intensity of a diffraction peak.

The highest $TC_{(hkl)}$ value was in the (002) plane indicating that all films present a preferred growth orientation along c-axis, i.e., (002) plane, whatever the number of the deposited layers is. The degree of c-axis orientation depends on the number of the deposited layers where the higher value of texture coefficient reveals a better crystallinity of thin film. It can be seen that the intensity of (002) diffraction peak is increased as the film is grown up to 15 layers, and then decreased. Dislike (002) peak, the intensity of (100) and (101) peaks were found to be decreased first up to

15 layers and then increased. This indicate that the crystal growth tends to be lateral at high thickness.

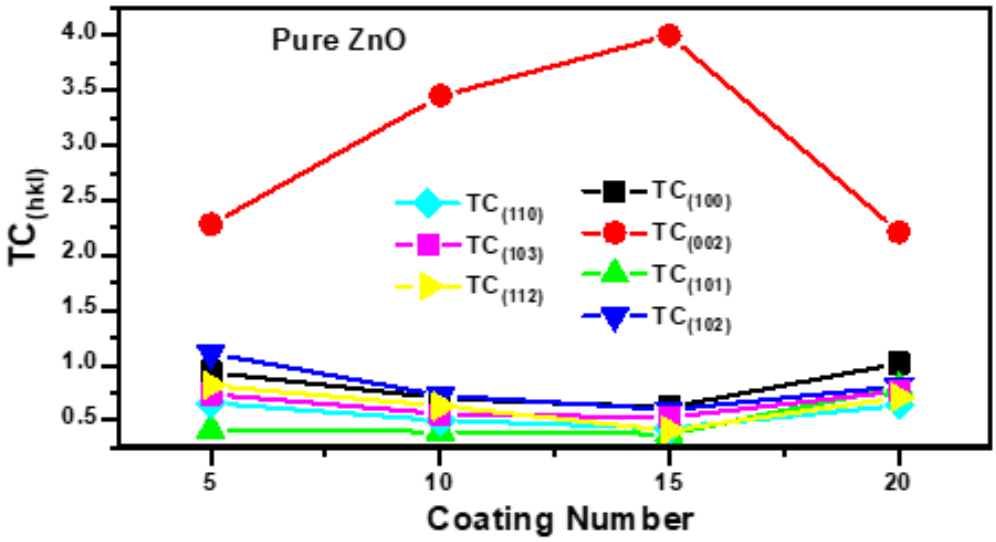

Figure IV. 4. Texture coefficient ($TC_{(hkl)}$) values of pure ZnO thin films for various deposited layers.

IV.2.2.2 Mn-doped ZnO thin films

The structural properties of 4% **(Figure IV.5a)** and 7% **(Figure IV.5b)** Mn-doped ZnO thin films were studied by XRD. The three main peaks (100), (002), and (101) in the XRD patterns were observed for all films. These peaks indicated that the Mn-doped ZnO thin films are polycrystalline with a preferential orientation along the c-axis. Also, any secondary phase was detected in both 4% and 7% Mn-doped ZnO films, such as $ZnMnO_3$ or Mn_3O_4 [25, 177]. It also showed that there were no significant changes in the wurtzite structure after the substitutional incorporation of Mn^{+2} into ZnO host [10].

However, the (002) diffraction peak was observed stronger compared to the other peaks indicating that the common direction along the c-axis was the preferential growth direction. This indicated that the surface free energy of (002) planes was the most stable compared to others [173].

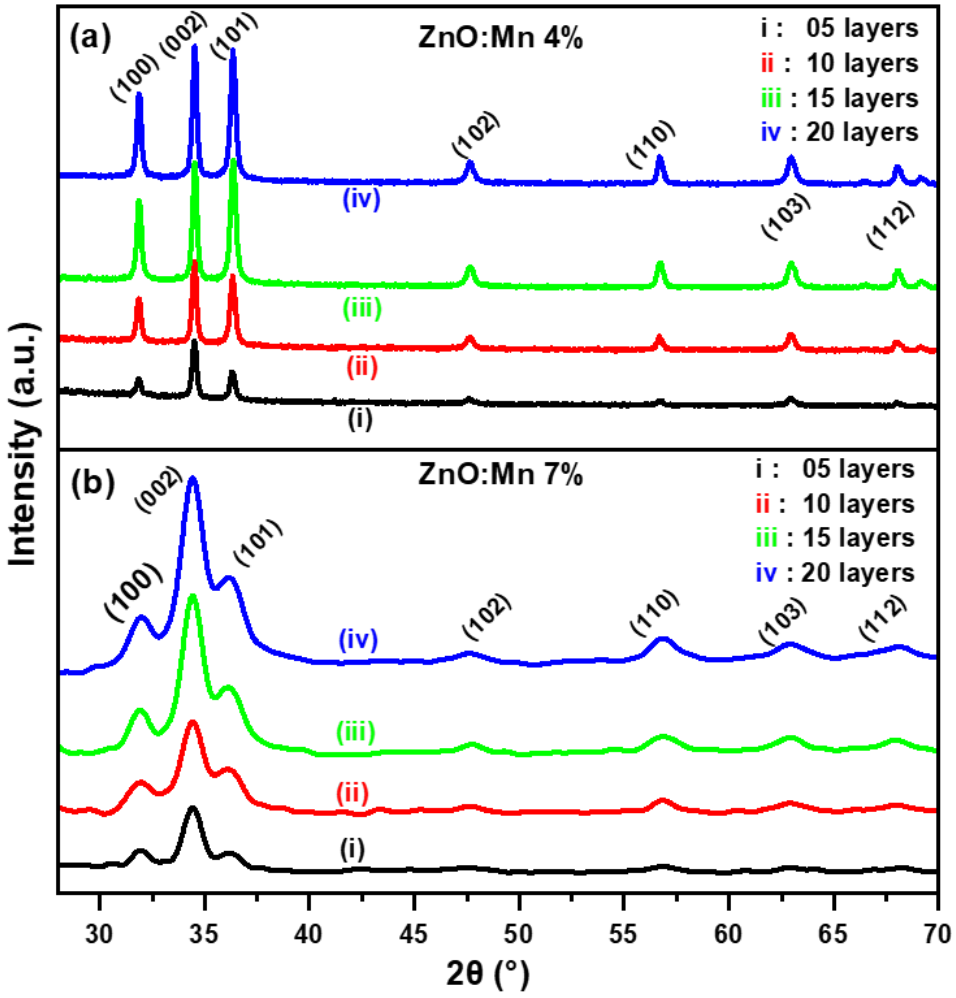

Figure IV. 5. XRD patterns of (a) 4% and (b) 7% Mn-doped ZnO thin films for various deposited layers.

The lattice constants $a = b$ and c of the thin films with different deposited layers are also calculated using the structure factor for wurtzite structure **(relations IV 1,2)**. The c-axis constant of 4% Mn-doped ZnO thin films decreased slightly from 5.198 Å (5 layers) to 5.195 Å (20 layers) with the increase of coating number **(Table IV.2)**, and all obtained values were less than the bulk value 5.207 Å (JCPDS 36-1451). This variation showed inversely proportional to the slight shift toward the higher angles of the (002) peak 2θ position with the increase of the coating number.

The c-axis constant of 7% Mn-doped ZnO thin films decreased slightly from 5.218 Å (5 layers) to 5.209 Å (20 layers) with the increase of coating number and approaches the bulk value 5.207 Å (JCPDS 36-1451) **(Table IV.2)** [11]. This evolution is inversely proportional to the slight shift toward the lower angles of the (002) peak 2θ position with the increase of the coating number caused by relaxation of the residual strain [26]. The c-axis values with maximum relative deviation up to 0.52% agree well with those reported in the literature [16, 27, 32, 53, 175, 176].

The average crystallite size was also calculated by Scherrer's formula **(relation IV. 3) (Table IV.2)**. It can be seen that the crystallite size values of 4% Mn- doped ZnO increased slightly from 39.23 nm (5 layers) to 40.36 nm (20 layers) with the increase of film thickness. However, the crystallite size values of 7% Mn- doped ZnO increased slightly from 10.09 nm (5 layers) to 10.14 Å (20 layers) with the increase of film thickness. Similar behavior was observed by others for Mn-doped ZnO films synthesized by RF- sputtering in nitrogen gas [27], and sol gel dip coating method [25].

The strain (ε_{ZZ}) values are also calculated using the **(equation IV.5) (Table IV.2)**. The compressive strain decreases with the increase of the film thickness for 4% Mn-doped ZnO thin films, where the film is relaxed and becomes thicker. However, 7% Mn-doped ZnO thin films present a decreasing tensile strain.

Table IV. 2. Structural parameters of 7% Mn-doped ZnO thin films for various deposited layers extracted from the (002) main peak.

Samples	Coating number	Thickness (nm)	2θ (°)	a (Å)	c (Å)	FWHM (°)	Peak intensity	Crystallite size (nm)	Strain, ε_z (%)
4% Mn:ZnO	05	967	34.498	3.243	5.198	0.212	1945	39.23	-0.173
	10	1370	34.500	3.243	5.197	0.211	2598	39.44	-0.192
	15	1778	34.519	3.241	5.195	0.209	3569	39.77	-0.230
	20	2886	34.514	3.241	5.195	0.206	3912	40.36	-0.230
7% Mn:ZnO	05	450	34.36	3.243	5.218	0.824	614.14	10.09	0.219
	10	951	34.38	3.243	5.215	0.815	695.14	10.20	0.165
	15	1295	34.40	3.241	5.212	0.807	907.30	10.30	0.097
	20	1871	34.42	3.242	5.209	0.820	992.41	10.14	0.055

The texture coefficient $TC_{(hkl)}$ for all peaks observed in XRD patterns of 4% **(Figure IV.6a)** and 7% **(Figure IV.6b)** Mn-doped ZnO films were calculated by the **equation (IV. 5)** for various thicknesses. The highest $TC_{(hkl)}$ value obtained was (002) plane for all Mn-doped ZnO thin films. This indicated that all films presented a preferred growth orientation along c-axis, which is (002) plane regardless of the number of deposited layers. The intensity of (002) diffraction peak increased as the film thickness increased from 5 layers to 20 layers for both 4% and 7% Mn-doped ZnO thin films. Also, the intensity of (100) and (101) peaks were found to be increased with coating numbers. However, the $TC_{(hkl)}$ values for the main peak (002) of 4% Mn-doped ZnO thin films decreased from 2.49 nm (5 layers) to 2.11 nm (20 layers) with the number of deposited layers, while the $TC_{(hkl)}$ of 7% Mn-doped ZnO increased from 1.57 nm (5 layers) to 2.07 nm (20 layers).

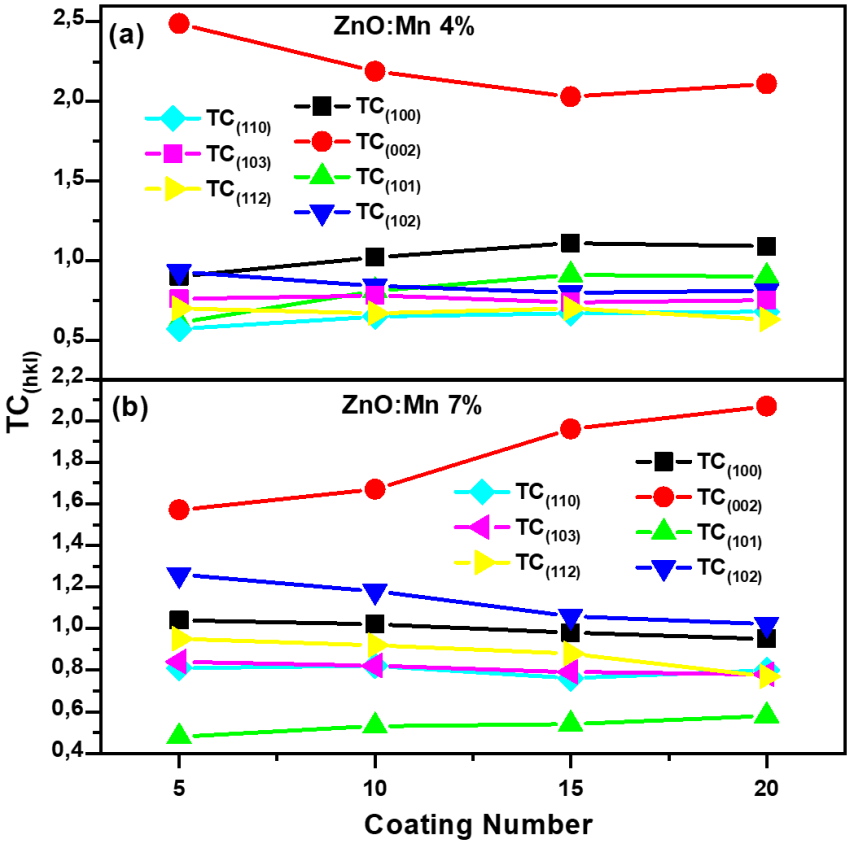

Figure IV. 6. Texture coefficient ($TC_{(hkl)}$) values of (a) 4% and (b) 7% Mn-doped ZnO thin films for various deposited layers.

IV.2.2.3 Comparison

- The main diffraction peaks become broader for 7% Mn-doped ZnO thin films compared to pure ZnO because of the increase of strain due to Mn^{+2} incorporation in the Zn lattice site [10, 178]. The obtained results are confirmed by the large values of the strain of Mn-doped ZnO thin films compared to those of the undoped ones for all deposited layers.
- The c-axis constant shifts toward higher values when going from the pure ZnO thin films to the doped ones **(Table IV.1 and IV.2)**. This can be attributed to the fact that the ionic radius of Mn^{2+} (0.80 Å) is larger than that of Zn^{2+} (0.74 Å).

- It can be seen that the values of crystallite size of pure ZnO films are higher than those of Mn-doped films for all deposited layers. This may be due to the strain induced in the doped ZnO caused by the replacement of the host (Zn^{2+}) by the dopant (Mn^{2+}) cations that prevents the grain growth [10, 13].
- The highest $TC_{(hkl)}$ value was in the (002) plane for both pure and Mn-doped ZnO thin films, indicating that all films present a preferred growth orientation along c-axis, i.e., (002) plane, whatever the number of the deposited layers is.
- The intensity of (002) diffraction peak is increased as the film is grown up to 15 layers for both pure and Mn-doped ZnO thin films. Above 15 layers, unlike the pure ZnO thin films, where the (002) peak was decreased, the (002) intensity peak continued to increase for Mn-doped ZnO thin films.

IV.2.3 Morphological properties

IV.2.3.1 AFM analysis

IV.2.3.1.1 Pure ZnO

AFM analysis was used to investigate the morphological properties of pure ZnO thin films with various thicknesses **(Figure IV.7)**. The 3D AFM images were scanned over an area of 1.0 × 1.0 μm^2. The grain size and surface roughness of samples were extracted from the AFM images **(Table IV.3)** using WsXM software [126]. The samples present a uniform growth, the grains are round shape in plane for all samples, and their size generally increases by increasing the coating number. This means that the grain growth is mainly vertical and then tends to become lateral by increasing the film thickness, which agrees with our XRD analysis. The ZnO thin films involve columnar grains that grow along the (002) direction perpendicular to the substrate surface. The root mean square (RMS) of the films was found to be increased with thickness.

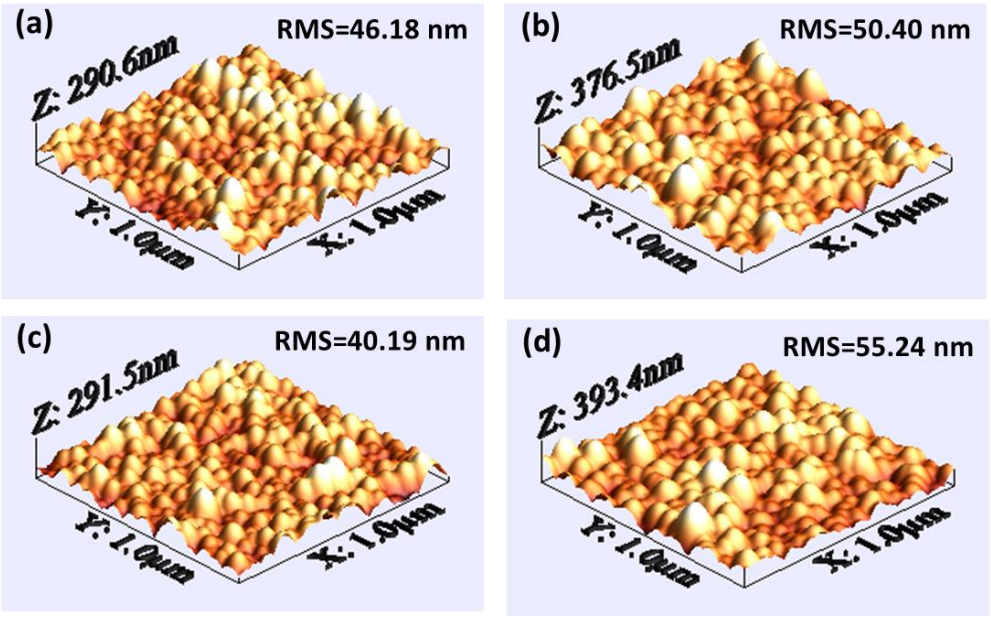

Figure IV. 7. 3D AFM images of pure ZnO thin films; (a) 5 layers, (b) 10 layers, (c) 15 layers, (d) 20 layers.

IV.2.3.1.2 Mn-doped ZnO

The morphological properties of 4% **(Figure IV.8a)** and 7% **(Figure IV.8b)** Mn-doped ZnO thin films with various thicknesses were investigated by AFM analysis. The 3D AFM images scanned over an area of 1.0 X 1.0 μm^2. The grain size and the surface roughness were also extracted from the AFM images **(Table IV.3)** using WsXM software [126].

The AFM images showed clearly that the samples presented a uniformly round shaped grains in a plane for all 4% and 7% Mn- doped ZnO samples. The size of their grains generally increased by increasing the coating number. This result means that the growth of grains is mainly vertical along (002) direction perpendicular to the substrate surface. This result is in agreement with our XRD analysis. The root mean square (RMS) of the films found to slightly increased with the thickness.

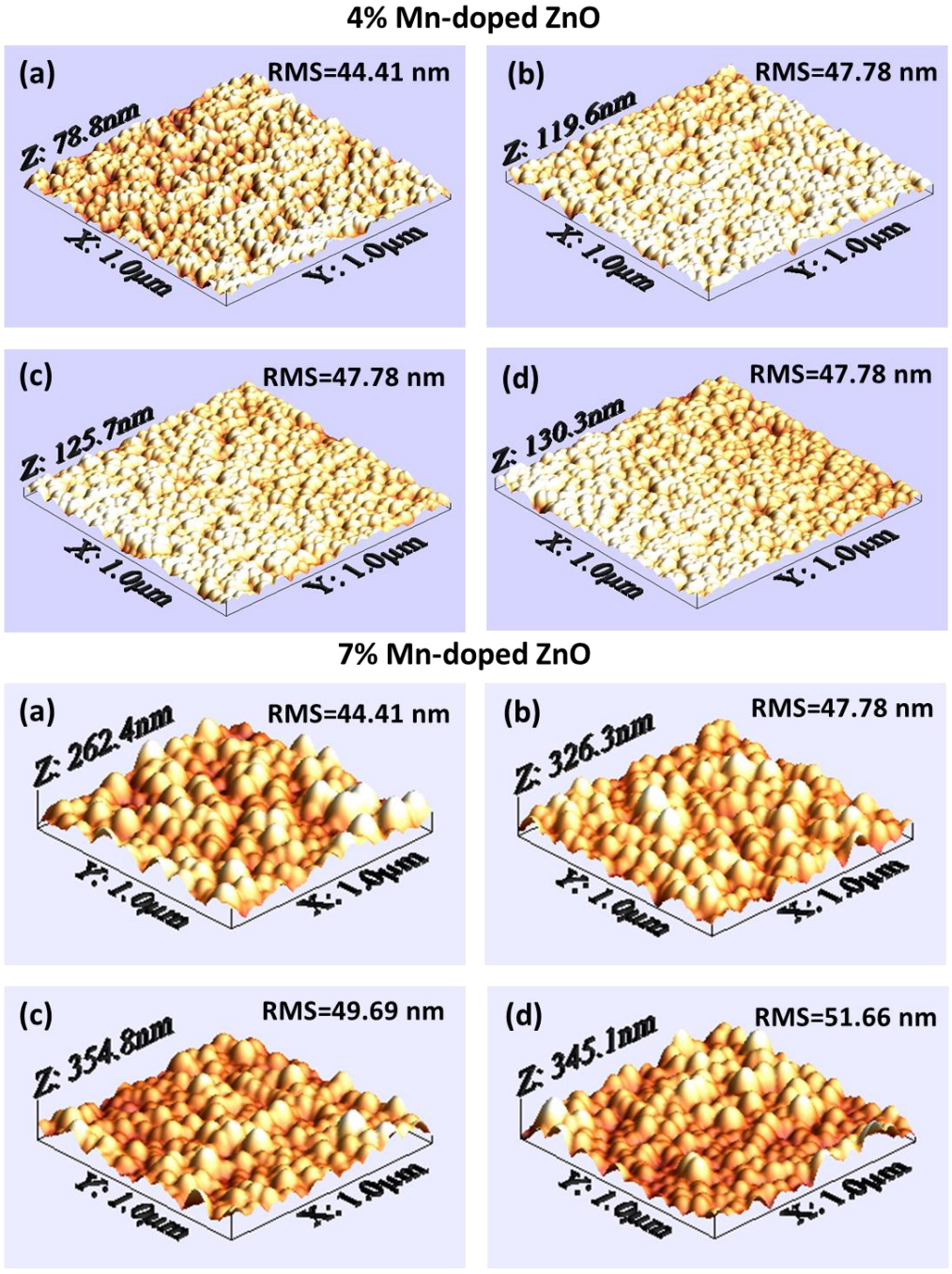

Figure IV. 8. 3D AFM images of 4% and 7% Mn-doped ZnO thin films; (a) 5 layers, (b) 10 layers, (c) 15 layers, (d) 20 layers.

Table IV. 3. Grain size from AFM of Pure ZnO, 4% and 7% Mn-doped ZnO thin films for various deposited layers.

Coating number	Grain size from AFM (nm)		
	Pure ZnO	4% Mn-doped ZnO	7% Mn-doped ZnO
05	54.60	27.80	46.33
10	64.86	32.43	50.96
15	46.33	41.70	55.59
20	70.31	55.59	62.50

IV.2.3.1.3 Comparison

- The samples present a uniform growth, the grains are round shape in plane for all samples, and their size generally increases by increasing the coating number for both doped and pure ZnO thin films.
- The surface roughness of the films was found to be increased with thickness for both doped and pure ZnO thin films.
- At the same coating number, the graine size values of 4% Mn- doped ZnO thin film are higher than those of 7%. However, the roughness of 4% Mn- doped ZnO are lower than those of 7%.

IV.2.3.2 FESEM analysis

IV.2.3.2.1 Pure ZnO

FESEM analysis was also used to investigate the morphology properties of pure ZnO thin films **(Figure IV.9)**. A wrinkled microstructure was observed, which is distributed homogenously over the whole film surface. As the thickness increased, the width, length, and height of wrinkles were increased. Also, cracks appeared from the sample of 10 layers **(Figure IV.9b)**, whereas the sample of 5 layers **(Figure IV.9a)** is without cracks. The width of cracks increased with increasing thickness. Similar surface shape was observed in ZnO films prepared by sol-gel dip coating method

on glass substrate [179]. Also, this surface shape was observed for ZnO thin films deposited onto alkali-free glass substrates by sol-gel spin coating technique [180].

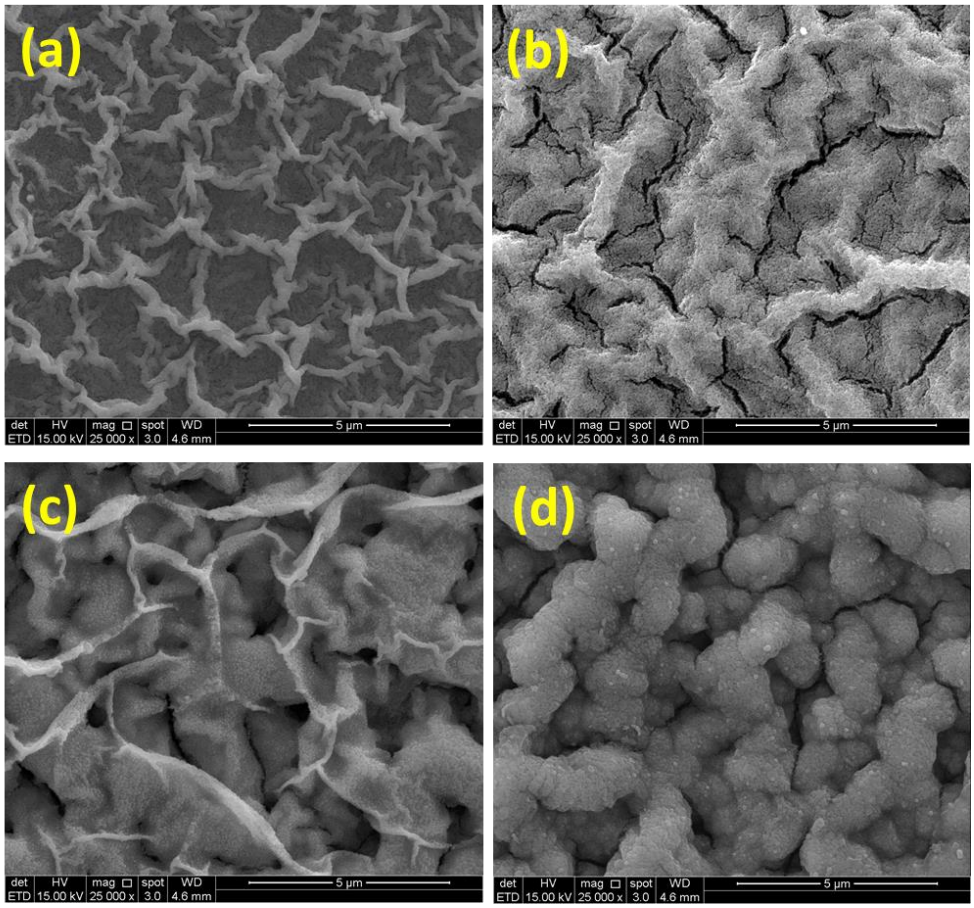

Figure IV. 9. FESEM images of pure ZnO thin films: (a) 5, (b) 10, (c) 15, and (d) 20 layers.

IV.2.3.2.2 Mn-doped ZnO

The morphology properties of 7% Mn-doped ZnO thin films with various thicknesses were also investigated by FESEM analysis **(Figure IV.10)** (FESEM analysis of 4% Mn- doped ZnO films were not performed). A wrinkled microstructure was observed, which is distributed homogenously over the whole film surface. The width, length, and height of wrinkles were increased with thickness. Also, cracks were observed in the samples **(Figure IV.10b)**. The width

of cracks increased with increasing thickness. Similar surface shape was observed for Ni-doped ZnO [181].

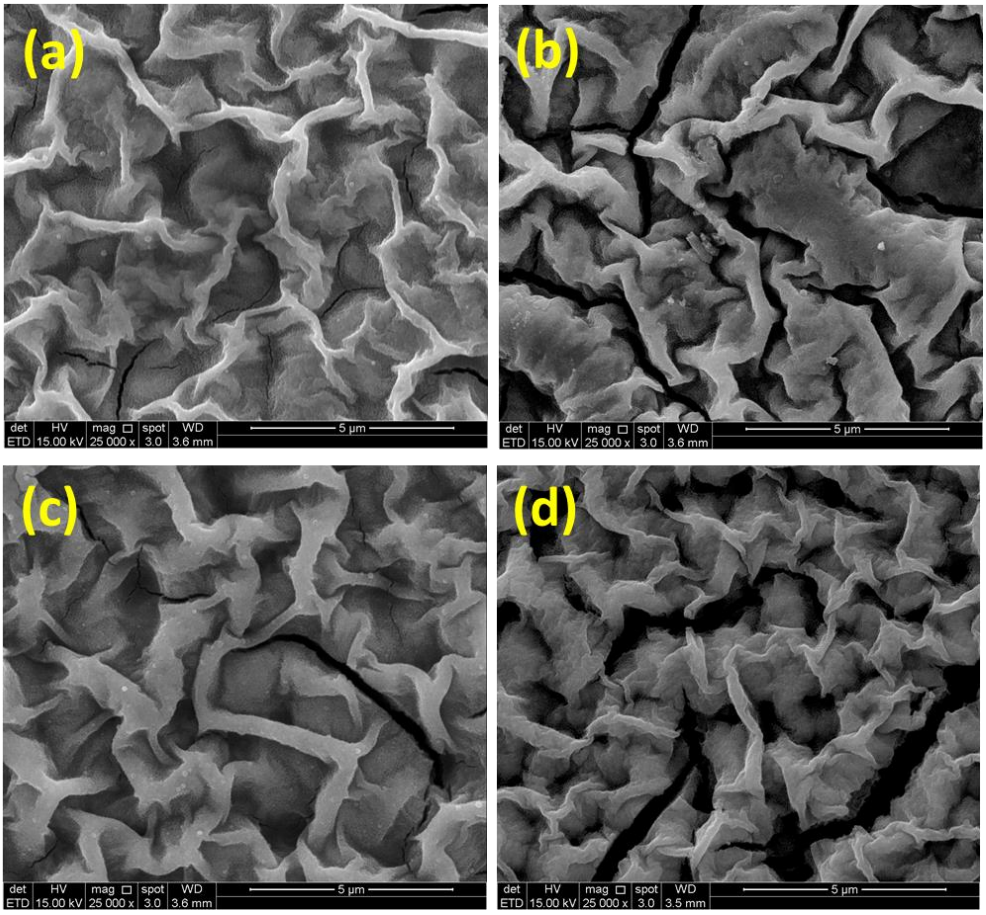

Figure IV. 10. FESEM images of 7% Mn-doped ZnO thin films: (a) 5, (b) 10, (c) 15, and (d) 20 layers.

IV.2.3.2.3 Comparison

- A wrinkled microstructure, homogenously distributed over the whole film surface, was observed for both pure and Mn-doped ZnO thin films, and their width, length, and height were increased with thickness.
- Cracks were appeared from the samples of 10 layers for both pure and Mn-doped ZnO thin films, and their width increased with increasing the thickness.

- The samples of 5 layers are without cracks for both pure and Mn-doped ZnO thin films.

IV.2.4 Optical properties

IV.2.4.1 UV-Visible analysis

IV.2.4.1.1 Pure ZnO

To investigate the effect of film thickness on the optical properties of pure ZnO thin films, UV-vis spectra were measured in the wavelength range of 350–800 nm at room temperature **(Figure IV.11)**. In the visible region, the average transmittance generally decreases with the increase of coating number **(inset of Figure IV.11)**. It is well known that the film becomes thicker as the coating number increases, which may affect the scattering of light and then decreases the transmittance for pure ZnO thin films [20, 21, 91].

However, a sharp absorption edge was observed. By increasing the thickness, a red shift of the absorption edge was also observed. The slight shift toward the large wavelengths could be attributed to the decrease of the carrier concentration ascribed to the increase in the grain size and the enhancement of the crystalline quality [24]. This result shows that the bandgap slightly decreases from 3.28 to 3.26 eV as the film thickness increases.

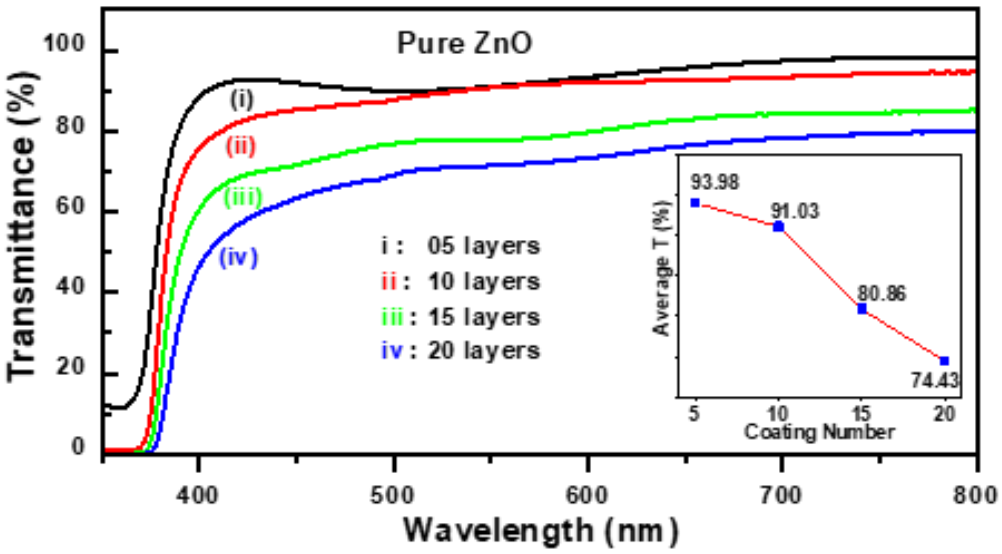

Figure IV. 11. Transmittance spectra of pure ZnO thin films for various deposited layers, with their average transmittance in the inset.

Optical constants such as refractive index (n) and extinction coefficient (k) can be determined from the transmittance data by using the following equations [74, 182, 183]:

$$A = \log(1/T) \quad \text{(IV.7)}$$

$$R = 1 - \mathrm{A} - \mathrm{T} \quad \text{(IV.8)}$$

$$\alpha = 2.303\ \mathrm{A/t} \quad \text{(IV.9)}$$

$$k = \alpha\lambda/4\pi \quad \text{(IV.10)}$$

$$n = (1+R)/(1-R) + \sqrt{4R/(1-R)^2 - k^2} \quad \text{(IV.11)}$$

where T is the transmittance, R is the reflectance, A is the absorbance, t is the film thickness, α is the absorption coefficient and λ is the wavelength. The variation of k and n is presented for pure ZnO thin films **(Figure IV.12)**. For all the films, the refractive index varies sharply near the optical edge and tends to be constant for the medium and low energy in the visible

region. By increasing the coating number (thickness), the refractive index increases and shifts to lower values of energy for pure ZnO thin films. Similar behavior is observed by other researchers for pure ZnO [32, 74, 182, 184].

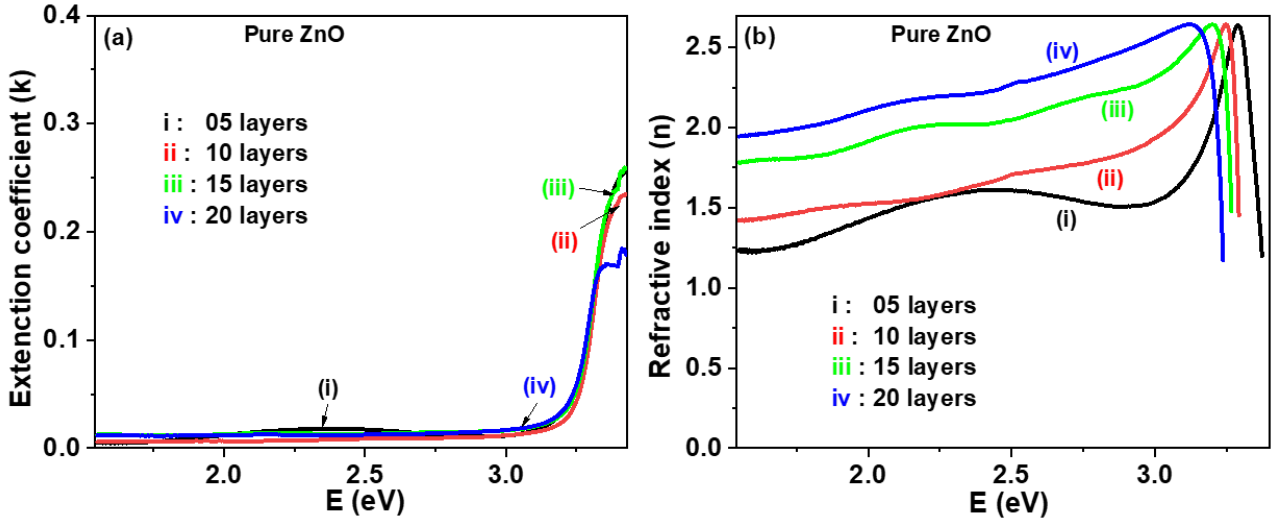

Figure IV. 12. Optical constants; (a) extinction coefficient and (b) refractive index of pure ZnO thin films for various deposited layers.

The absorption coefficient, previously calculated, was then used to evaluate the bandgap (E_g) by utilizing the Tauc's equation [53]. The $(\alpha h\nu)^2$ vs. photon energy $h\nu$ was plotted for various deposited layers **(Figure IV.13)**. The bandgap slightly decreases from 3.28 to 3.26 eV when the coating number is increased from 5 to 20.

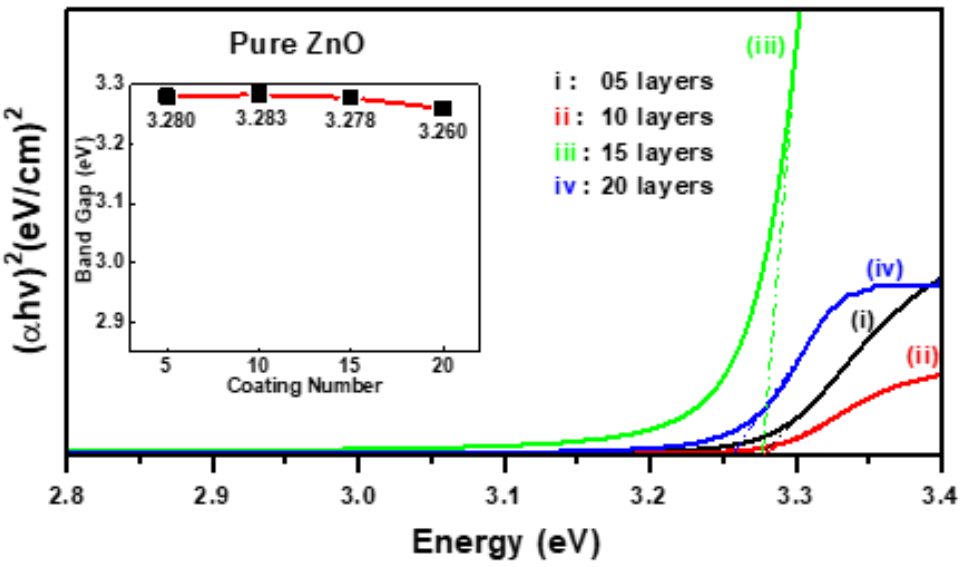

Figure IV. 13. $(\alpha hv)^2$ versus photon energy hν of pure ZnO thin films for various deposited layers. Bandgap variation was also shown in the inset.

IV.2.4.1.2 Mn-doped ZnO

The optical properties of 4% **(Figure IV.14a)** and 7% **(Figure IV.14b)** Mn-doped ZnO thin films for various film thickness were investigated. The UV-visible was performed in the wavelength range of 350- 800 nm at room temperature. In the visible range, the transmittance generally decreased with the increase of coating number for both Mn-doped ZnO thin films **(insets of Figure IV.14)**. A blunt absorption edge was observed for all Mn-doped thin films by increasing the thickness. Also, a red shift of the absorption edge was observed.

The higher average transmittance was found at the lowest thickness (sample of 5 layers), which was less than 45% for 4% doped Mn and less than 40% for 4% doped Mn films. It was known that the increase of the film thickness affects the scattering of light and then decreased the transmittance. Also, the increase in Mn content decreased the transmittance. Similar behavior of

average transmittance variation with thickness was found in a study of 5% Mn-doped ZnO thin films deposited by RF magnetron sputtering [27].

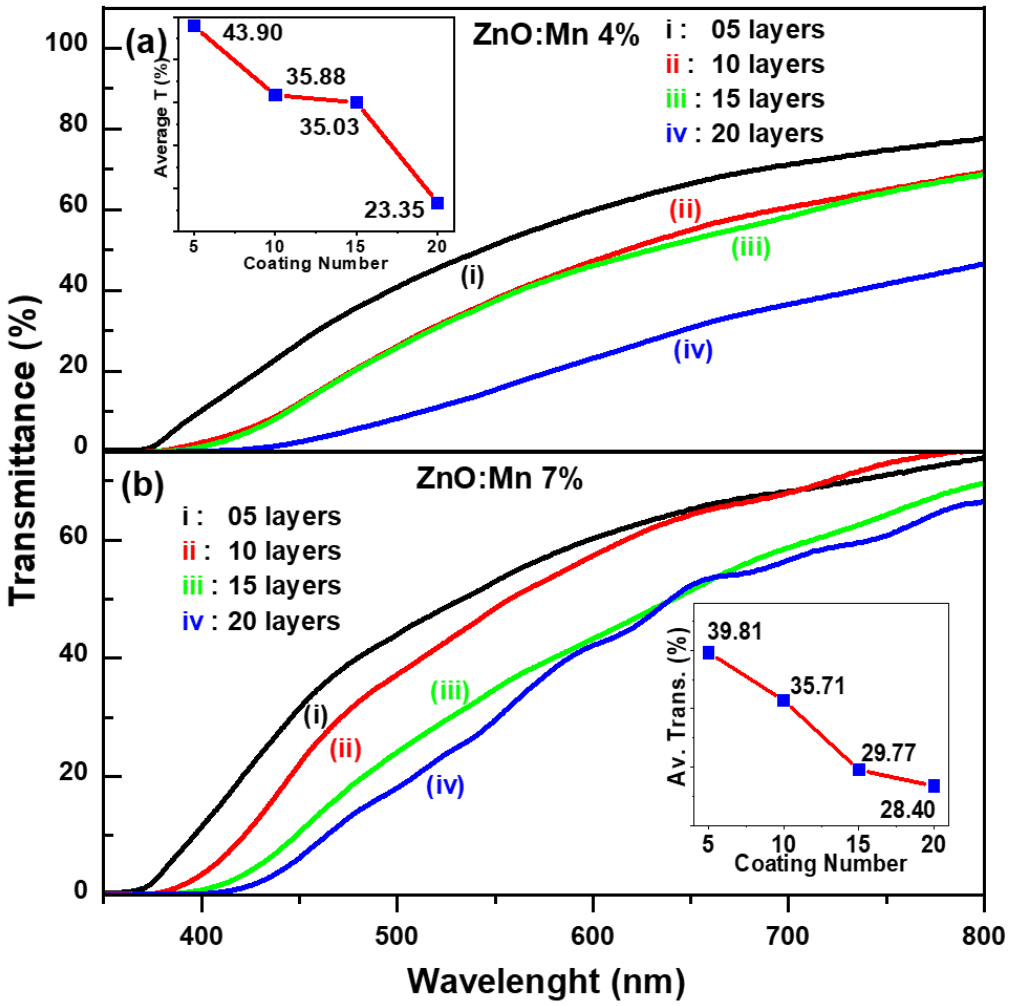

Figure IV. 14. Transmittance spectra of (a) 4% and (b) 7% Mn-doped ZnO thin films for various deposited layers, with their average transmittance in the insets.

The refractive index (*n*) and extinction coefficient (*k*) of 4% and 7% Mn-doped ZnO thin films was determined from the transmittance data by the **equations (IV.7-11)** and then presented **(Figure IV.15)**.

As pure ZnO thin films, the refractive index varies sharply near the optical edge and tends to be constant for the medium and low energy in the visible region for both 4% and 7% films. By increasing the coating number (thickness), the refractive index increases and shifts to lower values of energy with an appreciable amount for both 4% and 7% Mn-doped ZnO thin films. Also, the optical absorption edges for the extinction coefficient are clearly seen and predict a noticeable variation of band gap with coating number.

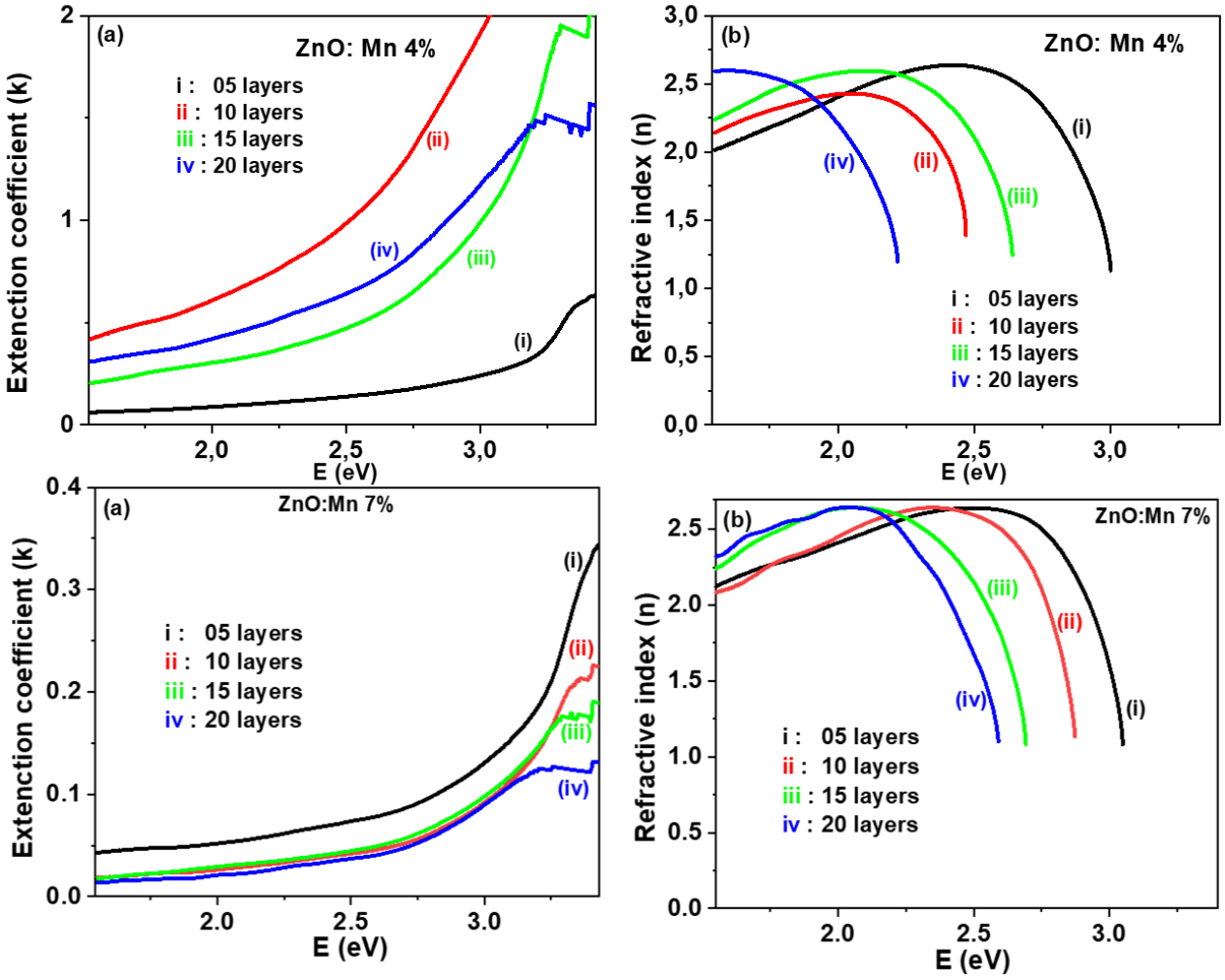

Figure IV. 15. Optical constants; (a) extinction coefficient and (b) refractive index of 4% and 7% Mn-doped ZnO thin films for various deposited layers.

The $(\alpha h\nu)^2$ vs. photon energy $h\nu$ for 4% **(Figure IV.16a)** and 7% **(Figure IV.16b)** Mn-doped ZnO thin films were plotted for various coating number. The coefficient (α) was determined (α) using Lambert's law and then used to evaluate the band gap (E_g) by utilizing the Tauc equation [8] . The result showed an appreciable decrease in the band gap values from 3.20 to 2.88 eV when the coating number increased from 5 to 20 layers for both 4% and 7% Mn-doped ZnO thin films **(insets of Figure IV.16)**. This variation caused by the change of strain along the c-axis [27] .

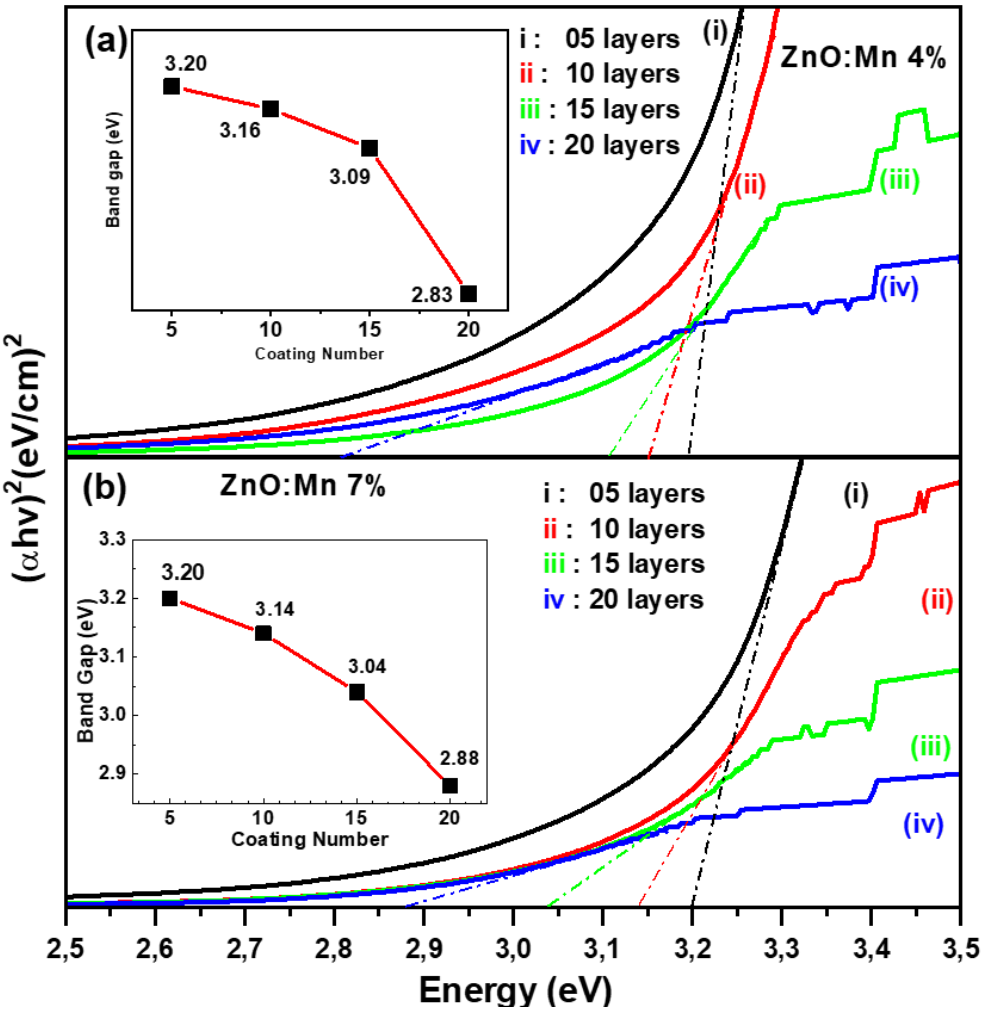

Figure IV. 16. $(\alpha h\nu)^2$ versus photon energy hν of (a) 4% and (b) 7% Mn-doped ZnO thin films for various deposited layers. Bandgap variation was also shown in the insets.

IV.2.4.1.3 Comparison

- The average transmittance values of the pure ZnO thin films **(inset of Figure IV.11)** are higher than those of Mn-doped ZnO ones **(insets of Figure IV.14)** at the same coating number, indicating a good visible transparency for pure ZnO thin films. This may be due to the increase in optical scattering caused by the decrease of grain size for Mn-doped thin films [2]. Also, the average transmittance decreases with the increase of Mn content.
- A sharp absorption edge was observed for pure ZnO thin films and blunt for 4% and 7% Mn-doped ZnO films. Also, a red shift of the absorption edge with thickness was observed for pure and Mn-doped thin films.
- The refractive index increases with thickness and shifts to lower values of energy with an appreciable amount for 4% and 7% Mn-doped ZnO thin films than for pure ZnO thin films. The decrease in crystallite size of Mn-doped ZnO thin films compared to the pure ones **(Table IV.1)** causes an increase in film density and then an increase in refractive index [183].
- The optical absorption edges for the extinction coefficient are clearly seen and predict a noticeable variation of band gap with coating number for Mn-doped ZnO than pure ZnO.
- The bandgap values of pure ZnO thin films **(inset of Figure IV.13)** are higher than those of the Mn-doped ZnO **(inset of Figure IV.16)**. This may be attributed to the shrinking of the bandgap caused by the merging of an impurity band near the conduction band caused by the exchange interaction between localized states of the transition metal ions and s-p states of the host band [10, 178]. Also, the band gap of 4% and 7% Mn-doped ZnO thin films are almost equals at the same coating layers.

IV.2.4.2 PL analysis

IV.2.4.2.1 Pure ZnO

The effect of the coating number on the PL properties of pure ZnO thin films were investigated **(Figure IV.17)**. The obtained experimental data of PL spectra were fitted by multi-peak Gaussian shape **(insets of Figure IV.17)**. Two major peaks were shown in the PL spectra: the near-band-edge emission centered at 387 nm, which is due to free exciton emission [53], and broad blue emission centered at 439 nm. A second blue emission at around 475 nm can be seen for pure ZnO thin films. The samples also show a weak green emission with a peak centered at 525 nm.

The origin of these emissions has not been decisively understood where many researchers suggested various origins for the same peak in the visible emission region [185-187]. The broad and strong blue emission at around 439 nm could be originated from transition from interstitial Zn_i to the valence band; the second blue emission may be attributed to the electron transition from the oxygen vacancy level to the valence band; and the green emission, as quoted by some researchers, may be due to the transition from conduction band to the O_{Zn} level [185, 188].

As the film thickness increases, the intensity of the visible emission increases for pure ZnO thin films, which is affected by the appreciable change in the grain size and defect concentration of the pure ZnO [10, 21].

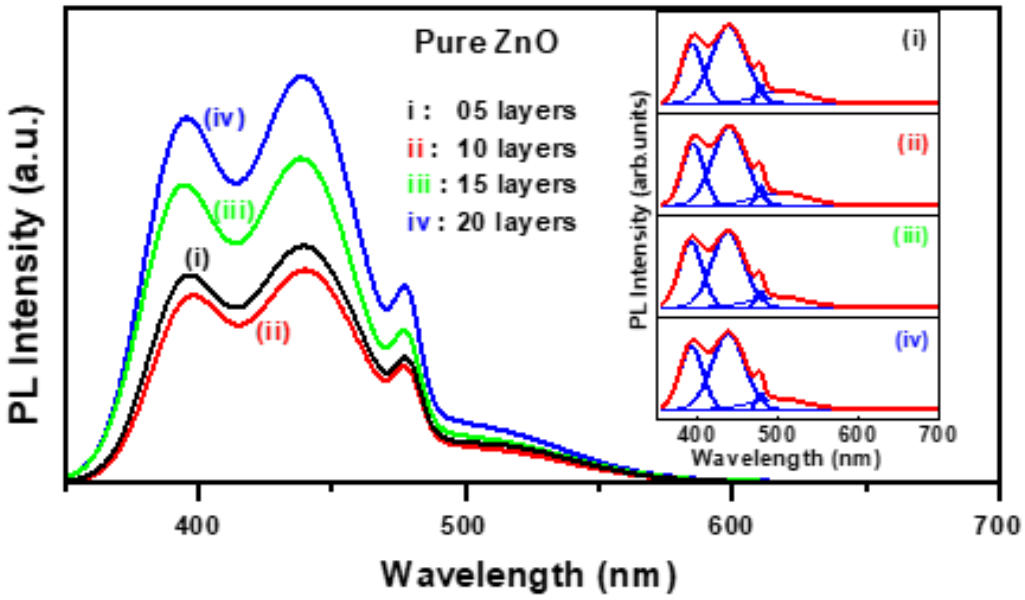

Figure IV. 17. Photoluminescence (PL) spectra of pure ZnO thin films for various deposited layers. Multi-peak Gaussian fits were also shown in the inset.

IV.2.4.2.2 Mn-doped ZnO

The photoluminescence (PL) properties of 4% **(Figure IV.18a)** and 7% **(Figure IV.18b)** Mn-doped ZnO thin films for various thickness were investigated. The obtained experimental data of PL spectra exhibited in multi-peak Gaussian shape **(insets of Figure IV.18)**. For all Mn- doped films, two major peaks were shown; near-band-edge (NBE) emission centered at 388 nm, and broad blue emission at 438 nm. A second blue emission at 475 nm was seen with a weak green emission peak centered at 525 nm. The origin of the near-band-edge (NBE) emission was due to free exciton emission [53]. However, the origin of the emissions in the visible region has not been exactly determined. Many researchers proposed the origins for these emission peaks at the same wavelength [185-187]. The blue emissions originated from transition from interstitial Zn_i to the valence band (peak around 438 nm) or transition from the oxygen vacancies level to the valence band (peak around 475 nm). The green emission peak at 525 nm attributed to the transition from

conduction band to the O_{Zn} level [8, 10]. The intensity of the visible emission peaks generally decreases with the increase of thickness for both 4% and 7% Mn-doped ZnO thin films.

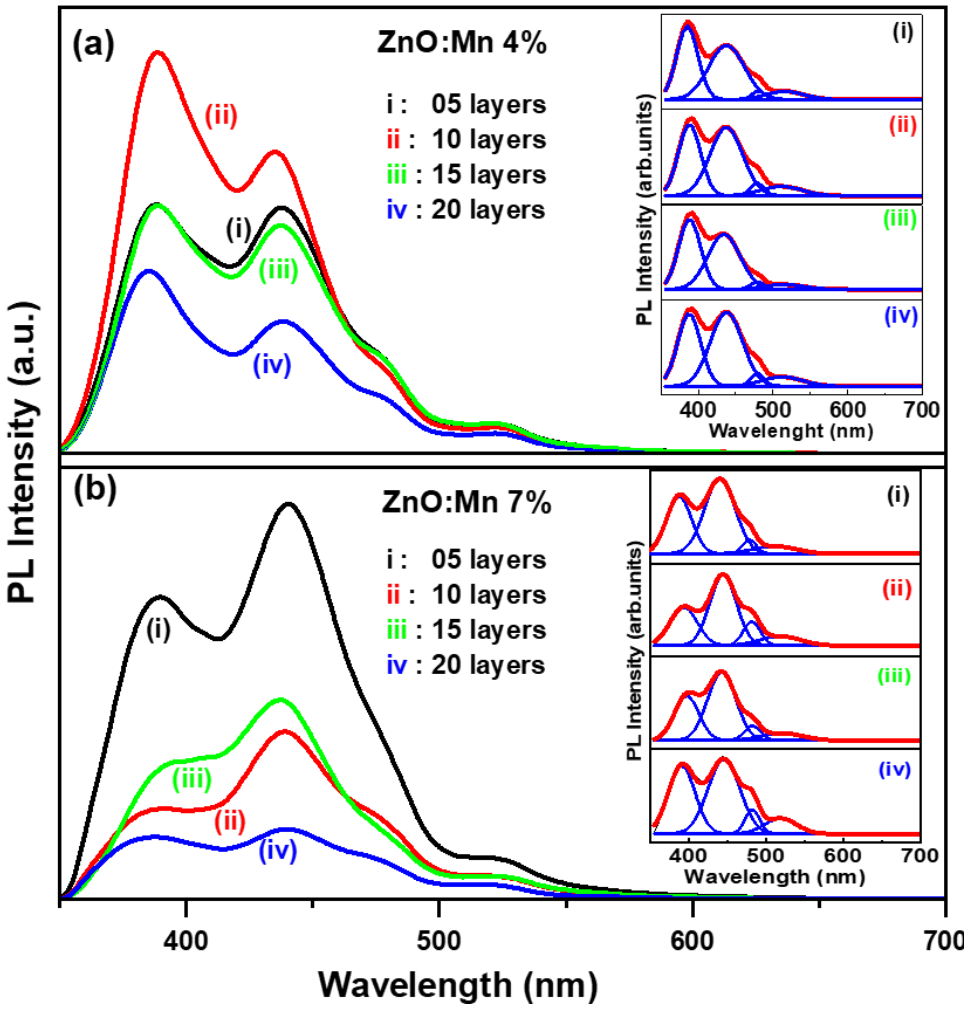

Figure IV. 18. Photoluminescence (PL) spectra of 7 % Mn-doped ZnO thin films for various deposited layers. Multi-peak Gaussian fits were also shown in the inset.

IV.2.4.2.3 Comparison

- The second blue emission at around 475 nm which can be seen for pure, 4% and 7% Mn-doped ZnO thin films, it becomes more pronounced for pure ZnO thin films and vanishes progressively for Mn-doped ZnO thin films with thickness. This indicates that the oxygen

vacancy concentration is decreased for Mn-doped ZnO thin films with thickness, which may be due to the formation of multilayer Mn segregation in ZnO grain boundary [189].

- By increasing the thickness, the intensity of the visible emission increases for pure ZnO thin films, which is affected by the appreciable change in the grain size and defect concentration of the pure ZnO [10, 21] while it decreases for the doped thin films.

IV.3 Calculation results

IV.3.1 Structural properties

The pure and Mn-doped ZnO lattice parameters were calculated**.** The geometry optimization results are performed with the plane wave ultrasoft pseudopotential using the generalized gradient approximation (GGA) with the PW91 functional as implemented in CASTEP code [132]. The optimized lattice constants of pure (a=b = 3.236Å and c = 5.202Å) and Mn-doped (a=b = 3.255Å and c = 5.238Å) ZnO structures are slightly increased with Mn concentration, which are comparable with our experimental results. This increase is due to the fact that the ionic radius of Zn^{2+} (0.74 Å) is smaller than that of Mn^{2+} (0.83 Å) [190].

IV.3.2 Electronic properties

IV.3.2.1 Band structure and density of states

To analyze the electronic properties, the energy band structures (**Figures IV.19a** and **IV.19b)** and partial density of O2s, O2p, Zn 4s, Zn 3d, Mn 4s and Mn 3d states, PDOS, (**Figure IV.19c, IV.19d** and **IV.19e),** are shown for pure and Mn-doped ZnO structures. It is observed that both structures are direct band gap at G point; Eg = 3.381 eV for pure ZnO and Eg = 3.246 eV for Mn-doped ZnO. However, the incorporation of the semi-empirical GGA+U approach with appropriate effective Hubbard U values improves significantly the theoretical direct bandgap

values compared to our values obtained without taking into account the Hubbard correction (Eg = 0.742 eV for pure ZnO and Eg = 0.003 eV for Mn-doped ZnO) and to other previous results [64, 191].

By incorporating Mn atoms, the conduction band, which is mainly originated from Zn *4s* with some mixture of Mn *3d*, O *2p* states, and a little Mn *4s* effect, shrinks and shifts downward to Fermi level, which slightly decreases the bandgap **(Figures IV.19c, d** and **e)**. On the other hand, the top of valence band appears to be relatively flat within a region of 7.5 eV and is mainly originated from mixture of O *2p* and Zn *3d* states with a little contribution from Mn *3d* states. These latter states seem to be distributed far from Fermi level.

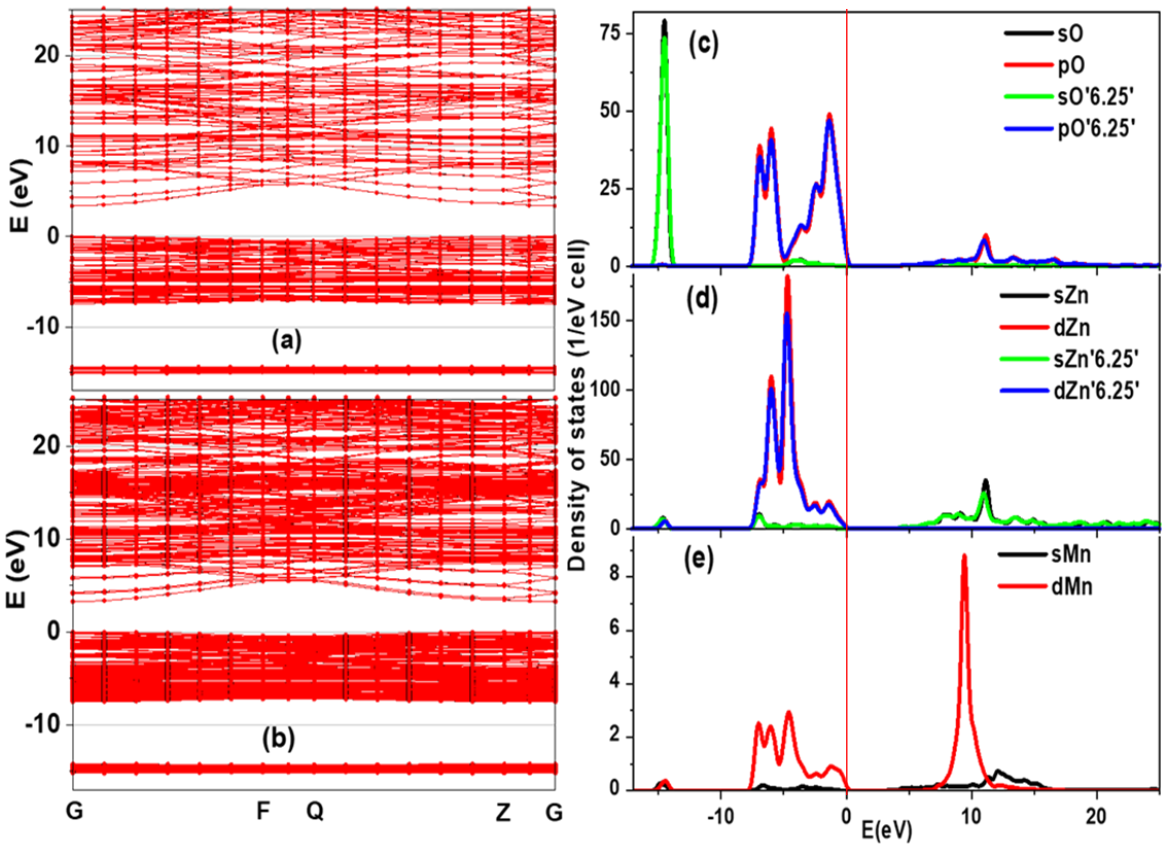

Figure IV. 19. Band structure of pure (a) and Mn-doped (b) ZnO structures and partial density of States (PDOS); (c) O 2s, O2p, (d) Zn 4s, Zn 3d, (e) Mn 4s and Mn 3d states.

IV.3.2.2 Charge density and Mulliken population

The average Mulliken charges are found to be as follows: for pure ZnO, Zn: 0.950e, and O: -0.950e, and for Mn-doped ZnO, Zn: 0.955e, Mn: 0.960e, and O: -0.954e. Then, the effective valence of Zn is 1.050 for pure ZnO and that of Zn is 1.045 and Mn is 1.040 for Mn-doped ZnO. This indicates the coexistence of both ionic and covalent bonding either for pure or Mn-doped ZnO structures.

The distribution (010) surfaces of charge density difference were studied for pure **(Figure IV.20a)** and Mn-doped **(Figure IV.20b)** ZnO structures. Yellow regions show charge loss (depletion), red regions represent charge accumulation, and blue color indicates a region with minimal difference. This is consistent with the results obtained for the atomic population; the more the atom has effective valence, the more it attracts electrons.

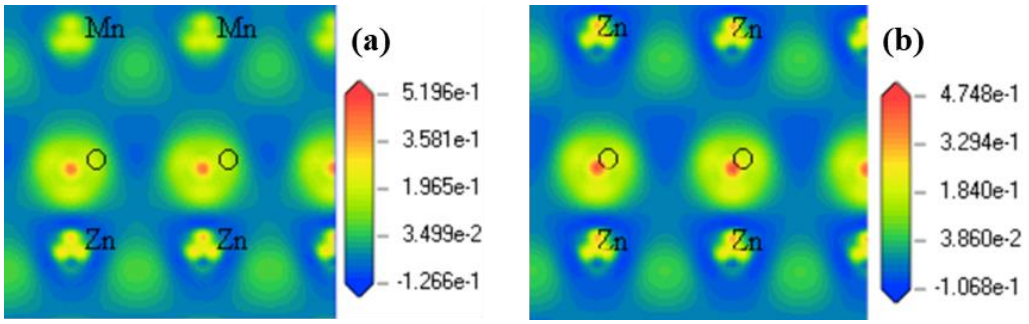

Figure IV. 20. Distribution (010) surface of charge density difference for (a) pure and (b) Mn-doped ZnO.

IV.3.3 Optical properties

The frequency-dependent dielectric function is the main parameter to deduce the optical properties of materials [192, 193]. Both pure and Mn-doped ZnO structures present similar behavior in the complex dielectric function **(Figure IV.21a)**. The peak intensities of pure material are all slightly higher than those of Mn-doped material because of the replacement of Zn atoms by

Mn ones. There is an exception within a narrow energy range (10.5–10.9 eV), where a peak is appeared at around 10.7 eV **(insets of Figure IV.21a)**. This peak may be mainly derived from the transition between the O *2p* and Mn *3d* orbitals. The shrinking of bandgap energy for doped material causes a slight shift of dielectric function toward the lower energy of incident photon.

The calculated refractive index and extinction coefficient are also shown **(Figure IV.21b)** for pure and Mn-doped ZnO structures. The extinction coefficient presents a sharp increase near the optical edge with slight shift to lower energy for Mn-doped ZnO structure (**Inset in Figure IV.21b)**. The refractive index tends to be constant for lower photon energy in the visible region (around 1.56 for pure and 1.55 for Mn-doped ZnO structure). Both refractive index and extinction coefficient exhibit a similar behavior to those deduced from experiment in this work within the considered energy range of the incident photon (1.55-3.5 eV).

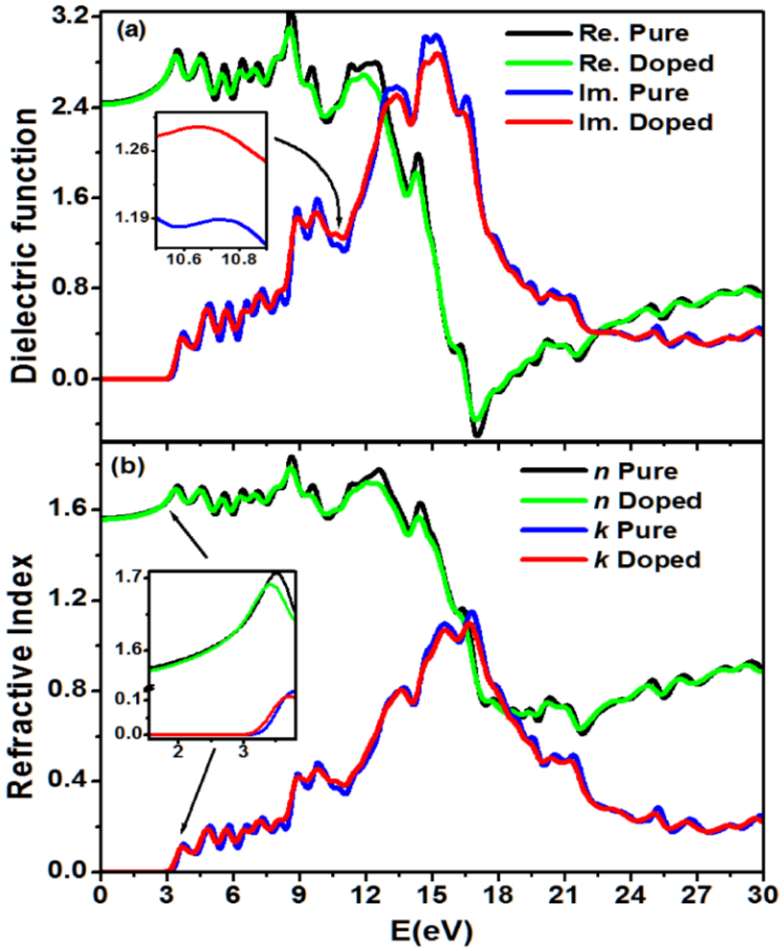

Figure IV. 21. Complex dielectric function (a) and refractive index, n, and extinction coefficient, k, (b) for pure ZnO and Mn-doped ZnO structures. Inset in (a) shows dielectric function within the energy range 10.5-10.9 eV. Inset in (b) shows n and k within the visible range of photon energy.

IV.4 Conclusion

The thickness effects of pure ZnO, 4% and 7% Mn-doped ZnO thin films on glass substrates, obtained by sol-gel spin coating method, were characterized and calculated by GGA + U. All films present a polycrystalline hexagonal wurtzite structure with a preferential orientation along the (002) axis. A uniform growth and round shape in plane of grains are observed, and their grain size slightly increases by increasing the thickness. A wrinkled microstructure is homogeneously distributed in pure and Mn-doped ZnO thin films, whose roughness is found to be increased with thickness. The transmittance and bandgap were found to be decreased for both pure and doped ZnO films with thickness, where the bandgap slightly decreases for the pure ZnO films. The high PL properties are remarked at low thickness for Mn-doped ZnO films and at high thickness for pure ZnO films. The GGA + U approach improves the theoretical direct bandgap values. The covalency of bonds is slightly influenced from pure to Mn-doped ZnO structure, and both ionic and covalent bonding are coexisted. Combination of experimental and theoretical from this work will shed light on designing Mn-doped ZnO thin films for optical, sensors and solar cell applications".

V. General conclusion

V.1 General conclusion

This work is devoted to investigate the effect of thickness on the physical properties of pure, 4% and 7% Mn doped ZnO thin films. The synthesis of our samples was done by the sol-gel spin-coating technique. Zinc acetate dihydrate, Manganese acetate tetrahydrate, isopropanol and monoethanolamine (MEA) were used as precursor, solvent and stabilizer, respectively. The pure and doped films were deposited on glass substrate. The molar concentration of ZnO precursor is 0.7 mol / L, and the doping concentration for Mn-doped ZnO, is 4 % and 7%. To increase the thickness, the deposition process was repeated 05, 10, 15 and 20 times.

In order to obtain the physical properties of our samples, several characterizations were carried out: Structural and morphological characterization: X-ray diffraction (XRD), Field emission scanning electron microscope (FESEM), atomic force microscope (AFM); Optical properties: UV- Visible measurement of transmittance, and photoluminescence (PL) of films. The thickness of all films was measured by a profilometer.

Furthermore, first-principles calculations of structural, electronic, and optical properties of pure and 6.25% Mn- doped ZnO wurtzite materials were performed by DFT and Hubbard (GGA + U) semi-empirical approach method as implemented in CASTEP code. The generalized gradient approximation (GGA) in the scheme of Perdew–Burke–Ernzerhof (PBE) was used to treat the exchange-correlation function. ZnO supercell model, derived from the optimized ZnO wurtzite primitive cell, and substitutional method were used to achieve the considered Mn content.

To confirm the convergence in the calculation, appropriate computer input criteria, such as valence-electron atomic configurations of O, Zn and Mn, energy cut-off, pseudopotential, sampling of the Brillouin zone by k-point mesh, optimization convergence for maximum force,

energy change, maximum displacements, maximum stress and the SCF convergence threshold were adopted on the basis of previous theoretical studies.

In the thickness measurement, the film thickness was increased with coating number for both pure and doped ZnO. The average thickness of each layer was found to be 50 nm for pure ZnO and 90 nm for 7% Mn-doped ZnO and 150 nm for 4% Mn doped ZnO.

The X-ray diffraction showed that all films present a polycrystalline hexagonal wurtzite structure with a preferential orientation along the c-axis. The (002) intensity peak was increased with thickness for 4% and 7% Mn-doped ZnO films. However, for pure ZnO films, the (002) peak increased up to 15 layers and then decreased while the (100) and (101) peaks increased with thickness. The crystallite size, strain and growth mode are significantly influenced by the increasing of thickness.

Morphological analyzes have shown a good uniformity of the produced films. The grain size and the surface roughness slightly increase by increasing the thickness. A wrinkled microstructure is homogeneously distributed in pure and 7% Mn-doped ZnO thin films, whose roughness is found to be increased with thickness.

Optical measurements using UV-Vis transmittance revealed that the average transmittance and bandgap decreased with thickness for pure, 4% and 7% Mn- doped ZnO films, with a slight decrease in the bandgap for pure ZnO films. And both were decreased when going from pure to Mn doped ZnO.

The photoluminescence of all films showed ultraviolet (UV) emissions and several visible emissions such as violet, blue, green, corresponding to near band edges (NBE) and the various structural defects. A second blue emission peak at 475 nm was observed more pronounce for pure

ZnO compared to doped films. The luminescence intensity increases with thickness for pure ZnO films and it decreases for Mn doped films.

DFT+U calculations reveal that the bandgap energy decreases from pure (3.381 eV) to 6.25% Mn-doped ZnO (3.246 eV) material, which are both enhanced by effective Hubbard U values. The covalency of bonds is slightly influenced from pure to Mn-doped ZnO structure, and both ionic and covalent bonding are coexisted. Also, the Mn3d states were distributed far from Fermi level with a coexistence of both ionic and covalent nature bonds. A slight shift toward the lower energy was noticed for optical properties by Mn doping.

Finally, it should be noted that two valuable results can be drawn from this study. First, all physical properties of thin films were found to be influenced by thickness variation, indicating that the thickness of films is an important parameter which must be controlled for suitable use in a potential application. Second, DFT+U correction in standard DFT shows that practical effective U values significantly enhance the band gap energy and its corresponding optical and electronic properties.

VI. List of references

[1] P.T. Moseley, Progress in the development of semiconducting metal oxide gas sensors: a review, Measurement Science and Technology, 28 (2017) 082001.
[2] S. Lany, Semiconducting transition metal oxides, Journal of Physics: Condensed Matter, 27 (2015) 283203.
[3] A. Dey, Semiconductor metal oxide gas sensors: A review, Materials Science and Engineering: B, 229 (2018) 206-217.
[4] F.U. Hamelmann, Transparent Conductive Oxides in Thin Film Photovoltaics, Journal of Physics: Conference Series, 559 (2014) 012016.
[5] M. Soylu, M. Coskun, Controlling the properties of ZnO thin films by varying precursor concentration, J. Alloys Compd., 741 (2018) 957-968.
[6] D. Pal, J. Singhal, A. Mathur, A. Singh, S. Dutta, S. Zollner, S. Chattopadhyay, Effect of substrates and thickness on optical properties in atomic layer deposition grown ZnO thin films, Appl. Surf. Sci., 421 (2017) 341-348.
[7] A. Namoune, T. Touam, A.J.J.o.M.S.M.i.E. Chelouche, Thickness, annealing and substrate effects on structural, morphological, optical and waveguiding properties of RF sputtered ZnO thin films, 28 (2017) 12207-12219.
[8] A. Mahroug, R. Amari, A. Boukhari, B. Deghfel, L. Guerbous, N. Selmi, Synthesis, Structural, Morphological, Electronic, Optical and Luminescence Properties of Pure and Manganese-Doped Zinc Oxide Nanostructured Thin Films: Effect of Doping, Journal of Nanoelectronics and Optoelectronics, 13 (2018) 732-742.
[9] B. Ghanbari Shohany, A. Khorsand Zak, Doped ZnO nanostructures with selected elements - Structural, morphology and optical properties: A review, Ceram. Int., 46 (2020) 5507-5520.
[10] S. Yang, Y. Zhang, Structural, optical and magnetic properties of Mn-doped ZnO thin films prepared by sol–gel method, J. Magn. Magn. Mater., 334 (2013) 52-58.
[11] X. Li, X. Zhu, K. Jin, D. yang, Study on structural and optical properties of Mn-doped ZnO thin films by sol-gel method, Optical Materials, 100 (2020) 109657.
[12] S. Aksoy, Y. Caglar, Synthesis of Mn doped ZnO nanopowders by MW-HTS and its structural, morphological and optical characteristics, J. Alloys Compd., 781 (2019) 929-935.
[13] M. Shatnawi, A.M. Alsmadi, I. Bsoul, B. Salameh, M. Mathai, G. Alnawashi, G.M. Alzoubi, F. Al-Dweri, M.S. Bawa'aneh, Influence of Mn doping on the magnetic and optical properties of ZnO nanocrystalline particles, Results in Physics, 6 (2016) 1064-1071.
[14] V. Kumar, S.K. Singh, H. Sharma, S. Kumar, M.K. Banerjee, A. Vij, Investigation of structural and optical properties of ZnO thin films of different thickness grown by pulsed laser deposition method, Physica B: Condensed Matter, 552 (2019) 221-226.
[15] L. Miao, S. Tanemura, M. Tanemura, S.P. Lau, B.K.J.J.o.M.S.M.i.E. Tay, Thickness-dependent optical properties of ZnO thin films, 18 (2007) 343-346.
[16] T. Prasada Rao, M.C. Santhoshkumar, Effect of thickness on structural, optical and electrical properties of nanostructured ZnO thin films by spray pyrolysis, Appl. Surf. Sci., 255 (2009) 4579-4584.
[17] A. Mortezaali, O. Taheri, Z.S. Hosseini, Thickness effect of nanostructured ZnO thin films prepared by spray method on structural, morphological and optical properties, Microelectron. Eng., 151 (2016) 19-23.
[18] K. Kandpal, J. Singh, N. Gupta, C.J.J.o.M.S.M.i.E. Shekhar, Effect of thickness on the properties of ZnO thin films prepared by reactive RF sputtering, 29 (2018) 14501-14507.

[19] F.J.J.o.E.D. Chowdhury, Influence of thickness variation on the optical properties of ZnO thin films prepared by thermal evaporation method, Journal of Electron Devices, 10 (2011) 448-455.
[20] N. Kakati, S.H. Jee, S.H. Kim, J.Y. Oh, Y.S. Yoon, Thickness dependency of sol-gel derived ZnO thin films on gas sensing behaviors, Thin Solid Films, 519 (2010) 494-498.
[21] L. Xu, X. Li, Y. Chen, F. Xu, Structural and optical properties of ZnO thin films prepared by sol–gel method with different thickness, Appl. Surf. Sci., 257 (2011) 4031-4037.
[22] S. Mridha, D. Basak, Effect of thickness on the structural, electrical and optical properties of ZnO films, Mater. Res. Bull., 42 (2007) 875-882.
[23] L. Cui, G.-G. Wang, H.-Y. Zhang, R. Sun, X.-P. Kuang, J.-C. Han, Effect of film thickness and annealing temperature on the structural and optical properties of ZnO thin films deposited on sapphire (0001) substrates by sol–gel, Ceram. Int., 39 (2013) 3261-3268.
[24] M. Bouderbala, S. Hamzaoui, B. Amrani, A.H. Reshak, M. Adnane, T. Sahraoui, M. Zerdali, Thickness dependence of structural, electrical and optical behaviour of undoped ZnO thin films, Physica B: Condensed Matter, 403 (2008) 3326-3330.
[25] Z.N. Kayani, F. Nazir, S. Riaz, S. Naseem, Structural, optical and magnetic properties of manganese zinc oxide thin films prepared by sol–gel dip coating method, Superlattices and Microstructures, 82 (2015) 472-482.
[26] R. Rajalakshmi, S. Angappane, Effect of thickness on the structural and optical properties of sputtered ZnO and ZnO:Mn thin films, J. Alloys Compd., 615 (2014) 355-362.
[27] M. Venkaiah, R. Singh, Effect of thickness on structural, optical and mechanical properties of Mn doped ZnO nanocrystalline thin films RF sputtered in nitrogen gas environment, Superlattices Microstruct., 72 (2014) 164-171.
[28] V. Kumar, N. Singh, R.M. Mehra, A. Kapoor, L.P. Purohit, H.C. Swart, Role of film thickness on the properties of ZnO thin films grown by sol-gel method, Thin Solid Films, 539 (2013) 161-165.
[29] R. Mariappan, V. Ponnuswamy, P. Suresh, N. Ashok, P. Jayamurugan, A. Chandra Bose, Influence of film thickness on the properties of sprayed ZnO thin films for gas sensor applications, Superlattices and Microstructures, 71 (2014) 238-249.
[30] R.S. Reddy, A. Sreedhar, A.S. Reddy, S.J.A.M.L. Uthanna, Effect of film thickness on the structural morphological and optical properties of nanocrystalline ZnO films formed by RF magnetron sputtering, 3 (2012) 239-245.
[31] M. Alias, R. Aljarrah, H. Al-Lamy, K.J.I.J.A.I.E.M. Adem, Investigation the effect of thickness on the structural and optical properties of nano ZnO films prepared by dc magnetron sputtering, 2 (2013) 198-203.
[32] E.Ş. Tüzemen, S. Eker, H. Kavak, R. Esen, Dependence of film thickness on the structural and optical properties of ZnO thin films, Appl. Surf. Sci., 255 (2009) 6195-6200.
[33] M. Ali Yıldırım, A. Ateş, Influence of films thickness and structure on the photo-response of ZnO films, Opt. Commun., 283 (2010) 1370-1377.
[34] M.F. Malek, M.H. Mamat, T. Soga, S.A. Rahman, S. Abu Bakar, A.S. Ismail, R. Mohamed, S.A.H. Alrokayan, H.A. Khan, M.R. Mahmood, Thickness-controlled synthesis of vertically alignedc-axis oriented ZnO nanorod arrays: Effect of growth time via novel dual sonication sol–gel process, Jpn. J. Appl. Phys., 55 (2015) 01AE15.
[35] S. Bo, Z. Ping, First-principles local density approximation (LDA) + U and generalized gradient approximation (GGA) + U studies of plutonium oxides, Chinese Physics B, 17 (2008) 1364-1370.

[36] E. Benrezgua, B. Deghfel, A. Mahroug, M.K. Yaakob, A. Boukhari, R. Amari, S. Kheawhom, A.A. Mohamad, Experimental and theoretical studies on structural, morphological, electronic, optical and magnetic properties of Zn1-xCuxO thin films (0≤x≤0.125), Materials Science in Semiconductor Processing, 134 (2021) 106012.
[37] V.I. Anisimov, J. Zaanen, O.K. Andersen, Band theory and Mott insulators: Hubbard U instead of Stoner I, Physical Review B, 44 (1991) 943.
[38] M. Yaakob, N. Hussin, M. Taib, T. Kudin, O. Hassan, A. Ali, M. Yahya, First principles LDA+ U calculations for ZnO materials, Integrated Ferroelectrics, 155 (2014) 15-22.
[39] M.V. Gallegos, C.R. Luna, M.A. Peluso, L.C. Damonte, J.E. Sambeth, P.V. Jasen, Effect of Mn in ZnO using DFT calculations: Magnetic and electronic changes, Journal of Alloys and Compounds, 795 (2019) 254-260.
[40] M.F. Kasim, A.K.A.b. Darman, M.K. Yaakob, N. Badar, N. Kamarulzaman, Experimental and first-principles DFT studies on the band gap behaviours of microsized and nanosized Zn(1−x)MnxO materials, PCCP, 21 (2019) 19126-19146.
[41] L. Wu, T. Hou, Y. Wang, Y. Zhao, Z. Guo, Y. Li, S.-T. Lee, First-principles study of doping effect on the phase transition of zinc oxide with transition metal doped, J. Alloys Compd., 541 (2012) 250-255.
[42] K. Wetzig, C.M. Schneider, Metal based thin films for electronics, Wiley-VCH Verlag GmbH & Co. KGaA, Weinheim, 2006.
[43] M. Ghougali, Elaboration and characterization of nanostructuring NiO thin films for gas sensing applications, Faculty of Exact Sciences and Science of Nature and Life, Mohamed Khider, BISKRA, Algeria, 2019.
[44] S.J.E.A.S.M.B. Abdullahi, RF Sputtered Zinc Oxide (ZnO) Thin Films: A Review, 2 (2019) 75-82.
[45] L. Pithan, On the Role of External Stimuli to Tailor Growth of Organic Thin Films, Mathematisch-Naturwissenschaftlichen Fakultät, Humboldt-Universität zu Berlin, Germany, 2017.
[46] R.P. García, Controlled Deposition of FullerenesEffects of Topological nano-Modifications of a Surface onAggregation and Growth Phenomena, Mathematik und Naturwissenschaftender Technischen, Universität Berlin, 2018.
[47] B.I. Šklovskij, A.L. Ėfros, Electronic properties of doped semiconductors, Springer, Berlin, Heidelberg, 1984.
[48] D.S. Hecht, L. Hu, G.J.A.m. Irvin, Emerging transparent electrodes based on thin films of carbon nanotubes, graphene, and metallic nanostructures, 23 (2011) 1482-1513.
[49] Tcm, G. Kiriakidis, H.Y. Lee, B. Meyer, M. Peeble, A. Zunger, M. International Symposium on Transparent Conductive, Tcm, Transparent conductive materials, TCM series (2014).
[50] H. Sato, T. Minami, S. Takata, T. Yamada, Transparent conducting p-type NiO thin films prepared by magnetron sputtering, Thin Solid Films, 236 (1993) 27-31.
[51] K.H.L. Zhang, K. Xi, M.G. Blamire, R.G. Egdell, P-type transparent conducting oxides, J. Phys.: Condens. Matter, 28 (2016) 383002.
[52] K. Fleischer, E. Norton, D. Mullarkey, D. Caffrey, I.V. Shvets, Quantifying the Performance of P-Type Transparent Conducting Oxides by Experimental Methods, 10 (2017) 1019.

[53] R. Amari, A. Mahroug, A. Boukhari, B. Deghfel, N. Selmi, Structural, Optical and Luminescence Properties of ZnO Thin Films Prepared by Sol-Gel Spin-Coating Method: Effect of Precursor Concentration, Chinese Physics Letters, 35 (2018) 016801.
[54] A. Khayatian, M.A. Kashi, R. Azimirad, S. Safa, S.F.A. Akhtarian, Effect of annealing process in tuning of defects in ZnO nanorods and their application in UV photodetectors, Optik, 127 (2016) 4675-4681.
[55] V. Cauda, R. Gazia, S. Porro, S. Stassi, G. Canavese, I. Roppolo, A. Chiolerio, Nanostructured ZnO materials: synthesis, properties and applications, Handbook of Nanomaterials Properties, Springer2014, pp. 137-177.
[56] C. Jagadish, S.J. Pearton, Zinc oxide bulk, thin films and nanostructures : processing, properties and applications, Elsevier, Oxford; Amsterdam, 2011.
[57] M.A. Borysiewicz, ZnO as a Functional Material, a Review, Crystals, 9 (2019) 505.
[58] M. Abdelhafid, Etude des couches minces d'Oxyde de Zinc dopé Aluminium et Cobalt élaborées par la technique sol gel-spin coating, Frères Mentouri Constantine, Algeria, 2015.
[59] H. Morkoç, U. Özgür, Zinc oxide : fundamentals, materials and device technology, Wiley-VCH, Weinheim, 2009.
[60] T. Subramanyam, B. Srinivasulu Naidu, S.J.C.R. Uthanna, T.J.o. Experimental, I. Crystallography, Physical properties of zinc oxide films prepared by dc reactive magnetron sputtering at different sputtering pressures, 35 (2000) 1193-1202.
[61] L. Ozawa, CATHODOLUMINESCENCE AND PHOTOLUMINESCENCE : theories and practical applications, CRC PRESS, [S.l.], 2019.
[62] K. Vanheusden, C. Seager, W.t. Warren, D. Tallant, J.J.A.p.l. Voigt, Correlation between photoluminescence and oxygen vacancies in ZnO phosphors, Applied Physics Letters, 68 (1996) 403-405.
[63] J. Nayak, S. Kimura, S. Nozaki, Enhancement of the visible luminescence from the ZnO nanocrystals by Li and Al co-doping, Journal of Luminescence, 129 (2009) 12-16.
[64] R. Amari, B. Deghfel, A. Mahroug, A.A. Mohamad, A. Boukhari, N. Selmi, Effects of Mn doping on the structural, morphological, electronic and optical properties of ZnO thin films by sol-gel spin coating method: An experimental and DFT+U study, Physica B: Condensed Matter, 577 (2020) 411766.
[65] B. Al Farsi, T.M. Souier, F. Al Marzouqi, M. Al Maashani, M. Bououdina, H.M. Widatallah, M. Al Abri, Structural and optical properties of visible active photocatalytic Al doped ZnO nanostructured thin films prepared by dip coating, Opt. Mater., 113 (2021) 110868.
[66] F. Hussain, M. Imran, R.M.A. Khalil, N.A. Niaz, A.M. Rana, M.A. Sattar, M. Ismail, A. Majid, S. Kim, F. Iqbal, M.A. Javid, S. Saeed, A. Sattar, An insight of Mg doped ZnO thin films: A comparative experimental and first-principle investigations, Physica E: Low-dimensional Systems and Nanostructures, 115 (2020) 113658.
[67] A.M. Alsaad, A.A. Ahmad, I.A. Qattan, Q.M. Al-Bataineh, Z. Albataineh, Structural, Optoelectrical, Linear, and Nonlinear Optical Characterizations of Dip-Synthesized Undoped ZnO and Group III Elements (B, Al, Ga, and In)-Doped ZnO Thin Films, Crystals, 10 (2020).
[68] G. Voicu, D. Miu, C.-D. Ghitulica, S.-I. Jinga, A.-I. Nicoara, C. Busuioc, A.-M. Holban, Co doped ZnO thin films deposited by spin coating as antibacterial coating for metallic implants, Ceram. Int., 46 (2020) 3904-3911.
[69] Z. Xu, Y.J. Yuan, Implementation of guiding layers of surface acoustic wave devices: A review, Biosensors and Bioelectronics, 99 (2018) 500-512.

[70] R. Vittal, K.-C. Ho, Zinc oxide based dye-sensitized solar cells: A review, Renewable and Sustainable Energy Reviews, 70 (2017) 920-935.
[71] N.K. Zayer, R. Greef, K. Rogers, A.J.C. Grellier, C.N. Pannell, In situ monitoring of sputtered zinc oxide films for piezoelectric transducers, Thin Solid Films, 352 (1999) 179-184.
[72] R. Faiz, Zinc oxide light-emitting diodes: a review, Optical Engineering, 58 (2019) 1-20.
[73] R. Kumar, O. Al-Dossary, G. Kumar, A.J.N.-M.L. Umar, Zinc oxide nanostructures for NO 2 gas–sensor applications: A review, 7 (2015) 97-120.
[74] S. Sharma, C. Periasamy, P. Chakrabarti, Thickness dependent study of RF sputtered ZnO thin films for optoelectronic device applications, Electronic Materials Letters, 11 (2015) 1093-1101.
[75] S.S. Alias, A.A. Mohamad, Synthesis of Zinc Oxide by Sol-Gel Method for Photoelectrochemical Cells, 2014.
[76] A.B. Djurišić, A.M.C. Ng, X.Y. Chen, ZnO nanostructures for optoelectronics: Material properties and device applications, Progress in Quantum Electronics, 34 (2010) 191-259.
[77] M. Kaliva, M. Vamvakaki, Chapter 17 - Nanomaterials characterization, in: R. Narain (Ed.) Polymer Science and Nanotechnology, Elsevier2020, pp. 401-433.
[78] A.H. Hammad, M.S. Abdel-wahab, S. Vattamkandathil, A.R. Ansari, Structural and optical properties of ZnO thin films prepared by RF sputtering at different thicknesses, Physica B: Condensed Matter, 540 (2018) 1-8.
[79] A. Mhamdi, R. Mimouni, A. Amlouk, M. Amlouk, S. Belgacem, Study of copper doping effects on structural, optical and electrical properties of sprayed ZnO thin films, Journal of Alloys and Compounds, 610 (2014) 250-257.
[80] J.-M. Myoung, W.-H. Yoon, D.-H. Lee, I. Yun, S.-H. Bae, S.-Y. Lee, Effects of Thickness Variation on Properties of ZnO Thin Films Grown by Pulsed Laser Deposition, Jpn. J. Appl. Phys., 41 (2002) 28-31.
[81] H. Ennaceri, M. Boujnah, D. Erfurt, J. Rappich, X. Lifei, A. Khaldoun, A. Benyoussef, A. Ennaoui, A. Taleb, Influence of stress on the photocatalytic properties of sprayed ZnO thin films, Sol. Energy Mater. Sol. Cells, 201 (2019) 110058.
[82] R. Gayen, K. Sarkar, S. Hussain, R. Bhar, A. Pal, ZnO films prepared by modified sol-gel technique, (2011).
[83] N. Kaneva, A. Bojinova, K. Papazova, D. Dimitrov, I. Svinyarov, M.J.B.C.C. Bogdanov, Effect of thickness on the photocatalytic properties of ZnO thin films, 47 (2015) 395-401.
[84] R.S. Gonçalves, P. Barrozo, G.L. Brito, B.C. Viana, F. Cunha, The effect of thickness on optical, structural and growth mechanism of ZnO thin film prepared by magnetron sputtering, Thin Solid Films, 661 (2018) 40-45.
[85] S. Azara Hussain, A. Jabbar Radi, Study the effect of film thickness on the structural and optical of (ZnO) thin film prepared by pulsed laser deposition, Journal of Physics: Conference Series, 1294 (2019) 022001.
[86] A. Namoune, T. Touam, A. Chelouche, Thickness, annealing and substrate effects on structural, morphological, optical and waveguiding properties of RF sputtered ZnO thin films, Journal of Materials Science: Materials in Electronics, 28 (2017) 12207-12219.
[87] M.S. Kim, K.G. Yim, J.-Y. Leem, S. Kim, G. Nam, D.-Y. Lee, J.S. Kim, J.S.J.J.o.t.K.P.S. Kim, Thickness dependence of properties of ZnO thin films on porous silicon grown by plasma-assisted molecular beam epitaxy, Journal of the Korean Physical Society, 59 (2011) 2354-2361.

[88] T. Singh, T. Lehnen, T. Leuning, D. Sahu, S. Mathur, Thickness dependence of optoelectronic properties in ALD grown ZnO thin films, Applied Surface Science, 289 (2014) 27-32.
[89] S. Benramache, F. Chabane, B. Benhaoua, F.Z. Lemmadi, Influence of growth time on crystalline structure, conductivity and optical properties of ZnO thin films, Journal of Semiconductors, 34 (2013) 023001.
[90] A. Jain, P. Sagar, R. Mehra, Changes of structural, optical and electrical properties of sol-gel derived ZnO films with their thickness, Materials Science Poland, 25 (2007) 233--242.
[91] V. Kumar, N. Singh, R. Mehra, A. Kapoor, L. Purohit, H. Swart, Role of film thickness on the properties of ZnO thin films grown by sol-gel method, Thin Solid Films, 539 (2013) 161-165.
[92] A. Zhong, J. Tan, H. Huang, S. Chen, M. Wang, S. Xu, Thickness effect on the evolution of morphology and optical properties of ZnO films, Appl. Surf. Sci., 257 (2011) 4051-4055.
[93] R. Hong, J. Shao, H. He, Z. Fan, Influence of buffer layer thickness on the structure and optical properties of ZnO thin films, Appl. Surf. Sci., 252 (2006) 2888-2893.
[94] R.S. Reddy, A. Sreedhar, A.S. Reddy, S. Uthanna, Effect of film thickness on the structural morphological and optical properties of nanocrystalline ZnO films formed by RF magnetron sputtering, Adv. Mater. Lett, 3 (2012) 239-245.
[95] M. Suchea, S. Christoulakis, M. Katharakis, N. Vidakis, E. Koudoumas, Influence of thickness and growth temperature on the optical and electrical properties of ZnO thin films, Thin Solid Films, 517 (2009) 4303-4306.
[96] B.L. Zhu, X.H. Sun, S.S. Guo, X.Z. Zhao, J. Wu, R. Wu, J. Liu, Effect of Thickness on the Structure and Properties of ZnO Thin Films Prepared by Pulsed Laser Deposition, Jpn. J. Appl. Phys., 45 (2006) 7860-7865.
[97] S. Shariffudin, M. Salina, S. Herman, M.J.T.o.E. Rusop, E. Materials, Effect of film thickness on structural, electrical, and optical properties of sol-gel deposited layer-by-layer ZnO nanoparticles, Trans. Electr. Electron. Mater., 13 (2012) 102-105.
[98] R. Gayen, K. Sarkar, S. Hussain, R. Bhar, A. Pal, ZnO films prepared by modified sol-gel technique, Indian Journal of Pure & Applied Physics, 49 (2011) 470-477.
[99] E.S. Shim, H.S. Kang, J.S. Kang, J.H. Kim, S.Y. Lee, Effect of the variation of film thickness on the structural and optical properties of ZnO thin films deposited on sapphire substrate using PLD, Appl. Surf. Sci., 186 (2002) 474-476.
[100] C.H. Chia, W.C. Tsai, J.W. Chiou, Thickness effect on luminescent properties of sol–gel derived ZnO thin films, J. Lumin., 136 (2013) 160-164.
[101] S. Mridha, D. Basak, Thickness dependent photoconducting properties of ZnO films, Chem. Phys. Lett., 427 (2006) 62-66.
[102] N. Kaneva, A. Bojinova, K. Papazova, D. Dimitrov, I. Svinyarov, M.J.B.C.C. Bogdanov, Effect of thickness on the photocatalytic properties of ZnO thin films, Bulgarian Chemical Communications, 47 (2015) 395-401.
[103] A. Jain, P. Sagar, R.J.M.S.P. Mehra, Changes of structural, optical and electrical properties of sol-gel derived ZnO films with their thickness, 25 (2007) 233--242.
[104] E.T.J.S.J.o.P. Wu, Synthesis and Effect of Thickness on the Structure and Optical Properties of ZnO Thin Films Prepared By Sol-Gel Spin Coating Method, Science Journal of Physics, 2013 (2015).

[105] R. Pérez-Cuapio, M. Pacio, H. Juárez, J.A. Alvarado, C. Guarneros, C. Bueno, A. Pacio, Effect of ZnO Film Thickness on its Optical and Structural Properties, Journal of Nano Research, 52 (2018) 102-114.
[106] A.A.J.D.J.F.P.S. Habeeb, Influence of Thickness and Annealing on Some Physical Properties of Zinc Oxide Films, Diyala journal for pure sciences, 14 (2018).
[107] B. Kafle, B. Pokhrel, P.J.S.M.S.E. Lamichhane, Thickness Dependence of Optical and Electrical Properties of Zinc Oxide Thin Films, SOJ Materials Science & Engineering, 4 (2016) 1-4.
[108] M. Momoh, S. Abdullahi, A. Moreh, Influence of Thickness on Electrical and Structural Properties of Zinc Oxide (ZnO) Thin Films Prepared by RF Sputtering Technique, International Journal of Recent Research in Physics and Chemical Sciences, (2015).
[109] P. Carvalho, P. Sampaio, S. Azevedo, C. Vaz, J.P. Espinós, V. Teixeira, J.O. Carneiro, Influence of thickness and coatings morphology in the antimicrobial performance of zinc oxide coatings, Applied Surface Science, 307 (2014) 548-557.
[110] M.A.J.I.J.o.P. Salim, Effect of thickness on the optical properties of ZnO thin films prepared by pulsed laser deposition technique (PLD), 15 (2017) 114-121.
[111] J.-L. Tian, H.-Y. Zhang, G.-G. Wang, X.-Z. Wang, R. Sun, L. Jin, J.-C. Han, Influence of film thickness and annealing temperature on the structural and optical properties of ZnO thin films on Si (100) substrates grown by atomic layer deposition, Superlattices and Microstructures, 83 (2015) 719-729.
[112] L. Miao, S. Tanemura, M. Tanemura, S.P. Lau, B.K. Tay, Thickness-dependent optical properties of ZnO thin films, Journal of Materials Science: Materials in Electronics, 18 (2007) 343-346.
[113] Y. Zhang, G. Du, B. Liu, H. Zhu, T. Yang, W. Li, D. Liu, S. Yang, Effects of ZnO buffer layer thickness on properties of ZnO thin films deposited by low-pressure MOCVD, J. Cryst. Growth, 262 (2004) 456-460.
[114] N. Gopalakrishnan, L. Balakrishnan, A. Brindha, G.J.C.R. Jayalakshmi, Technology, Thickness and substrate orientation dependence of ferromagnetism in Mn doped ZnO thin films, Cryst. Res. Technol, 47 (2012) 45-52.
[115] D. Levy, M. Zayat, The sol-gel handbook, 2015.
[116] C.J. Brinker, G.W. Scherer, Sol-Gel Science : the Physics and Chemistry of Sol-Gel Processing, Elsevier Science, Saint Louis, 2014.
[117] A. Chládová, J. Wiener, J.M. Luthuli, V.J.A.R.J. Zajícová, Dyeing of glass fibres by the sol gel method, 11 (2011) 18-23.
[118] L. Znaidi, Sol–gel-deposited ZnO thin films: A review, Materials Science and Engineering: B, 174 (2010) 18-30.
[119] A.J. Sanchez-Herencia, Water Based Colloidal Processing of Ceramic Laminates, Key Eng. Mater., 333 (2007) 39-48.
[120] G. Amokrane, C. Falentin-Daudré, S. Ramtani, V. Migonney, A Simple Method to Functionalize PCL Surface by Grafting Bioactive Polymers Using UV Irradiation, IRBM, 39 (2018) 268-278.
[121] B.D. Cullity, S.R. Stock, S. Pearson India Education, Elements of X-ray diffraction, Pearson India Education Services, [Miejsce nieznane], 2015.
[122] M. Birkholz, Thin Film Analysis by X-Ray Scattering, (2010).
[123] W.C. Sanders, Atomic force microscopy : fundamental concepts and laboratory investigations, 2020.

[124] W.R. Bowen, N. Hilal, Atomic force microscopy in process engineering : introduction to AFM for improved processes and products, Butterworth-Heinemann, Amsterdam; London, 2009.
[125] P.J. Eaton, P. West, P. Oxford University, Atomic force microscopy, Oxford University Press, Oxford, 2019.
[126] I. Horcas, R. Fernández, J. Gomez-Rodriguez, J. Colchero, J. Gómez-Herrero, A. Baro, WSXM: a software for scanning probe microscopy and a tool for nanotechnology, Rev. Sci. Instrum., 78 (2007) 013705.
[127] I. Cimieri, Sol-gel preparation and characterization of titanium dioxide films for degradation of organic pollutants, FACULTY OF SCIENCES, Ghent University, 2014.
[128] N. Brodusch, H. Demers, R. Gauvin, Field emission scanning electron microscopy : new perspectives for materials characterization, 2018.
[129] P. USA, Electron Microscopy: Nonmagnetic Drives and Stages for Vacuum, 2021, April 02.
[130] H.-H. Perkampus, Uv-vis spectroscopy and its applications, Springer-Verlag Berlin An, [Place of publication not identified], 2012.
[131] S. Manakh, Contribution à l'étude des propriétés de films ZnO, departement de physique, Mentouri - Constantine, Algeria, 2010.
[132] S.J. Clark, M.D. Segall, C.J. Pickard, P.J. Hasnip, M.I. Probert, K. Refson, M.C.J.Z.f.K.-C.M. Payne, First principles methods using CASTEP, 220 (2005) 567-570.
[133] K. Harun, N.A. Salleh, B. Deghfel, M.K. Yaakob, A.A. Mohamad, DFT + U calculations for electronic, structural, and optical properties of ZnO wurtzite structure: A review, Results in Physics, 16 (2020) 102829.
[134] P.-A. Martin, F. Rothen, S. Goldfarb, A.N. Jordan, S. Leach, Many-Body Problems and Quantum Field Theory : an Introduction, (2013).
[135] A. Fabrocini, S. Fantoni, E. Krotscheck, T. European Summer School on Microscopic Many-Body, A. their, Introduction to modern methods of quantum many-body theory and their applications, (2002).
[136] F. Calogero, Exactly solvable one-dimensional many-body problems, Lettere al Nuovo Cimento (1971-1985), 13 (1975) 411-416.
[137] J.-M. Combes, P. Duclos, R. Seiler, The born-oppenheimer approximation, Rigorous atomic and molecular physics, Springer1981, pp. 185-213.
[138] V. Fock, Näherungsmethode zur Lösung des quantenmechanischen Mehrkörperproblems, Z. Phys., 61 (1930) 126-148.
[139] H. Eschrig, The fundamentals of density functional theory, Ed. am Gutenbergplatz, Leipzig, 2003.
[140] P. Hohenberg, W. Kohn, Inhomogeneous Electron Gas, Phys. Rev., 136 (1964) B864-B871.
[141] W. Kohn, L.J. Sham, Self-Consistent Equations Including Exchange and Correlation Effects, Phys. Rev., 140 (1965) A1133-A1138.
[142] A.W. Overhauser, Observability of Charge-Density Waves by Neutron Diffraction, Physical Review B, 3 (1971) 3173-3182.
[143] W. Yang, Direct calculation of electron density in density-functional theory, Phys. Rev. Lett., 66 (1991) 1438-1441.
[144] T. Grabo, E.K.U. Gross, Density-functional theory using an optimized exchange-correlation potential, Chem. Phys. Lett., 240 (1995) 141-150.

[145] C. Filippi, C.J. Umrigar, X. Gonze, Separation of the exchange-correlation potential into exchange plus correlation: An optimized effective potential approach, Phys. Rev. A, 54 (1996) 4810-4814.
[146] R. van Leeuwen, E.J. Baerends, Exchange-correlation potential with correct asymptotic behavior, Phys. Rev. A, 49 (1994) 2421-2431.
[147] J.P. Perdew, A. Zunger, Self-interaction correction to density-functional approximations for many-electron systems, Physical Review B, 23 (1981) 5048-5079.
[148] J.P. Perdew, Y. Wang, Accurate and simple analytic representation of the electron-gas correlation energy, Physical Review B, 45 (1992) 13244-13249.
[149] L. Hedin, B.I. Lundqvist, Explicit local exchange-correlation potentials, Journal of Physics C: Solid State Physics, 4 (1971) 2064-2083.
[150] D.M. Ceperley, B.J. Alder, Ground State of the Electron Gas by a Stochastic Method, Phys. Rev. Lett., 45 (1980) 566-569.
[151] E. Wigner, On the Interaction of Electrons in Metals, Phys. Rev., 46 (1934) 1002-1011.
[152] J.P. Perdew, E.R. McMullen, A. Zunger, Density-functional theory of the correlation energy in atoms and ions: A simple analytic model and a challenge, Phys. Rev. A, 23 (1981) 2785-2789.
[153] F. Oba, M. Choi, A. Togo, I. Tanaka, Point defects in ZnO: an approach from first principles, Science and Technology of Advanced Materials, 12 (2011) 034302.
[154] V.I. Anisimov, F. Aryasetiawan, A.I. Lichtenstein, First-principles calculations of the electronic structure and spectra of strongly correlated systems: theLDA+Umethod, J. Phys.: Condens. Matter, 9 (1997) 767-808.
[155] V.I. Anisimov, J. Zaanen, O.K. Andersen, Band theory and Mott insulators: Hubbard U instead of Stoner I, Physical Review B, 44 (1991) 943-954.
[156] E.H. Lieb, Two theorems on the Hubbard model, Phys. Rev. Lett., 62 (1989) 1201-1204.
[157] J.P. Perdew, K. Burke, M. Ernzerhof, Generalized Gradient Approximation Made Simple, Phys. Rev. Lett., 77 (1996) 3865-3868.
[158] J.P. Perdew, P. Ziesche, H. Eschrig, Electronic structure of solids' 91, Akademie Verlag, Berlin, 1991.
[159] B. Himmetoglu, A. Floris, S. De Gironcoli, M.J.I.J.o.Q.C. Cococcioni, Hubbard-corrected DFT energy functionals: The LDA+ U description of correlated systems, 114 (2014) 14-49.
[160] G. Kresse, J. Furthmüller, Efficient iterative schemes for ab initio total-energy calculations using a plane-wave basis set, Physical Review B, 54 (1996) 11169-11186.
[161] N. Marzari, D. Vanderbilt, M.C. Payne, Ensemble Density-Functional Theory for Ab Initio Molecular Dynamics of Metals and Finite-Temperature Insulators, Phys. Rev. Lett., 79 (1997) 1337-1340.
[162] R.D. Cowan, Atomic Self-Consistent-Field Calculations Using Statistical Approximations for Exchange and Correlation, Phys. Rev., 163 (1967) 54-61.
[163] G.P. Srivastava, Broyden's method for self-consistent field convergence acceleration, J. Phys. A: Math. Gen., 17 (1984) L317-L321.
[164] A.S. Banerjee, P. Suryanarayana, J.E. Pask, Periodic Pulay method for robust and efficient convergence acceleration of self-consistent field iterations, Chem. Phys. Lett., 647 (2016) 31-35.
[165] M.I.J. Probert, Improved algorithm for geometry optimisation using damped molecular dynamics, J. Comput. Phys., 191 (2003) 130-146.
[166] J. BARZILAI, J.M. BORWEIN, Two-Point Step Size Gradient Methods, IMA Journal of Numerical Analysis, 8 (1988) 141-148.

[167] R.P. Feynman, Forces in Molecules, Phys. Rev., 56 (1939) 340-343.
[168] H.J.F.D. Hellman, Leipzig, Einführung in die Quantenchemie, 285 (1937).
[169] C. Fiolhais, F. Nogueira, M.A.L. Marques, A primer in density functional theory, Springer, Berlin; London, 2011.
[170] Z. Long, L. Peng-Fei, Y. Zhong-Yuan, M. Shi-Jia, D. Lu, L. Jian-Tao, The electronic and magnetic properties of (Mn, C)-codoped ZnO diluted magnetic semiconductor, Chinese Physics B, 21 (2012) 097103.
[171] S.J. Clark, M.D. Segall, C.J. Pickard, P.J. Hasnip, M.I. Probert, K. Refson, M.C. Payne, First principles methods using CASTEP, Zeitschrift für Kristallographie-Crystalline Materials, 220 (2005) 567-570.
[172] D. Vanderbilt, Soft self-consistent pseudopotentials in a generalized eigenvalue formalism, Physical Review B, 41 (1990) 7892-7895.
[173] M. Xin, L.Z. Hu, D.-P. Liu, N.-S. Yu, Effect of Mn doping on the optical, structural and photoluminescence properties of nanostructured ZnO thin film synthesized by sol–gel technique, Superlattices Microstruct., 74 (2014) 234-241.
[174] A. Mahroug, S. Boudjadar, S. Hamrit, L. Guerbous, Structural, morphological and optical properties of undoped and Co-doped ZnO thin films prepared by sol–gel process, Journal of Materials Science: Materials in Electronics, 25 (2014) 4967-4974.
[175] M. Saleem, L. Fang, H. Ruan, F. Wu, Q. Huang, C. Xu, C. Kong, Effect of zinc acetate concentration on the structural and optical properties of ZnO thin films deposited by Sol-Gel method, International Journal of Physical Sciences, 7 (2012) 2971-2979.
[176] D. Raoufi, T. Raoufi, The effect of heat treatment on the physical properties of sol–gel derived ZnO thin films, Appl. Surf. Sci., 255 (2009) 5812-5817.
[177] S. Fabbiyola, L.J. Kennedy, A.A. Dakhel, M. Bououdina, J.J. Vijaya, T. Ratnaji, Structural, microstructural, optical and magnetic properties of Mn-doped ZnO nanostructures, J. Mol. Struct., 1109 (2016) 89-96.
[178] U.N. Maiti, P.K. Ghosh, S. Nandy, K.K. Chattopadhyay, Effect of Mn doping on the optical and structural properties of ZnO nano/micro-fibrous thin film synthesized by sol–gel technique, Physica B: Condensed Matter, 387 (2007) 103-108.
[179] N. Kaneva, A. Bojinova, K. Papazova, D. Dimitrov, I. Svinyarov, M. Bogdanov, Effect of thickness on the photocatalytic properties of ZnO thin films, Bulg ChemCommun, 47 (2015) 395-401.
[180] C.-Y. Tsay, K.-S. Fan, S.-H. Chen, C.-H. Tsai, Preparation and characterization of ZnO transparent semiconductor thin films by sol–gel method, J. Alloys Compd., 495 (2010) 126-130.
[181] N. Kaneva, C. Dushkin, Preparation of nanocrystalline thin films of ZnO by sol-gel dip coating, Bulg Chem Commun, 43 (2011) 259-263.
[182] M. Mazhdi, J. Saydi, M. Karimi, J. Seidi, F. Mazhdi, A study on optical, photoluminescence and thermoluminescence properties of ZnO and Mn doped-ZnO nanocrystalline particles, Optik, 124 (2013) 4128-4133.
[183] Y. Caglar, Sol–gel derived nanostructure undoped and cobalt doped ZnO: Structural, optical and electrical studies, J. Alloys Compd., 560 (2013) 181-188.
[184] T.P. Rao, M.S. Kumar, S.A. Angayarkanni, M. Ashok, Effect of stress on optical band gap of ZnO thin films with substrate temperature by spray pyrolysis, Journal of Alloys and compounds, 485 (2009) 413-417.
[185] L. Xu, G. Zheng, J. Miao, F. Xian, Dependence of structural and optical properties of sol–gel derived ZnO thin films on sol concentration, Appl. Surf. Sci., 258 (2012) 7760-7765.

[186] M. Baneto, A. Enesca, Y. Lare, K. Jondo, K. Napo, A. Duta, Effect of precursor concentration on structural, morphological and opto-electric properties of ZnO thin films prepared by spray pyrolysis, Ceram. Int., 40 (2014) 8397-8404.
[187] R. Karmakar, S.K. Neogi, A. Banerjee, S. Bandyopadhyay, Structural; morphological; optical and magnetic properties of Mn doped ferromagnetic ZnO thin film, Applied Surface Science, 263 (2012) 671-677.
[188] Y.-J. Choi, H.-H. Park, A simple approach to the fabrication of fluorine-doped zinc oxide thin films by atomic layer deposition at low temperatures and an investigation into the growth mode, Journal of Materials Chemistry C, 2 (2014) 98-108.
[189] B. Straumal, S. Protasova, A. Mazilkin, A. Myatiev, P. Straumal, G. Schütz, E. Goering, B. Baretzky, Ferromagnetic properties of the Mn-doped nanograined ZnO films, J. Appl. Phys., 108 (2010) 073923.
[190] E. Chikoidze, Y. Dumont, F. Jomard, O. Gorochov, Electrical and optical properties of ZnO:Mn thin films grown by MOCVD, Thin Solid Films, 515 (2007) 8519-8523.
[191] Z.-W. Jin, Y.-Z. Yoo, T. Sekiguchi, T. Chikyow, H. Ofuchi, H. Fujioka, M. Oshima, H. Koinuma, Blue and ultraviolet cathodoluminescence from Mn-doped epitaxial ZnO thin films, Appl. Phys. Lett., 83 (2003) 39-41.
[192] Q.-J. Liu, Z.-T. Liu, J.-C. Chen, L.-P. Feng, H. Tian, First-principles study of structural, mechanical, electronic and optical properties of 3R- and 2H-CuGaO2, Physica B: Condensed Matter, 406 (2011) 3377-3382.
[193] K. Harun, N. Mansor, M.K. Yaakob, M.F.M. Taib, Z.A. Ahmad, A.A. Mohamad, On the verification of sol–gel-derived ZnO nanoparticle properties using first-principles calculation, J. Sol-Gel Sci. Technol., 80 (2016) 56-67.

List of publications and communications

1- Publications

1. Thickness effect on the properties of Mn-doped ZnO thin films synthesis by sol-gel and comparison to first-principles calculations
A Boukhari, B Deghfel, A Mahroug, R Amari, N Selmi, S Kheawhom, A A Mohamad

Ceramics International Volume 47, Issue 12, 15 June 2021, Pages 17276-17285

https://www.sciencedirect.com/science/article/pii/S0272884221007021

2. Thickness effect on the properties of 4% Mn-doped ZnO thin films grown by Sol-Gel spin coating deposition
A Boukhari, B Deghfel, A Mahroug, R Amari, N Selmi, A A Mohamad
Macromolecular Symposia journal, Volume 397, Issue 1, 17 June 2021.

https://onlinelibrary.wiley.com/doi/abs/10.1002/masy.202000235

3. Effects of Mn doping on the structural, morphological, electronic and optical properties of ZnO thin flms by sol-gel spin coating method: An experimental and DFT+U study
R Amari, B Deghfel, A Mahroug, A A Mohamad, **A Boukhari**, N Selmi
Physica B: Condensed Matter Volume 577, 15 January 2020, 411766.

https://www.sciencedirect.com/science/article/abs/pii/S0921452619306659

4. Structural, Optical and Luminescence Properties of ZnO Thin Films Prepared by Sol Gel Spin Coating Method: Effect of Precursor Concentration
R. Amari, A. Mahroug, **A. Boukhari**, B. Deghfel, N. Selmi
CHIN. PHYS. LETT. Vol. 35, No. 1 (2018) 016801.

http://cpl.iphy.ac.cn/10.1088/0256-307X/35/1/016801

5. Synthesis, Structural, Morphological, Electronic, Optical and Luminescence Properties of Pure and Manganese-Doped Zinc Oxide Nanostructured Thin Films: Effect of Doping
A. Mahroug, R. Amari, **A. Boukhari**, B. Deghfel, L. Guerbous, and N. Selmi
Journal of Nanoelectronics and Optoelectronics, Vol. 12, pp. 1–10, 2017
http://www.aspbs.com/jno/jno_contents2018.htm#v13n6

6. Experimental and theoretical studies on structural, morphological, electronic, optical and magnetic properties of Zn1-xCuxO thin films ($0 \leq x \leq 0.125$)
Elhadj Benrezgua, Bahri Deghfel, Abdelhafid Mahroug, Muhamad Kamil Yaakob**, Ammar Boukhari**, Rabie Amari, Soorathep Kheawhom, Ahmad Azmin Mohamad
Journal of Materials Science in Semiconductor Processing, Vol. 134, pp. 106012, 2021

https://www.sciencedirect.com/science/article/abs/pii/S1369800121003590

2- Communications

1. Experimental and first principles study of structural, electronic and optical properties of $Zn_{0.875}Mn_{0.125}O$ thin film
B. Deghfel, A. Mahroug, R. Amari, **A. Boukhari**, A. Bentabet
ICAMS 2018 – 7th International Conference on Advanced Materials and Systems
October 18th - 20th, 2018, Bucharest, ROMANIA
http://icams.ro/icamsresurse/2018/proceedings_icams_2018_v02.pdf

2. Studies on structural, surface morphological, optical, luminescence and UV photodetection properties of sol gel oxides thin films
A. Mahroug, R. Amari, **A. Boukhari**, B. Deghfel, E. Ben Rezgua
ICAMS 2018 – 7th International Conference on Advanced Materials and Systems
October 18th - 20th, 2018, Bucharest, ROMANIA
http://icams.ro/icamsresurse/2018/proceedings_icams_2018_v02.pdf

3. First principles LDA+U study of structural, electronic, elastic and optical properties of Mn doped wurtzite ZnO.
B. Deghfel, **A. Boukhari**, R. Amari, A. Mahroug, A. Bentabet.
Nanotechnology and nanomaterials» (NANO-2017), Ukraine - Chernivtsi, August 23- 26, 2017
http://www.iop.kiev.ua/~nano2017/files/Abstract_book.pdf

4. Elaboration and Characterization of TM-doped ZnO Thin Films: Effect of doping on structural and optical properties.
A. Mahroug, R. Amari, **A. Boukhari**, B. Deghfel.
Nanotechnology and nanomaterials» (NANO-2017), Ukraine - Chernivtsi, August 23 - 26, 2017
http://www.iop.kiev.ua/~nano2017/files/Abstract_book.pdf

5. Structural, morphological and optical properties of Mn-doped ZnO thin films prepared by sol-gel spin coating method.
A. Boukhari, B. Deghfel, A. Mahroug, A. Azmin
1st international conference on materials and energies» (IC- ME-21), Tamanghasset - Algeria, September 13 - 14, 2021

ملخص: تبحث هذه الدراسة تأثير سمك الأفلام الرقيقة لأكسيد الزنك النقي (ZnO) وأغشية ZnO الرقيقة المشبعة بالمنغنيز بنسبة 4٪ و 7٪، المترسبة باستخدام طريقة " محلول - هلام مع تقنية التدوير"، على الخصائص البنيوية والمورفولوجية والإلكترونية والبصرية .جميع الأفلام الرقيقة تبلورت على بنية "wurtzite " ذات الشكل السداسي في الاتجاه عالي التفضيل حسب المحورc . الشكل السطحي أظهر تجانسًا كبيرا مع وجود تشققات وتجاعيد. النفاذية الضوئية تتناقص مع السمك. كما أن فجوة الطاقة تتناسب عكسياً مع السمك. طيف التلألؤ الضوئي أظهر أشعة فوق بنفسجية مع وجود قمم تدل على انبعاثات قوية وضعيفة باللون الأزرق والأخضر. تم بعد ذلك تطبيق نظرية دالية الكثافة الوظيفية وطريقة Hubbard (DFT + U) لدراسة الخصائص التركيبية والإلكترونية والبصرية ل ZnO النقي وZnO المطعم ب 6.25٪ منغنيز. أظهرت النتائج انخفاض في فجوة الطاقة بين ZnO النقي إلى 6.25٪ ZnO المطعم . و وجد أيضًا أن حالات Mn3d كانت موزعة بعيدًا عن مستوى فيرمي مع تصاحب كل من الروابط الأيونية والتساهمية. لوحظ أيضا تحول طفيف نحو الطاقة المنخفضة للخصائص الضوئية بواسطة التطعيم بالمنغنيز. أظهرت النتائج النظرية سلوكًا مشابهًا لتلك التي تم الحصول عليها بالتجربة.

الكلمات الرئيسية: سمك الفيلم الرقيق؛ طريقة " محلول - هلام مع تقنية التدوير"؛ ZnOمطعم ب Mn ؛ الخصائص البنيوية، الخصائص الضوئية، DFT + U

Abstract: The structural, morphological, electronic, and optical properties of pure, 4 %, and 7 % Mn-doped ZnO thin films deposited on glass substrate by the sol–gel spin coating process are investigated in this study. All films exhibited a hexagonal wurtzite structure with a strong c-axis preference. The surface morphology was uniform, with a cracks and wrinkles. With increasing thickness, the transmittance decreased. The bandgap energy varied inversely with the coatings number. photoluminescence spectra revealed ultraviolet with strong and weak blue emission peaks, as well as weak green emission peaks. The structural, electronic, and optical properties of pure and 6.25 % Mn-doped ZnO materials were then investigated using density functional theory and the Hubbard (DFT+U) approach. The DFT+U approach demonstrated a decrease in bandgap energy from pure to 6.25 % Mn-doped ZnO material. It was also discovered that the Mn3d states were distributed far from the Fermi level, with both ionic and covalent nature bonds coexisting. Mn doping caused a small shift in optical properties toward the lower energy. The theoretical findings were consistent with those obtained through experiment.

Keyword: Film thickness; Sol-gel spin coating method; Mn-doped ZnO; Structural properties; Optical properties; DFT+U